Universiteit
Leiden
The Netherlands

Monitoring Alzheimer's disease in transgenic mice with ultra high field magnetic resonance imaging

Kara, F.

Citation

Kara, F. (2013, December 3). *Monitoring Alzheimer's disease in transgenic mice with ultra high field magnetic resonance imaging*. Retrieved from https://hdl.handle.net/1887/22736

Version:	Not Applicable (or Unknown)
License:	Leiden University Non-exclusive license
Downloaded from:	https://hdl.handle.net/1887/22736

Note: To cite this publication please use the final published version (if applicable).

Cover Page

Universiteit Leiden

The handle http://hdl.handle.net/1887/22736 holds various files of this Leiden University dissertation.

Author: Kara, Firat
Title: Monitoring Alzheimer's disease in transgenic mice with ultra high field magnetic resonance imaging
Issue Date: 2013-12-03

Monitoring Alzheimer's disease in transgenic mice with ultra high field magnetic resonance imaging

Fırat Kara

Fırat Kara
Monitoring Alzheimer‘s disease in transgenic mice with ultra high field magnetic resonance imaging
PhD Thesis, Leiden University, 3 December 2013

ISBN: 978-94-6203-496-9

© 2013 by Fırat Kara, Leiden, the Netherlands. All rights reserved except the following chapters:

Chapter 2 NeuroImage 2012, 60(2);958-966; 2006 © Elsevier. Reprinted with permission from Elsevier

Chapter 4 Magn Reson Med, 2012: doi: 10.1002/mrm.24533 © Wiley Periodicals, Inc. Reprinted with permission of John Wiley & Sons, Inc.

Chapter 5 Parts of this chapter were published in Curr Med Imag Rev 2011; 7:1:80-87 © Reprinted with permission of Bentham Science Publishers Ltd.

No part of this thesis may be reproduced in any form without the express written consent of the copyright holders.
Cover illustration courtesy of Başaran Karabulut.
Printed by CP-Wöhrmann Print Service- Zutphen.

Monitoring Alzheimer's disease in transgenic mice with ultra high field magnetic resonance imaging

Proefschrift

ter verkrijging van
de graad van Doctor aan de Universiteit Leiden,
op gezag van Rector Magnificus Prof. mr. C.J.J.M. Stolker,
volgens besluit van het College voor Promoties
te verdedigen op dinsdag 3 december 2013
klokke 08:45 uur

door

Fırat Kara
geboren te Malatya, Turkey
in 1977

Promotiecommissie

Promotor:
Prof. dr. H.J.M. de Groot

Co-promotor:
Dr. A. Alia

Overige leden:
Prof. dr. E.R. de Kloet
Prof. dr. M.A. van Buchem
Prof. dr. J. Brouwer
Prof. dr. A.M. van der Linden, University of Antwerp, Belgium

The Centre for Medical Systems Biology (CMSB), Internationale Stichting Alzheimer Onderzoek and Alzheimer Nederland are gratefully acknowledged for financial support to the printing costs of the thesis.

Knowledge should mean a full grasp of knowledge:
Knowledge means to know yourself, heart and soul.
If you have failed to understand yourself,
then all of your reading has missed its call**.**

-Yunus Emre

English version by Namık Kemal Zeybek

Voor mijn ouders

Contents

List of abbreviations **9**

1 **General introduction** **13**

1.1 Alzheimer's disease 13

1.2 Mouse models of AD 18

1.3 Magnetic resonance imaging 20

1.4 Monitoring AD using MR- based techniques 27

1.5 Thesis scope 32

References 34

2 **Monitoring blood flow alterations in the Tg2576 mouse model of Alzheimer's disease*** **47**

2.1 Abstract 47

2.2 Introduction 47

2.3 Materials and Methods 49

2.4 Results and Discussion 52

Acknowledgements 63

Supplementary Material 64

References 66

3 **Longitudinal monitoring of transverse relaxation time (T_2) changes in the corpus callosum region of a mouse model of Alzheimer' disease*** **73**

3.1 Abstract 73

3.2 Introduction 73

3.3 Materials and Methods 75

3.4 Results 78

3.5 Discussion 85

Acknowledgements 89

Supplementary Material 90

References 91

4 ***In vivo*** **Measurement of Transverse Relaxation Time in the Mouse Brain at 17.6 T*** **99**

4.1 Abstract 99

4.2 Introduction 99

4.3 Materials and Methods 100

4.4 Results 104

4.5 Discussion 108

Acknowledgments 113

Supplementary Material 114

References 116

5 **General Discussion and Future Outlook** **123**

5.1 Monitoring blood flow abnormalities in an AD mouse model 123

5.2 Probing white matter abnormalities in AD using T_2 measurements 124

5.3 *In vivo* Measurement of T_2 in the Mouse Brain at 17.6 T 125

References 131

Summary **136**

Samenvatting **138**

Curriculum Vitae **140**

List of publications **141**

List of abbreviations

µMRI	Magnetic Resonance micro-Imaging
1D	One-dimensional
2D	Two-dimensional
3D	Three-dimensional
AD	Alzheimer's Disease
A	Absolute bias
AC	Anterior commisure
ACA	Anterior cerebral artery
AComA	Anterior communicating artery
ANOVA	Analysis of variance
APP	Amyloid precursor protein
ASL	Arterial Spin Labeling
azACA	Anterior azygos cerebral artery
azPA	Azygos pericallosal artery
Aβ	Amyloid β
BA	Basilar artery
BS	Brain stem
C	Cingulate cortex
CAA	Cerebral amyloid angiopathy
CB	Cerebellum
CC	Corpus callosum
CCA	Common carotid artery
CNR	Contrast to noise ratio
CPMG	Carr-Purcell-Meiboom-Gill
Cpu	Caudate putamen
CSF	Cerebrospinal fluid
CX	Cortex
DKI	Diffusion Kertosis Imaging
DTI	Diffusion tensor imaging
ECA	External carotid artery

FAD	Familial type of AD
FCX	Frontal cortex
FDG	18F-2-fluoro-2-deoxy-D-glucose
FID	Free-induction decay
FOV	Field of view
GABA	γ-Aminobutyric acid
GE	Gradient echo
GFAP	Glial fibrillary acidic protein
GL	Glomerular layer
Gln	Glutamine
Glu	Glutamate
H&E	Hematoxylin and eosin
HC	Hippocampus
HT	Hypothalamus
IBA-1	Ionized calcium binding adaptor molecule 1
ICA	Internal carotid artery
ICC2,1	intra-class correlation coefficient
ISA	image sequence analysis
LFB	Luxol fast blue
LOAD	Late-onset form of the AD
M	Muscle
MAPT	Microtubular associated protein tau
MCA	Middle cerebral artery
MCI	Mild cognitive impairment
MIP	Maximum intensity projection
mIns	Myo-Inositol
MRA	Magnetic resonance angiography
MRI	Magnetic resonance imaging
MRS	Magnetic resonance spectroscopy
MS	Multiple sclerosis
MSME	Multi-Slice, Multi-Echo
MTC	Magnetization Transfer Contrast
NA	Number of averages
NAA	N-acetylaspartate
NAAG	N-acetlyaspartylglutamate
NFT	Neurofibrillary tangle

NMR	Nuclear magnetic resonance
NS	Number of slices
O CX	Occipital cortex
OB	Olfactory bulb
OlfA	Olfactory artery
PCA	Posterior cerebral artery
pCX	Pariatal cortex
PET	Positron emission tomography
PPP	Palatine portion of pterygopalatine
PRESS	Point Resolved Spectroscopy
PrP	Prion protein
PS1, PS2	Presenilin-1, Presenilin-2
RARE	Rapid acquisition with relaxation-enhancement
RF	Radiofrequency pulses
ROIs	Regions of interest
ROS	Reactive oxygen species
rs-fc	Resting state functional connectivity
RSP	Retrosplenial cortex
r_2	Transverse relaxivity
R_2	Transverse relaxation rate
SB	Subiculum
SB/PSB	Subiculum/parasubiculum
SCA	Superior cerebellar artery
SE	Spin echo
SNR	Signal-to-Noise Ratio
T	Tesla
T_1	Longitudinal or spin-lattice relaxation time
T_2	Transverse or spin-spin relaxation time
Tau	Taurine
tCr	Total Creatine (Creatine + Phosphocreatine)
TE	Echo Time
TH	Thalamus
Tg	Transgenic
TR	Repetition Time
WT	Wild-type

1 General introduction

1.1 Alzheimer's disease

Alzheimer's disease is one of the most common causes of dementia, accounting for approximately 60-80% of all cases, with no effective treatment or definitive ante-mortem diagnostic test (1,2). Increasing life expectancy along with the exponential rise of incidence of AD, position the disease as one of the main challenges to society and the health care system at present (1-3). The disease is characterised by abnormalities including a disruption of neuronal function, progressive memory loss, and a gradual cognitive, functional and behavioural deterioration (4). Despite noteworthy progress in unravelling the biological foundations of AD, the etiological mechanisms underlying the neuropathological changes in AD remain unclear. They probably involve environmental, epigenetic as well as genetic factors (5).

AD was named almost 100 years ago after a German physician, Alois Alzheimer (1864-1915) (6). According to Alzheimer's original case report, published in 1907, the disease was characterised by the presence of *miliary foci* and *neurofibrils* in the post-mortem cerebral cortex region of a patient called "Auguste D", who had shown progressive cognitive impairment, focal symptoms, hallucinations, delusions, and psychosocial incompetence (6). In this landmark paper, he remarkably identified the two hallmarks of AD that are known to be common to all forms of AD (7). These hallmarks are extracellular senile plaque deposition, which is mainly composed of Aβ peptide, and intracellular neurofibrillary tangle formation, which is composed of hyperphosphorylated forms of the microtubule associated protein tau (8). Presently, the disease is characterized by presence of these two hallmarks as well as vascular pathology (*e.g.* cerebral amyloid angiopathy) and brain atrophy (Fig. 1.1). These pathologies are often accompanied by gliosis, loss of white matter and synapses. Other features of AD pathologies include Lewy bodies, actin-immunoreactive Hirano bodies and inflammatory processes, *e.g.* oxidative stress and mitochondrial dysfunction (9). Furthermore, failure of neurotransmitter pathways, particularly those of the basal forebrain cholinergic system

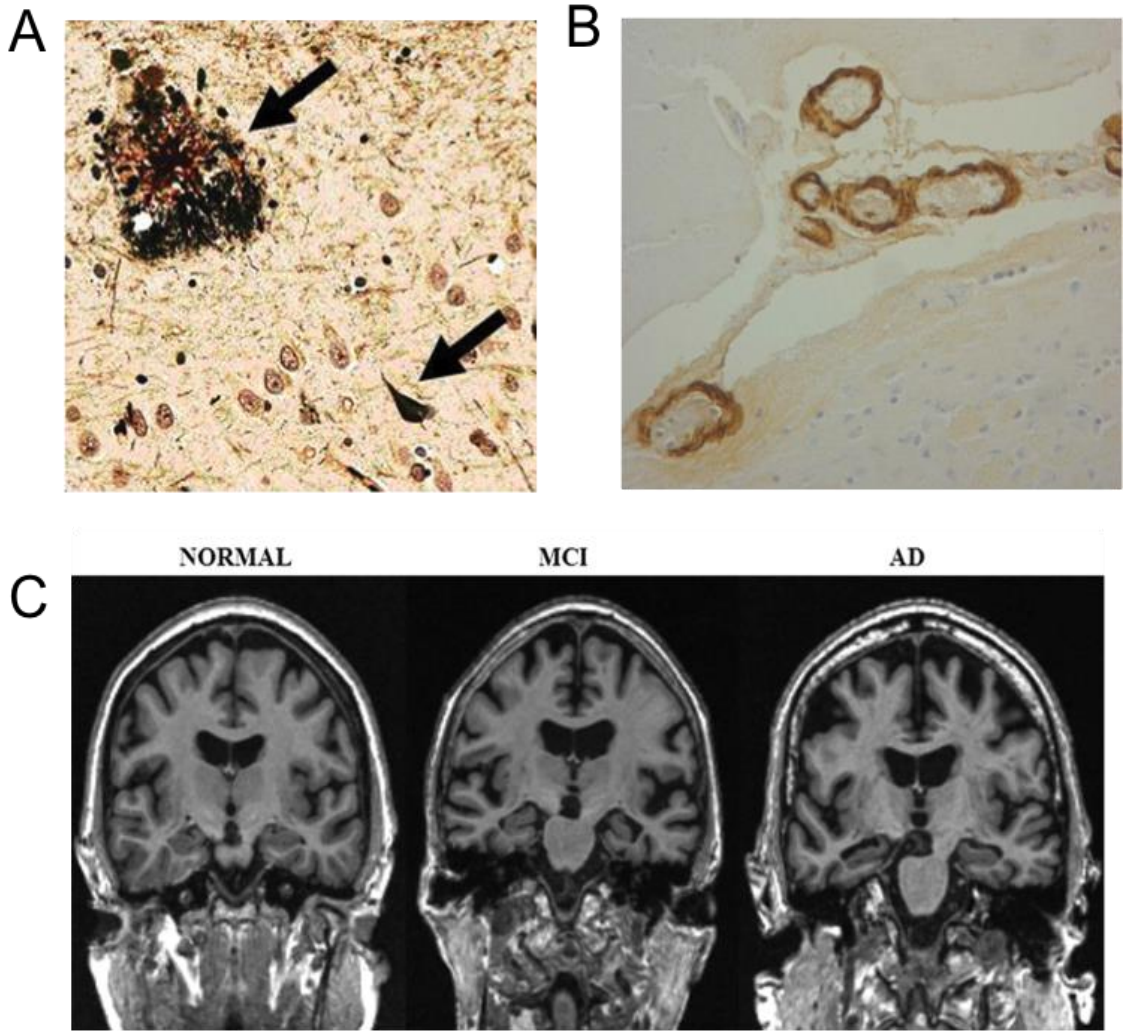

Fig. 1.1. The pathological hallmarks of AD. (A) Photomicrograph shows an Aβ plaque (upper arrow) and a neurofibrillary tangle (lower arrow) in an 85-year-old individual with autopsy-verified AD. (B) Cerebral amyloid angiopathy is commonly observed in mouse models of AD and AD patients. Aβ40 is deposited around cerebral vessels. (C) Atrophy and clinical stage of AD: mild cognitive impairment (MCI) and AD patients showed atrophy compared to normal patients Figs 1.1 A and C are reproduced, with permission, from Jack, 2012 (10). ©rsna.org.

have also been reported (8,11). Since learning and memory are thought to be associated with synaptic efficacy, such as long-term potentiation and long-term depression, synaptic alterations and loss are considered by some investigators to be the major neurobiological cause of cognitive dysfunction in AD (12-14).

While the etiology of the disease has been the subject of considerable debate, the amyloid cascade hypothesis suggests that altered cleavage of amyloid precursor protein, which leads to accumulation of different forms of Aβ peptide in the brain, is central to the pathological cascade that leads AD development (15). This hypothesis was initiated after

isolation of Aβ from cerebrovascular fibrils (16-18). Aβ40 and Aβ42 peptides, which are the major constituents of the Aβ plaques, are derived from an integral type 1 trans-membrane integral protein through sequential cleavage by β-secretase and γ-secretase/presenilin complexes (19,20). These peptides can be either diffuse or compact in nature (17). Aβ peptides have the ability to self-aggregate and form large amyloid fibrils (21). Although both soluble oligomer forms of Aβ and insoluble forms, *i.e.* amyloid fibrils, have been associated with toxicity (22-24), recent studies have suggested that the soluble oligomer forms of Aβ are the most neurotoxic species (25), and have been associated with AD pathogenesis (26,27). How insoluble Aβ causes neurotoxicity is still not fully understood. Interestingly, the presence of insoluble Aβ does not correlate well with cognitive decline in AD (28,29), although some degree of correlation has been shown between Aβ load and cognitive decline (30). The main evidence supporting the amyloid cascade hypothesis has come from identification of mutations in the APP gene (31), which are linked to the early onset of autosomal-dominant familial type of AD (mean age at onset <65 years old). Additional support for this hypothesis comes from the identification of the APP gene's location on chromosome 21. Adults with Down's syndrome (trisomy 21), who have an extra chromosome 21, frequently (60%) develop AD in the sixth decade of life. This is thought to be due to excess production of the APP as a consequence of the trisomy, which leads to formation of amyloid plaques, neuronal cell dead and clinical AD (32).

Under normal physiological conditions, cleavage of APP by α-secretase precludes Aβ formation, whereas all FAD mutations near the β- or γ-secretase cleavage site of APP lead to an increase in the forms of Aβ that can aggregate. The amyloid cascade hypothesis was further supported by identification of mutations in PS1 (33) and PS2 (34), which are proteins that form the catalytic active site of the γ-secretase complex. The mutated form of these proteins can lead to production of more Aβ42, which leads to an increase in Aβ42/Aβ40 ratio (35,36).

Even though mutated genes in FAD are well characterized, the mutations in genes contributing to the disease formation in the LOAD are still under investigation. A few loci, such as the apolipoprotein E, have been derived from genome-wide association studies and have been linked with late onset AD (37,38). These AD gene candidates have been categorized into four groups, namely Aβ metabolism, lipid metabolism, innate immunity, and cell signalling (39) suggesting that multiple factors might be involved in the progression of AD. Clearly, there is an urgent need to have complete appreciation of

the full scope of AD pathology. To this end, it is essential to understand neuropathological factors that contribute to AD pathology. For example, cerebrovascular abnormalities leading to blood flow disturbances and white matter abnormalities, such as demyelination, are considered to be important risk factors for AD. However, how these abnormalities contribute to the disease progression remains unclear.

1.1.1 Cerebrovascular abnormalities and blood flow disturbances

Accumulating evidence suggests that AD is associated with cerebrovascular abnormalities that result in cerebral blood flow disturbances and impaired perfusion (40). The predominant source of cerebrovascular abnormalities of small blood vessels in AD are cerebral amyloid angiopathy and arteriosclerosis (41). Although CAA of the Aβ type is commonly observed in patients with AD and mouse models of the disease (42,43), the *in vivo* relationship between CAA related blood flow alterations in the brain of AD patients and Aβ deposits has not been systematically studied. Understanding the contribution of cerebrovascular abnormalities to the progression of AD is an important step for the development of new treatment strategies to slow and/or prevent the progression of the disease.

CAA is defined as the deposition of Aβ in the cerebral vessel walls (Fig 1.1b). The evidence for CAA in AD brain mainly comes from post-mortem studies (44,45). For example, Yamada has reported that among AD patients, the frequency of CAA was 87% (46). The CAA was associated with blood vessel wall disruption, loss of vascular smooth muscle cell and aneurismal vasodilation that lead to an increased incidence of CAA-related cerebral haemorrhage (47).

CAA usually affects cortical capillaries, small to middle-size arteries of the cerebral cortex and the leptomeninges (48). CAA may cause a failure in perivascular lymphatic drainage pathways, which drains interstitial fluid and solutes drain from the brain. Eventually, failure in drainage pathways could result in decreased clearance of Aβ from the brain (49). Finally, some evidence suggests that CAA could be an important cause of cerebral blood flow disturbances (50). There is a need for direct non-invasive *in vivo* methods to probe blood flow disturbances during AD development. Non-invasive visualization of these disturbances and correlation of them with *in vivo* plaque load could be an important step in the development of new therapies for the prevention of AD but also contribute toward better understanding of AD mechanism.

1.1.2 White matter alterations in AD

Along with grey matter pathologies, white matter microstructural alterations are also implicated in the pathogenesis of AD (51-55). The evidence for white matter alterations came mainly from neuropathological examinations of AD brain (52,54-57). Around 60% of the confirmed cases of AD showed white matter abnormalities, such as myelin breakdown (52). Although there is evidence that white matter abnormalities are associated with cognitive impairment, contribution of these abnormalities to the onset and progression of AD, however, remains unclear (58).

There is converging evidence that different patterns of white matter abnormalities in corpus callosum, which is the largest white matter structure in the brain, are associated with AD progression (59). Since the corpus callosum plays an important role in functional connectivity and cognitive processing, abnormalities in this region may lead to impairment in connections between brain regions, and disturb cognitive process (60). The disconnection between brain regions can play a critical role in progression of AD pathophysiology (59). Even though multiple AD studies have reported microstructural changes in the corpus callosum (61,62), little is known about age-dependent changes and tissue characteristics of these abnormalities. Biochemical analyses of AD white matter revealed that increased Aβ load is accompanied by significant decreases in the amount of myelin basic protein, myelin proteolipid protein, cholesterol, and leads to increased total fatty acid content (57). In addition, neuropathological examination depicted abnormalities, such as gliosis, reduction of oligodendrocytes, partial loss of axons and myelin breakdown in AD white matter (51,52,54,55). To approach these changes *in vivo*, however, is challenging. There is a need for *in vivo* non-invasive techniques to monitor age-dependent microstructural changes in corpus callosum. Altered white matter integrity in corpus callosum might be an early key event in the development of AD pathology. Non-invasive measures may have the potential to follow deteriorating white matter integrity during normal aging and the development of AD and, thus, may be a useful marker to evaluate treatment success.

The lack of histological correlation forms a limitation of *in vivo* studies. Therefore, animal models of AD can serve as valuable biological tools to characterize vascular and white mater abnormalities *in vivo*, and correlate these alterations with histology.

1.2 Mouse models of AD

More than 200 early onset-FAD mutations have been reported in genes producing APP, PS1 and PS2 proteins (39). Based on mutated FAD genes, and mutations on the gene of microtubular associated protein tau, *in vivo* mouse models of AD have been developed. Several groups have combined APP, PS1, PS2 and/or MAPT mutations to generate double or triple transgenic mice (63). Transgenic mouse models of AD play a very fundamental role in the study of pathogenic mechanisms in AD and allow development of novel therapeutic approaches that ameliorate or prevent AD within the next decade (64). These models replicate various features of human AD including senile plaques, cognitive deficits and neurofibrillary tangles pathology (11). A brief summary of the most commonly used transgenic mouse models of AD is presented in Table 1.1 and an updated overview of these models is available on the following website, http://www.alzforum.org, which also shows mouse models based on late-onset AD genetic risk factors, such as apolipoprotein.

Tg2576 is one of the most commonly used and well-characterized transgenic mouse models of the disease (Table 1.1) (65,66). This transgenic mouse line overexpresses a mutant human APP cDNA transgene with the K670M/N671L double mutation (also called Swedish mutation) under the control of the hamster prion protein promoter (65). These mutations lead to formation of soluble Aβ42 and Aβ40 peptides, resulting in Aβ plaque development. Aß deposits start to appear at approximately 9 months of age and are similar to those found in AD. The plaques become visible in cortical and limbic brain regions of Tg2576 mice together with indications of cellular inflammation and behavioural defects (67-69). Neuronal loss, including loss of cholinergic neurons is not a feature of Tg2576 mice whereas CAA and white matter abnormalities are well developed in this model (70,71). Furthermore, development of age-dependent memory defects as assessed by Morris water maze testing, was also demonstrated in this model (65). Many of these findings fit well with biochemical and epidemiological findings in AD. Even though mice carrying FAD mutations represent a very small percentage of AD cases (1%<), the development and progression of AD pathology in these mouse models is of great interest to researchers since mouse models of AD present many pathologic features, similar to those found in patients with LOAD (in which symptoms develop at age 65 or later). Future treatment strategies that are effective in transgenic mouse models carrying FAD genes may provide clues to effective treatments for people with late-onset disease.

Over the past decade, *in vivo* non-invasive magnetic resonance based techniques, such as magnetic resonance imaging and spectroscopy, have emerged as a powerful means to monitor different biological processes longitudinally over time in transgenic mouse models of AD. Current efforts to extend the use of MRI and MRS to evaluate brain changes in these models of AD present a major opportunity to enhance the

Table 1.1: Overview of selected examples of AD mouse models

Species	Promoter	Aβ deposition onset	Transgene characteristics	Remarks	Reference
Tg2576	hamster PrP	9-11 months	human(h) APP695 with Swedish mutation (K670/M671L)	Deterioration in white matter integrity with age (71); CAA formation; memory deficits; brain lipid peroxidation; gliosis.	(65)
APP23	Thy-1.2	6 months	hAPP751 with Swedish mutation	Learning impairment; CAA; gliosis; tau hyperphosphorylation.	(66)
CNRD8	hamster PrP	3 months	hAPP695 with Swedish and Indiana (V717F) mutations	On set of learning impairments is 3 months of age; CAA; gliosis; highly increased Aβ42/ Aβ40 ratio.	(72)
APP/PS 1	Thy-1	1.5 months	hAPP751 with Swedish mutation and PS1 with L166 in a single locus	At 8 month of age cognitive deficits; CAA	(73)
3xTgAD	Thy-1.2	6 months	hAPP695 with Swedish, PS1M146V, and tauP301L	At 4 months of age cognitive deficits; At 6 months of age deficits in long-term synaptic plasticity which correlate with the accumulation of intraneuronal Aβ; Tau pathology develops at 12 months of age.	(74, 75)
5x FAD	Thy-1.2	1.5-2 months	hAPP695 with Swedish, Florida (I716V), London (V717I) and PS1 double mutation (M146L, L286V)	At 1.5 months Aβ42 accumulation, Aβ deposition and gliosis (2 months), synapse degeneration (4 months), neuron loss, and memory deficits (4-5 months).	(76)

development of treatments and provide a potentially efficient approach for investigating promising biomarkers and evaluating candidate therapies. In the following paragraph, a brief introduction of theory of MR-based techniques that were employed in this thesis, and their relevance to mouse imaging is presented.

1.3 Magnetic resonance imaging

Magnetic resonance imaging is a highly advanced non-invasive medical imaging technique, with a very high spatial resolution. It is commonly used in preclinical and clinical studies as a noninvasive tool to investigate the structural, biochemical and functional changes in the brain (77).

The physical principles of MRI are based upon the nuclear magnetic resonance phenomenon, which was first experimentally demonstrated in 1946 independently by Purcell *et al* (78) and Bloch (79). NMR is a physical phenomenon in which nuclei in a magnetic field absorb and re-emit electromagnetic radiation. The nuclei with an odd number of neutrons or protons exhibit spin. One of the most abundant nuclei with spin in the human body is the ^{1}H atom. The ^{1}H nuclear magnetic response to an external magnetic field is one of the strongest found in nature. For this reason protons are the most frequently studied nuclei. Several other nuclei including ^{31}P, ^{13}C, ^{23}Na, and ^{19}F have nuclear magnetic moments corresponding with spin ½ and are also suitable for detection by magnetic resonance (77). However their sensitivity is not as high as for the proton.

When nuclei possessing a spin are placed in an external magnetic field (B_0), the nuclear spins behave like a compass needle or small magnet (Fig. 1.2). The different nuclear states produce a net magnetization vector M_z along the direction of B_0 (Fig. 1.2b). When the magnetization is tilted away from the B_0 direction by a radiofrequency pulse irradiation, the spins will precess around the magnetic field axis (*z*-axis) at a frequency proportional to the magnitude of the external field, according to the Larmor frequency in the MHz to GHz range, determined by γ, the gyromagnetic ratio. Protons have a higher γ (42.575 MHz/T) compared other nuclei of biomedical interest. When an alternating magnetic field (B_1) is applied perpendicular to B_0 by using RF at the Lamor frequency (resonant frequency), the nucleus absorbs the portion of this energy. Subsequently it induces a transition between different spin states. The spins, which have different possible energy states, absorb the energy. This phenomenon can lead to a full or partial inversion of the nuclear spin population, with an increase in the fraction of the higher

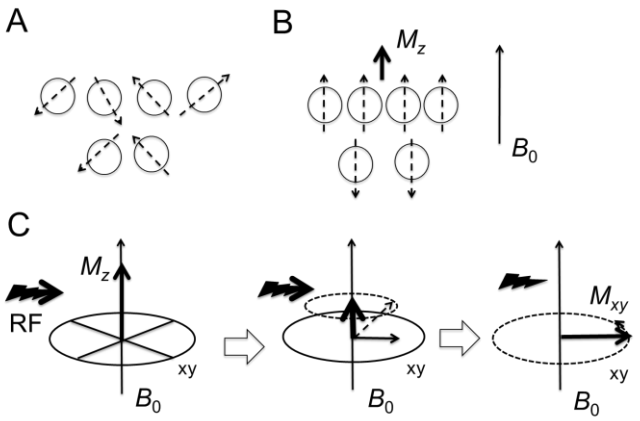

Figure 1.2: (a) Demonstration of MR basics. Protons have a magnetic moment, or "spin". (b) When protons are placed in an external field B_0, a large number of nuclei spins align parallel to the external magnetic field B_0 (along the z-axis), resulting in a net magnetization vector M_z. (c). Application of a 90° RF pulse flips M_z into the xy-plane (perpendicular to B_0), resulting in magnetization vector M_{xy} and phase coherence between spins.

energy state spins at the expense of those in the lower energy states decrease. When B_1 is applied in the presence of B_0, the magnetization vector M_z will rotate away from the *z*-axis towards the *xy*-plane or – *z*-axis (Fig. 1.2c). Immediately after the radio frequency signal is switched off, the nucleus reemits the absorbed energy and the polarization relaxes back to the original alignment (Figs. 1.3a, b). This return to equilibrium is referred to as relaxation. The recovery process of magnetization along the longitudinal axis is called T_1 relaxation, spin-lattice relaxation or longitudinal relaxation (Fig. 1.3b). During this process an exchange of energy occurs between the spin system and the surrounding and is described as:

$$M_z(t) = M_{z_{max}} \left(1 - e^{-\frac{t}{T_1}}\right) \tag{1.1}$$

The number T_1 represents the time it takes for 63% of the nuclear magnetization associated with the excited protons to realign with the B_0 (80). The transverse (or spin-spin) relaxation time T_2 reveals loss of the net magnetization in the *xy*-plane, due to dephasing (Fig. 1.3c). During T_2 relaxation, the energy is transferred between neighbouring nuclear spins. The number T_2 represents the time for M_{xy} to drop to 37% of its original magnitude due to dephasing (80). During dephasing, the net magnetization in the xy-plane decays exponentially to zero over time. The rate at which this occurs is dependent on T_2 and the T_2 process is described as:

$$M_{xy}(t) = M_{xy_{max}} e^{-\frac{t}{T_2}}. \tag{1.2}$$

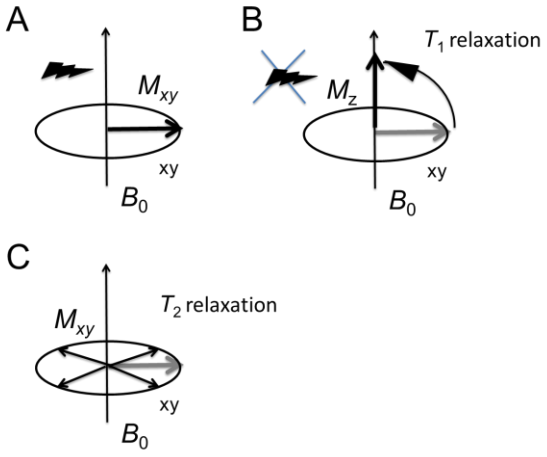

Fig. 1.3. (a) Application of a 90^0 radiofrequency pulse produces magnetization in the xy plane M_{xy}. When RF pulse is stopped, the nucleus reemits the absorbed energy and relaxes back to the original alignments at a rate determined by T_1 (b) and T_2 (c) relaxation times.

When an image is acquired, T_1 or T_2 or a combination determines the amplitude of the MR signal and intensity of the image. Relaxation time parameters form the basis of tissue contrast in MRI, which allows identification of white and gray matter regions. During a relaxation period, the nuclei lose energy by emitting their own RF signal. This NMR signal is referred to as the free-induction decay. In MRI, the FID signal is measured by a surface or volume coil placed on or around the object being imaged. This measurement is processed or reconstructed to obtain grey-scale MR images. The resonance condition forms the basis of MRI, which can form an image by representing a display of spatially localized signal intensities. The image formation is achieved in two steps. First a slice of tissue is selected for imaging. Subsequently the location of the signal is determined through the use of a nonuniform magnetic field created by magnetic field gradients, which causes the spin location to be encoded in terms of its Larmor frequency (77). The gradient field is parallel to B_0 and its strength varies with position relative to B_0. The gradient has three components, G_x, G_y, and G_z, associated with the *x*, *y*, or *z* spatial axis, respectively. When a magnetic field gradient along the *z* axis formed, the magnitude of the applied magnetic field changes in proportion to the *z* axis while remaining constant for any point in any *xy* plane (77). Application of the gradient field allows the spins to experience different field strengths, which depend on the location of the spins within the gradient field. The gradient direction (x, y, z) determines the slice orientation, whereas the gradient amplitude together with the RF pulse characteristics determine both the slice thickness and slice position. Two most commonly employed pulse sequences for MRI are the spin echo sequence and the gradient echo sequence (Figs 1.4a,b) (81,82).

SE sequences use two RF pulses, an excitation pulse, which is a slice selective 90° pulse, and one or more 180° refocusing pulses that generate spin echoes. The two important parameters in a SE sequence are the repetition time and the echo time. TR is defined as the time between successive excitation pulses for a given slice. TE is the time from the

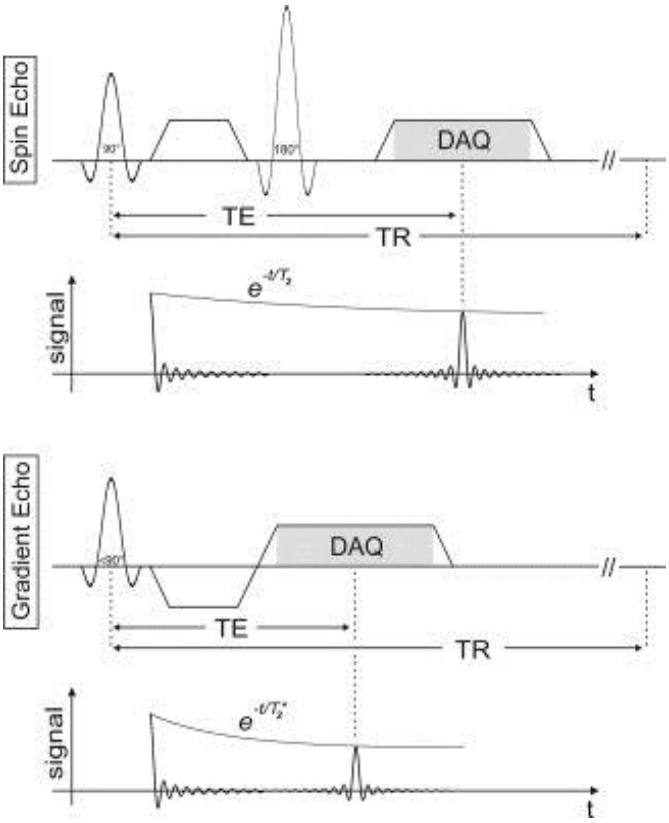

Figure 1.4: Simplified spin echo (top) and gradient echo (bottom) pulse sequence diagrams. The basic difference between gradient echo and spin echo imaging is related to the fact that echo formation is a result of a single RF pulse and gradient reversal while spin echo imaging uses two RF pulses, i.e., a second 180° pulse, for echo generation. As a result, the gradient echo signal intensity is determined by T-decay and, contrary to the spin echo T_2-weighted signal intensity, field inhomogeneity effects are not refocused at the time of signal formation. DAQ reflects the period of data acquisition. Reproduced, with permission, from Markly and Leupold, 2012 (81). © John Wiley & Sons, Inc.

excitation pulse to the echo maximum. This sequence can be adjusted to give T_1-weighted, proton density and T_2-weighted images. The images acquired with the SE sequence are less sensitive to susceptibility artifacts than the data obtained with gradient echo sequences. In the SE sequence the 180° refocusing pulse can correct the susceptibility-induced dephasing of spins from T_2* effects (82). The GE sequence is used in a wide variety of imaging techniques, such as MR angiography. This sequence uses only a single selective pulse, which changes from 10° to 90°, in combination with readout gradient reversal. This sequence provides a fast imaging possibility with short TR (82).

1.3.1 Rapid acquisition with relaxation-enhancement imaging

Rapid acquisition with relaxation-enhancement imaging (83,84) is a fast magnetic resonance spin echo-imaging method. It is based on the Carr-Purcell-Meiboom-Gill echo train in which multiple spin echoes are generated by employing multiple 180° refocusing pulses. This imaging method delivers excellent T_2 contrast, which makes this method ideal for screening in most neurodegenerative disorders.

The primary contrast in RARE is T_2-based, however the contrast in the final image can be modified depending on the choice of TE, and TR. T_2-weighted images usually have a long TR >1500 ms and long TE, whereas a T_1-weighted image has a short TR <500msec and short TE. In a T_2-weighted image, the elements with long T_2 will appear bright, and elements with a short T_2 will appear dark. TE refers to the time between the excitation pulses and the echo. A practical implementation of RARE imaging in visualizing Alzheimer's Aβ plaques is demonstrated in Chapter 2.

1.3.2 Magnetic resonance angiography

Magnetic resonance angiography offers a non-invasive approach to visualize cerebrovasculature and blood flow defects. One well-established MRA technique is the time of flight angiography (Fig. 1.5), which is commonly employed for the clinical evaluation of many vascular diseases (85). This technique is based on a nuclear magnetic resonance phenomenon in flowing liquids (86). This phenomenon, known as the time-of-flight effect, arises from the saturation of stationary tissue during RF pulse application, which leads to a net magnetization approaching zero and weak signal. The RF pulses, however, cannot fully saturate a flowing liquid, where the polarization is refreshed continuously with spins with full magnetization, and eventually this increases the signal (Fig. 1.4) (81,87). This phenomenon forms the basis of the contrast mechanism between a blood vessel and stationary tissue (85,87).

The time of flight MRA method is sensitive to fast flowing blood. In this method, vessel visibility depends on several object parameters, such as velocity of blood flow, relaxation times (T_1, T_2, T_2*) of tissue and vessel diameter, and the imaging parameters, such as flip angle, slice profile, thickness and orientation, voxel size or field of view, resolution, TR, and TE (85,88,89). For example, increasing TR and decreasing the flip angle increases the visibility of vessels with lower lumen diameter where the blood flow is slow (88,90). In addition, moving to higher fields can significantly improve vessel visibility. Higher magnetic field strengths provide a double advantage for vessel/tissue contrast (91). First, an increase in stationary tissue T_1 value with increasing magnetic field strength provides better suppression of tissue signal. Second, higher magnetic field strength increases the magnetization of the flowing blood and eventually this leads to a stronger signal from the

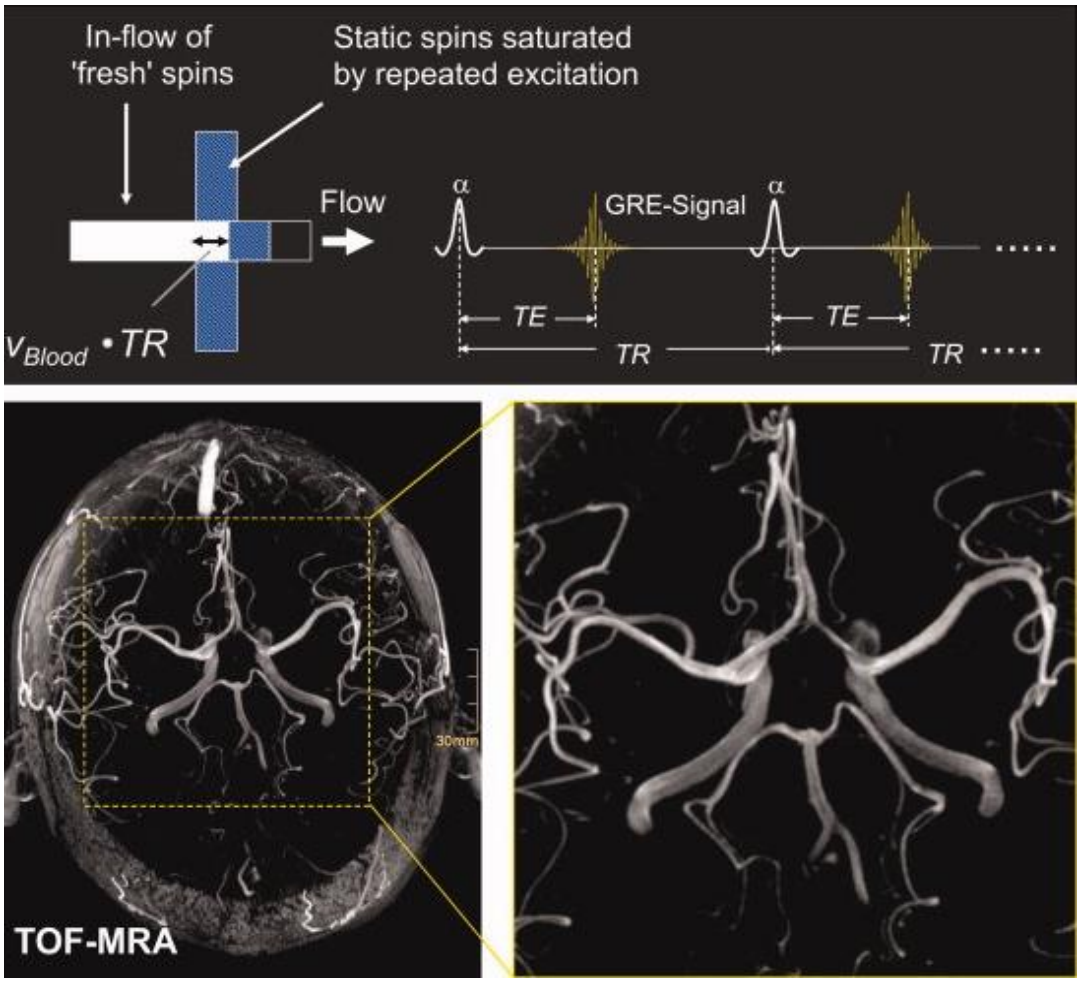

Figure 1.5. In-flow enhancement in GRE imaging results in bright signal of blood entering the imaging slice. In combination with saturation of static tissue this effect can be exploited to provide high blood-tissue contrast as in time of flight MR angiography. V_{blood} *= Velocity of blood; TR = Repetition time; TE = Echo time; α = flip angle. Reproduced, with permission, from Markly and Leupold, 2012 (81). © John Wiley & Sons, Inc*

flowing blood (91).The 3-D MRA acquired with 3D gradient echo sequences provides visualization of the large and small size arteries in a particular volume with a superior resolution (Fig. 1.4) (81,85,91). Additional post-processing of cross-sectional slices of these images with special techniques such as a maximum intensity projection algorithm allows 3D visual inspection of the vessel anatomy at an arbitrary view angle (92). Chapter 2 contains a practical implementation of this technique.

1.3.3 T_2 relaxation mapping

As described in the previous chapter, the relaxation times (*e.g.* T_1 and T_2) are intrinsic tissue parameters that are sensitive to changes in the biophysical water environment, and help determine the contrast in MRI (93). For example, myelin breakdown increases the T_2 relaxation time. Thus T_2 mapping has been proposed as a sensitive tool to investigate microstructural changes in white matter during AD progression (See Chapter 3, 4).

The T_2 relaxation time can be measured using multi-echo data sets acquired during a spin echo, enabling time efficient multi-slice imaging. T_2 can be calculated using different fit functions. In this thesis, to calculate T_2 maps of brain regions, regions of interest were drawn manually on the images by using an image sequence analysis tool package (Paravision 5, Bruker), which uses a fit function [$y= A+C*\exp(-t/T_2)$], where A is the absolute bias, C represents the signal intensity, and T_2 is the transverse relaxation time. Estimating true (absolute) T_2 values of tissue is challenging in biological systems due to increased field inhomogenities and magnetic susceptibility differences, which lead to signal loss. The spin echo technique used in this thesis rephrases the signal before collection, which decreases the effect of susceptibility differences on the signal (81,82). Therefore the calculated T_2 is closer to the true T_2 values than for images acquired with traditional methods.

1.3.4 Magnetic resonance spectroscopy

Magnetic resonance spectroscopy is a specialized method that offers a non-invasive means for the characterization of metabolic composition of tissues from the particular region of interest *in vivo*. This method along with MRI has been commonly employed in preclinical studies to study a variety of neurodegenerative disorders such as Alzheimer's disease. MRS and MRI are closely related techniques. The same scanner is used for both MRI and MRS. Both techniques use signals from the same nuclei, in particular ^{1}H. One of the main differences between MRI and MRS is that while MRI provides information on the physical-chemical state of tissue and on motion, MRS provides only information about the chemical composition of tissue and is less sensitive than MRI.

The MR spectra are acquired by applying a RF pulse via a surface or volume coil at a particular resonant frequency to detect the signal of specific nuclei (*e.g.*, ^{1}H, ^{31}P, etc.) in the region of interest. When the excitation RF pulse is turned off, the spins relax to their equilibrium state by emitting RF waves. These RF waves are collected as an FID in the

time domain by the RF coil (94). The sensitivity of the experiment can be increased by repeating the experiment and accumulating the FIDs. The FIDs contain (1) intensity, (2) frequency, (3) half-life, or $t_{½}$ and (4) phase information. The FID is converted to frequency-domain data (*i.e.* the spectrum) using a technique called Fourier transformation where the data are presented in the form of a one dimensional or two dimensional spectrum.

1.4 Monitoring AD using MR- based techniques

In recent years increasing effort has been directed towards the development of non-invasive high resolution *in vivo* neuroimaging methods to monitor pathological changes in AD brain. Two most commonly employed advanced imaging technologies are PET and MR-based techniques, such as MRI. Unlike PET, MRI uses non-ionizing radiofrequency pulses and a strong magnetic field to acquire brain images with high spatial resolution. With continuing developments in the precision of MRI, it is increasingly feasible to use these techniques in the study of subtle brain changes during AD progression (10,95).

Currently a variety of MR based techniques is commonly employed to characterize the anatomical, functional, neurochemical and blood flow changes observed during AD progression. For example, progressive cerebral atrophy, such as hippocampal atrophy, is a characteristic feature of AD, which can be detected with structural MRI (10,96,97). Non-invasive, *in vivo* methods to image Aβ plaque-load would be very valuable for monitoring Aβ formation with age in the same patient, and to evaluate the success of treatments for plaque clearance (98). MRI can detect Aβ plaque-load with higher spatial resolution compared to PET without using ionization radiation. Theoretically, MRI has the potential to resolve individual Aβ plaques, which range from 2 to 200 μm in size (99). Until now two main strategies have been employed to detect Aβ plaques in AD brain. These strategies involve contrast-enhancing agents, which bind to Aβ plaques, and susceptibility artefacts. *In vivo* MRI methods to image Aβ plaques without contrast agents in human AD patients are underway (100) but are currently not available in clinical magnetic fields. Recent *ex vivo* and *in vivo* higher field MRI studies using susceptibility artefacts have visualized Aβ plaques in the brain of AD mice as hypointense signals (98,101,102). These studies suggested that the signal hypointensities observed on MRI images represent Aβ plaques, containing metals, particularly iron. In addition, reduction of the water content in Aβ plaques can be the source of signal

hypointensities observed in MRI (103). Also, indirect MRI techniques, such as diffusion kurtosis imaging, magnetization transfer contrast and relaxation time maps have been employed to detect amyloid load in AD brains (10).

Microstructural changes, such as white matter degeneration, which accompany AD development, can be detected by intrinsic relaxation time parameters or DTI. DTI maps diffusion processes of water molecules in the brain, which serves as useful tools to detect changes in white matter integrity. DTI is being tested in an attempt to distinguish patients with AD from healthy elderly individuals (10). The neurobiological substrate of diffusion changes in AD remains unresolved. It remains unclear whether DTI has sufficient sensitivity to separate AD patients from controls, and is awaiting sufficient validation to be accorded into wider clinical use (10). Recent studies depicted that *in vivo* quantitative T_2 relaxation measurements are capable of characterizing white matter abnormalities in demyelinating disorders such as Multiple Sclerosis (104). However, few studies have employed T_2 measurement to asses white matter integrity in AD (105). Studies to characterize these changes longitudinally are missing. Functional MRI task free and task-based methods, which measure brain activity, are under evaluation to investigate their potential to discriminate different states of AD from healthy elderly individuals. In particular, a task free method, namely the resting state functional connectivity MRI method is increasingly employed to investigate subtle brain network abnormalities in AD (106). Loss of intra-network connectivity in large scale networks, including the default mode network, dorsal attention network, control network, salience network, and sensory motor network, has been shown in AD using the rs-fc MRI method, suggesting that soluble and/or insoluble Aβ causes disordered neural communication (106). The diagnostic accuracy of this method is under evaluation.

Biochemical changes in the brain can be measured by employing MR spectroscopy, which provides information about brain chemistry. Proton (^{1}H) MRS, among other spectroscopy methods, is one of the most commonly employed *in vivo* MR techniques for diagnosis of AD. This method has great potential to be used in clinical diagnosis of AD in the near future. For example, a decrease in NAA/mIns ratio provides very high sensitivity and specificity to distinguish AD from healthy individuals (95,107,108). Several cerebrovascular alterations, such as CAA, accompany AD neuropathology in AD (42,46,70). Cerebral blood flow abnormalities can be detected non-invasively *in vivo* in transgenic mouse models of AD (109) and human AD patients (110) by a variety of methods such as MRA and arterial spin labelling. A brief overview of MR based

techniques for visualizing blood flow and white matter abnormalities to assess AD pathology is given below.

1.4.1 MRA to detect blood flow abnormalities

The role of cerebrovascular abnormalities in the etiology of AD is increasingly becoming a topic of research (111). How CAA related abnormalities in cerebral blood flow contribute to the onset and progression of AD, and the interrelationship between these abnormalities and parenchymal amyloid load, however, remains unclear. *In vivo* non-invasive methods to visualize the blood flow abnormalities in brain are needed to address these questions.

Cerebrovascular blood flow abnormalities can be detected without contrast agent administration via MR-based techniques such as MRA and ASL. MRA of the mouse brain can be performed in spontaneously respiring animals. Determining the basal perfusion alterations in mice using ASL techniques is, however, challenging. Stable physiological conditions are warranted during *in vivo* scanning. This can be obtained by intubating and ventilating the animal, allowing a more controlled setting. However, these procedures are not routinely performed. MRA has been employed to investigate vascular alterations in a variety of mouse models of AD (109,112,113) and in clinics (114,115), the resolution of these studies, however, was hampered by the use of low magnetic field strengths. The MRA studies at ultra high magnetic field strengths, such as 17.6 T, which can provide better visualization of moderate to smaller vessels, are missing. The ability of the ultra-high field MRA to detect small flow disturbances makes it attractive as a diagnostic tool in AD (109). The application of this method in a mouse model of AD at 17.6 T is presented in Chapter 2.

1.4.2 T_2 measurements to assess white matter abnormalities

Tissue relaxation time parameters, such as T_1 and T_2, are sensitive to the biophysical environment, and can provide tissue specificity allowing enhanced characterization of pathological tissue (116). Thus a variety of aging and AD studies have employed relaxation time data in order to detect changes in tissue integrity (117-123). However, changes in relaxation values of white matter of AD brain with age and correlation of these values with AD pathological features, such as amyloid load and demyelination, is not yet well characterized.

Table 1.2: Summary of T_2 relaxometry studies in AD mouse models of AD and wild-type mice

Model name	Longi-tudinal	Age (month)	Relaxation Parameters	Field strength	Region of interest	Remarks	Refer-ences
B6/SW	No	1.5 and 12	T_1,T_2	7T	WT: CC; GM: HC, RSP, CX	Decrease in T_2: CC*	(124)
APP_{695}/PS1 PS1, NTg	No	16-23	T_1,T_2	7T	WT: CC; GM: HC, C RSP	Decrease in T_2: C*,RSP*, HC* (PS/APP vs. NTg)	(125)
APP_{V717I} NTg	No	24	T_2*	7T	GM: CX, TH	Decrease in T_2*: TH (statistical test is N/A)	(102)
APP_{695}, NTg	Yes	12,14,16,18	T_2	9.4T	GM: HC, CX	Decrease in T_2: HC *, CX * (at 16 and 18 months of age)	(126)
APP_{751}/PS1 PS1	No	~7-11 and ~15-21	T_1,T_2	4.7T	WM: CC; GM: Cpu, HC, SB, TH, pCX, vCX, P,	Decrease in T_2: SB* Decrease in T_1: pCX*, CC* (at 15-21 months of age)	(127)
APP/PS1 NTg	No	6, 12, 18	T_1*rho*	4.7T	GM: CX, HC, TH	Decrease in T_1*rho*: CX*, HC*, TH* (at 12 and 18 months of age)	(128)
APP_{751}/PS1 PS1	No	~4-8 (mean age ~5)	T_2	4.7T	GM: CX, SB	Decrease in T_2: SB*	(129)
APP_{695}, APP/PS1 PS1, NTg	Yes[a],	~1.5-2, ~8-11, ~15-19	T_2	7T	GM: CX, HC	Decrease in T_2: CX*, HC* (NTg vs. PS/APP at all ages)	(130)
APP_{695}/PS2 NTg	Yes	10, 12, 17	T_1, T_2, T_2*	7T	GM: BS, CB, O CX, TP CX, F CX, SB/PSB, HC, TH, BS WT and GM: CB	T_2: CX*, SB/PSB* T_1: CX* (at 12 and 17 months of age)	(131)
APP_{695}/PS1 NTg	No	~5	T_2	7T	GM: CX, HC V	CX*, HC*, V*	(132)

BS= Brainstem, C= Cingulate cortex, CB= cerebellum, CC= Corpus callosum, Cpu= Caudate putamen, CX= Cortex, GM= Gray matter, HC = Hippocampus, FCX= Frontal cortex, OCX= Occipital cortex, pCX= Pariatal cortex, RSP= Retrosplenial Cortex, , TH= Thalamus, SB =Subiculum, SB/PSB= Subiculum/parasubiculum, TPCX= Temporoparietal cortex, V= Ventricle, vCX =Visual cortex,WT= White matter . [a] Some mice were studied cross-sectional.

A variety of transgenic mouse models of AD have been used to investigate the correlation between intrinsic relaxation values and AD pathology (*e.g.*, demyelination, gliosis, Aβ plaque deposition). An overview of these studies in AD mice is depicted in Table 1.2.

The changes in gray matter are well characterized by these studies using relaxation values, *e.g.*, T_1, T_2, and T_2* and T_1rho. However, little is known about changes in the

white matter. There is evidence that altered white matter integrity, such as demyelination, is an early event in the course of the AD, but the nature of these changes and their contribution to the onset and progression of the disease remains unclear (52,133-136). There is an emerging need for detection of these changes *in vivo* with MRI, which has potential to aid early diagnosis of AD. T_2 values are sensitive to myelination and demyelination processes (124).

Thus, T_2 measurements can serve as a sensitive non-invasive tool to longitudinally monitor subtle microstructural changes in corpus callosum and other white matter regions. However, a proper longitudinal study, which follows T_2 changes in white matter integrity of AD mice models, is missing.

1.4.3 Ultra-high field MRI in mouse models of AD

Transgenic mouse models of human diseases have been commonly employed in biomedical research for testing treatments and monitoring disease progression. Being a non-invasive method, MRI allows longitudinally monitoring of structural and functional changes in these murine models of human diseases. The small size of the mouse brain however, has considerable limitations such as low signal-to noise ratio for a given measurement time. To overcome these limitations, several strategies can be employed such as conventional signal averaging, using a cryogenic radio frequency coil, or moving to higher magnetic field strength. In particular, the use of ultra-high magnetic fields (≥7T) in MRI and MRS will be highly beneficial in order to obtain well-defined chemical shift spectra, larger data acquisition rates, higher-resolution and signal-to-noise ratio (137). Currently the best available horizontal MRI system operates at field strength of 14.1 T, whereas vertical systems are at much higher field strength (≥17.6 T). Use of ultra-high systems might cause a paradigm shift in preclinical AD studies through the *in vivo* observation of metabolism and subtle microscopic tissue changes. Many MR based techniques benefit from ultra-high fields. In particular, MRA clearly benefits from high magnetic field. Increased T_1 relaxation time and high magnetization at higher fields provides improved higher vessel-to-tissue contrast and the signal- to-noise ratio that may contribute to the improved quality of MRA (138). Thus abnormalities in smaller vessels can be monitored without the use of contrast enhancing agents. In addition to increased SNR, *in vivo* localized MRS, which provides the unique prospect of longitudinally monitoring brain metabolism in living animals or humans, benefits from high magnetic fields from the increased spectral resolution (137)

Relaxation time parameters (*e.g.* T_1 and T_2) are known to change substantially with increasing field strength in biological tissues, but the amount of change depends, among other factors, on the biophysical water environment and the presence of metal ions such as iron in such a way that it cannot be estimated accurately with a theoretical calculation (139) . Thus, an accurate determination of proton relaxation times with ultra high field strength MRI is an essential first step in exploring the capabilities of ultra high field MRI. While such values have been reported in lower field strength, to our knowledge normative T_2 values of healthy mouse brain for 17.6 T are currently not available (See Chapter 4).

1.5 Thesis scope

An advanced characterization of AD pathology can be achieved by application of non-invasive *in vivo* imaging methods, such as MRI, to monitor the disease progression longitudinally in transgenic mouse models of AD. In particular *in vivo* imaging of these mice models at ultra high magnetic field strengths can permit a better understanding of the underlying cellular mechanism of AD. This knowledge can be used to develop potential biomarkers and promising treatment strategies to impede and/or prevent the disease progression.

There are important developments in AD translational research, especially with respect to the *in vivo* imaging of vascular defects and white abnormalities using MRI in transgenic mouse models of AD. AD is linked to abnormalities in the vascular system such as CAA. Although CAA is very common in the advanced stages of AD, its contribution to the onset and progression of AD remains unclear. In addition, the *in vivo* relationship between Aβ plaque deposition in brain tissue and its correlation with blood flow alterations is unknown. Longitudinal high-resolution MR studies to monitor blood flow abnormalities are required to study blood flow abnormalities and to investigate whether they are associated with Aβ plaque deposition. Furthermore there is a need for monitoring white matter changes in corpus callosum with age during AD development. The converging evidence suggests that different patterns of white matter abnormalities in corpus callosum are associated with AD progression (59). These changes might be an early biomarker for AD. How and when the integrity of white matter decreases in corpus callosum remains unclear.

Since ultra-high field systems are increasingly used in AD research, there is a need for accurate determination of proton relaxation times at 17.6 T to explore the capabilities of ultra high field MRI. While such values have been reported at lower field strength, to our knowledge normative T_2 values of healthy mouse brain for ultra high magnetic field strengths (17.6 T) are currently not available. These values can serve as normative values against which disease related relaxation changes can be assessed in mice.

The aim of this thesis is to implement and optimize MR based techniques, namely MRA and T_2 relaxometry at high and ultra high magnetic field (*i.e.* 9.4 and 17.6 T) to longitudinally monitor blood flow and white matter abnormalities in a mouse model of AD to establish potential neuroimaging biomarkers.

In **Chapter 2**, high resolution μMRA at 17.6 T has been optimized and successfully implemented to longitudinally monitor morphological changes in cerebral arteries in a Tg2576 mouse model. These changes were correlated with Aβ plaque development. In **Chapter 3** *in vivo* T_2 changes were longitudinally monitored in the corpus callosum of the Tg2576 mice. Since T_2 values have been shown to be sensitive to axonal injury, gliosis and demyelination, probing changes in T_2 values will provide a sensitive marker of dynamic microscopic changes in the corpus callosum, and will eventually yield new insights into the pathology underlying AD. In **Chapter 4**, regional T_2 values of the healthy mouse brain were established at 17.6 T, and regional brain T_1 and T_2 changes were followed with age. The estimates of *in vivo* T_1 and T_2 will be useful to optimize pulse sequences for optimal image contrast at 17.6 T and will serve as baseline values against which disease related relaxation changes could be assessed in mice. **Chapter 5** provides a general discussion to the work presented in this thesis, and presents some future prospects.

References

1. Ott A, Breteler MM, van Harskamp F, Claus JJ, van der Cammen TJ, Grobbee DE, Hofman A. Prevalence of Alzheimer's disease and vascular dementia: association with education. The Rotterdam study. BMJ 1995;310(6985):970-973.
2. Polvikoski T, Sulkava R, Myllykangas L, Notkola IL, Niinisto L, Verkkoniemi A, Kainulainen K, Kontula K, Perez-Tur J, Hardy J, Haltia M. Prevalence of Alzheimer's disease in very elderly people: a prospective neuropathological study. Neurology 2001;56(12):1690-1696.
3. De Deyn PP, Goeman J, Vervaet A, Dourcy-Belle-Rose B, Van Dam D, Geerts E. Prevalence and incidence of dementia among 75-80-year-old community-dwelling elderly in different districts of Antwerp, Belgium: the Antwerp Cognition (ANCOG) Study. Clin Neurol Neurosurg 2011;113(9):736-745.
4. McKhann G, Drachman D, Folstein M, Katzman R, Price D, Stadlan EM. Clinical diagnosis of Alzheimer's disease: report of the NINCDS-ADRDA Work Group under the auspices of Department of Health and Human Services Task Force on Alzheimer's Disease. Neurology 1984;34(7):939-944.
5. Reitz C, Brayne C, Mayeux R. Epidemiology of Alzheimer disease. Nature reviews Neurology 2011;7(3):137-152.
6. Alzheimer A, Stelzmann RA, Schnitzlein HN, Murtagh FR. An English translation of Alzheimer's 1907 paper, "Uber eine eigenartige Erkankung der Hirnrinde". Clin Anat 1995;8(6):429-431.
7. Weber MM. Aloys Alzheimer, a coworker of Emil Kraepelin. J Psychiatr Res 1997;31(6):635-643.
8. McGowan E, Eriksen J, Hutton M. A decade of modeling Alzheimer's disease in transgenic mice. Trends Genet 2006;22(5):281-289.
9. Hyman BT, Phelps CH, Beach TG, Bigio EH, Cairns NJ, Carrillo MC, Dickson DW, Duyckaerts C, Frosch MP, Masliah E, Mirra SS, Nelson PT, Schneider JA, Thal DR, Thies B, Trojanowski JQ, Vinters HV, Montine TJ. National Institute on Aging-Alzheimer's Association guidelines for the neuropathologic assessment of Alzheimer's disease. Alzheimer's & dementia : the journal of the Alzheimer's Association 2012;8(1):1-13.
10. Jack CR, Jr. Alzheimer disease: new concepts on its neurobiology and the clinical role imaging will play. Radiology 2012;263(2):344-361.

11. Van Dam D, De Deyn PP. Animal models in the drug discovery pipeline for Alzheimer's disease. British journal of pharmacology 2011;164(4):1285-1300.
12. Small DH, Mok SS, Bornstein JC. Alzheimer's disease and Abeta toxicity: from top to bottom. Nat Rev Neurosci 2001;2(8):595-598.
13. Selkoe DJ. Alzheimer's disease is a synaptic failure. Science 2002;298(5594):789-791.
14. Arendt T. Synaptic degeneration in Alzheimer's disease. Acta Neuropathol 2009;118(1):167-179.
15. Karran E, Mercken M, De Strooper B. The amyloid cascade hypothesis for Alzheimer's disease: an appraisal for the development of therapeutics. Nat Rev Drug Discov 2011;10(9):698-712.
16. Glenner GG, Wong CW. Alzheimer's disease and Down's syndrome: sharing of a unique cerebrovascular amyloid fibril protein. Biochem Biophys Res Commun 1984;122(3):1131-1135.
17. Glenner GG, Wong CW. Alzheimer's disease: initial report of the purification and characterization of a novel cerebrovascular amyloid protein. Biochem Biophys Res Commun 1984;120(3):885-890.
18. Hardy J. Testing times for the "amyloid cascade hypothesis". Neurobiol Aging 2002;23(6):1073-1074.
19. Di Carlo M. Beta amyloid peptide: from different aggregation forms to the activation of different biochemical pathways. European biophysics journal : EBJ 2010;39(6):877-888.
20. Nunan J, Small DH. Regulation of APP cleavage by alpha-, beta- and gamma-secretases. FEBS Lett 2000;483(1):6-10.
21. Burdick D, Soreghan B, Kwon M, Kosmoski J, Knauer M, Henschen A, Yates J, Cotman C, Glabe C. Assembly and aggregation properties of synthetic Alzheimer's A4/beta amyloid peptide analogs. J Biol Chem 1992;267(1):546-554.
22. Lambert MP, Barlow AK, Chromy BA, Edwards C, Freed R, Liosatos M, Morgan TE, Rozovsky I, Trommer B, Viola KL, Wals P, Zhang C, Finch CE, Krafft GA, Klein WL. Diffusible, nonfibrillar ligands derived from Abeta1-42 are potent central nervous system neurotoxins. Proc Natl Acad Sci U S A 1998;95(11):6448-6453.

23. Yankner BA, Dawes LR, Fisher S, Villa-Komaroff L, Oster-Granite ML, Neve RL. Neurotoxicity of a fragment of the amyloid precursor associated with Alzheimer's disease. Science 1989;245(4916):417-420.
24. Frautschy SA, Baird A, Cole GM. Effects of injected Alzheimer beta-amyloid cores in rat brain. Proc Natl Acad Sci U S A 1991;88(19):8362-8366.
25. Lue LF, Kuo YM, Roher AE, Brachova L, Shen Y, Sue L, Beach T, Kurth JH, Rydel RE, Rogers J. Soluble amyloid beta peptide concentration as a predictor of synaptic change in Alzheimer's disease. Am J Pathol 1999;155(3):853-862.
26. Cleary JP, Walsh DM, Hofmeister JJ, Shankar GM, Kuskowski MA, Selkoe DJ, Ashe KH. Natural oligomers of the amyloid-beta protein specifically disrupt cognitive function. Nat Neurosci 2005;8(1):79-84.
27. Hefti F, Goure WF, Jerecic J, Iverson KS, Walicke PA, Krafft GA. The case for soluble Abeta oligomers as a drug target in Alzheimer's disease. Trends in pharmacological sciences 2013;34(5):261-266.
28. Braak H, Braak E. Evolution of neuronal changes in the course of Alzheimer's disease. Journal of neural transmission Supplementum 1998;53:127-140.
29. Terry RD, Masliah E, Salmon DP, Butters N, DeTeresa R, Hill R, Hansen LA, Katzman R. Physical basis of cognitive alterations in Alzheimer's disease: synapse loss is the major correlate of cognitive impairment. Ann Neurol 1991;30(4):572-580.
30. Cummings BJ, Pike CJ, Shankle R, Cotman CW. Beta-amyloid deposition and other measures of neuropathology predict cognitive status in Alzheimer's disease. Neurobiol Aging 1996;17(6):921-933.
31. Levy E, Carman MD, Fernandez-Madrid IJ, Power MD, Lieberburg I, van Duinen SG, Bots GT, Luyendijk W, Frangione B. Mutation of the Alzheimer's disease amyloid gene in hereditary cerebral hemorrhage, Dutch type. Science 1990;248(4959):1124-1126.
32. Hyman BT. Down syndrome and Alzheimer disease. Progress in clinical and biological research 1992;379:123-142.
33. Sherrington R, Rogaev EI, Liang Y, Rogaeva EA, Levesque G, Ikeda M, Chi H, Lin C, Li G, Holman K, Tsuda T, Mar L, Foncin JF, Bruni AC, Montesi MP, Sorbi S, Rainero I, Pinessi L, Nee L, Chumakov I, Pollen D, Brookes A, Sanseau P, Polinsky RJ, Wasco W, Da Silva HA, Haines JL, Perkicak-Vance MA, Tanzi RE, Roses AD, Fraser PE, Rommens JM, St George-Hyslop PH. Cloning of a

gene bearing missense mutations in early-onset familial Alzheimer's disease. Nature 1995;375(6534):754-760.

34. Levy-Lahad E, Wasco W, Poorkaj P, Romano DM, Oshima J, Pettingell WH, Yu CE, Jondro PD, Schmidt SD, Wang K, et al. Candidate gene for the chromosome 1 familial Alzheimer's disease locus. Science 1995;269(5226):973-977.
35. Kumar-Singh S, Theuns J, Van Broeck B, Pirici D, Vennekens K, Corsmit E, Cruts M, Dermaut B, Wang R, Van Broeckhoven C. Mean age-of-onset of familial alzheimer disease caused by presenilin mutations correlates with both increased Abeta42 and decreased Abeta40. Hum Mutat 2006;27(7):686-695.
36. Findeis MA. The role of amyloid beta peptide 42 in Alzheimer's disease. Pharmacology & therapeutics 2007;116(2):266-286.
37. Schmechel DE, Saunders AM, Strittmatter WJ, Crain BJ, Hulette CM, Joo SH, Pericak-Vance MA, Goldgaber D, Roses AD. Increased amyloid beta-peptide deposition in cerebral cortex as a consequence of apolipoprotein E genotype in late-onset Alzheimer disease. Proc Natl Acad Sci U S A 1993;90(20):9649-9653.
38. Strittmatter WJ, Saunders AM, Schmechel D, Pericak-Vance M, Enghild J, Salvesen GS, Roses AD. Apolipoprotein E: high-avidity binding to beta-amyloid and increased frequency of type 4 allele in late-onset familial Alzheimer disease. Proc Natl Acad Sci U S A 1993;90(5):1977-1981.
39. Tanzi RE. A Brief History of Alzheimer's Disease Gene Discovery. J Alzheimers Dis 2012.
40. Honjo K, Black SE, Verhoeff NP. Alzheimer's disease, cerebrovascular disease, and the beta-amyloid cascade. The Canadian journal of neurological sciences Le journal canadien des sciences neurologiques 2012;39(6):712-728.
41. Thal DR, Ghebremedhin E, Orantes M, Wiestler OD. Vascular pathology in Alzheimer disease: correlation of cerebral amyloid angiopathy and arteriosclerosis/lipohyalinosis with cognitive decline. J Neuropathol Exp Neurol 2003;62(12):1287-1301.
42. Yamada M. Cerebral amyloid angiopathy: an overview. Neuropathology 2000;20(1):8-22.
43. Kumar S, O'Donnell ME, Khan K, Dunne G, Carey PD, Lee J. Successful treatment of perineal necrotising fasciitis and associated pubic bone osteomyelitis with the vacuum assisted closure system. World J Surg Oncol 2008;6:67.

44. Ellis RJ, Olichney JM, Thal LJ, Mirra SS, Morris JC, Beekly D, Heyman A. Cerebral amyloid angiopathy in the brains of patients with Alzheimer's disease: the CERAD experience, Part XV. Neurology 1996;46(6):1592-1596.
45. Pfeifer LA, White LR, Ross GW, Petrovitch H, Launer LJ. Cerebral amyloid angiopathy and cognitive function: the HAAS autopsy study. Neurology 2002;58(11):1629-1634.
46. Yamada M. Risk factors for cerebral amyloid angiopathy in the elderly. Ann N Y Acad Sci 2002;977:37-44.
47. Winkler DT, Bondolfi L, Herzig MC, Jann L, Calhoun ME, Wiederhold KH, Tolnay M, Staufenbiel M, Jucker M. Spontaneous hemorrhagic stroke in a mouse model of cerebral amyloid angiopathy. J Neurosci 2001;21(5):1619-1627.
48. Serrano-Pozo A, Frosch MP, Masliah E, Hyman BT. Neuropathological alterations in Alzheimer disease. Cold Spring Harbor perspectives in medicine 2011;1(1):a006189.
49. Weller RO, Preston SD, Subash M, Carare RO. Cerebral amyloid angiopathy in the aetiology and immunotherapy of Alzheimer disease. Alzheimer's research & therapy 2009;1(2):6.
50. Thal DR, Papassotiropoulos A, Saido TC, Griffin WS, Mrak RE, Kolsch H, Del Tredici K, Attems J, Ghebremedhin E. Capillary cerebral amyloid angiopathy identifies a distinct APOE epsilon4-associated subtype of sporadic Alzheimer's disease. Acta Neuropathol 2010;120(2):169-183.
51. Sjobeck M, Englund E. Glial levels determine severity of white matter disease in Alzheimer's disease: a neuropathological study of glial changes. Neuropathol Appl Neurobiol 2003;29(2):159-169.
52. Brun A, Englund E. A white matter disorder in dementia of the Alzheimer type: a pathoanatomical study. Ann Neurol 1986;19(3):253-262.
53. Gouw AA, Seewann A, Vrenken H, van der Flier WM, Rozemuller JM, Barkhof F, Scheltens P, Geurts JJ. Heterogeneity of white matter hyperintensities in Alzheimer's disease: post-mortem quantitative MRI and neuropathology. Brain 2008;131(Pt 12):3286-3298.
54. Sjobeck M, Haglund M, Englund E. Decreasing myelin density reflected increasing white matter pathology in Alzheimer's disease--a neuropathological study. Int J Geriatr Psychiatry 2005;20(10):919-926.

55. Englund E, Brun A, Alling C. White matter changes in dementia of Alzheimer's type. Biochemical and neuropathological correlates. Brain 1988;111 (Pt 6):1425-1439.
56. Englund E, Brun A, Persson B. Correlations between histopathologic white matter changes and proton MR relaxation times in dementia. Alzheimer Dis Assoc Disord 1987;1(3):156-170.
57. Roher AE, Weiss N, Kokjohn TA, Kuo YM, Kalback W, Anthony J, Watson D, Luehrs DC, Sue L, Walker D, Emmerling M, Goux W, Beach T. Increased A beta peptides and reduced cholesterol and myelin proteins characterize white matter degeneration in Alzheimer's disease. Biochemistry 2002;41(37):11080-11090.
58. de Groot JC, de Leeuw FE, Oudkerk M, van Gijn J, Hofman A, Jolles J, Breteler MM. Cerebral white matter lesions and cognitive function: the Rotterdam Scan Study. Ann Neurol 2000;47(2):145-151.
59. Preti MG, Baglio F, Lagana MM, Griffanti L, Nemni R, Clerici M, Bozzali M, Baselli G. Assessing corpus callosum changes in Alzheimer's disease: comparison between tract-based spatial statistics and atlas-based tractography. PLoS One 2012;7(4):e35856.
60. Hinkley LB, Marco EJ, Findlay AM, Honma S, Jeremy RJ, Strominger Z, Bukshpun P, Wakahiro M, Brown WS, Paul LK, Barkovich AJ, Mukherjee P, Nagarajan SS, Sherr EH. The role of corpus callosum development in functional connectivity and cognitive processing. PLoS One 2012;7(8):e39804.
61. Teipel SJ, Wegrzyn M, Meindl T, Frisoni G, Bokde AL, Fellgiebel A, Filippi M, Hampel H, Kloppel S, Hauenstein K, Ewers M, group Es. Anatomical MRI and DTI in the diagnosis of Alzheimer's disease: a European multicenter study. J Alzheimers Dis 2012;31 Suppl 3:S33-47.
62. Di Paola M, Spalletta G, Caltagirone C. In vivo structural neuroanatomy of corpus callosum in Alzheimer's disease and mild cognitive impairment using different MRI techniques: a review. J Alzheimers Dis 2010;20(1):67-95.
63. Muskulus M, Scheenstra AEH, Braakman N, Dijkstra J, Verduyn-Lunel S, Alia A, de Groot HJM, Reiber JHC. Prospects for Early Detection of Alzheimer's Disease from Serial MR Images in Transgenic Mouse Models. Curr Alzheimer Res 2009;6(6):503-518.

64. Philipson O, Lord A, Gumucio A, O'Callaghan P, Lannfelt L, Nilsson LN. Animal models of amyloid-beta-related pathologies in Alzheimer's disease. The FEBS journal 2010;277(6):1389-1409.

65. Hsiao K, Chapman P, Nilsen S, Eckman C, Harigaya Y, Younkin S, Yang F, Cole G. Correlative memory deficits, Abeta elevation, and amyloid plaques in transgenic mice. Science 1996;274(5284):99-102.

66. Sturchler-Pierrat C, Abramowski D, Duke M, Wiederhold KH, Mistl C, Rothacher S, Ledermann B, Burki K, Frey P, Paganetti PA, Waridel C, Calhoun ME, Jucker M, Probst A, Staufenbiel M, Sommer B. Two amyloid precursor protein transgenic mouse models with Alzheimer disease-like pathology. Proc Natl Acad Sci U S A 1997;94(24):13287-13292.

67. Chapman PF, White GL, Jones MW, Cooper-Blacketer D, Marshall VJ, Irizarry M, Younkin L, Good MA, Bliss TV, Hyman BT, Younkin SG, Hsiao KK. Impaired synaptic plasticity and learning in aged amyloid precursor protein transgenic mice. Nature neuroscience 1999;2(3):271-276.

68. Kawarabayashi T, Younkin LH, Saido TC, Shoji M, Ashe KH, Younkin SG. Age-dependent changes in brain, CSF, and plasma amyloid (beta) protein in the Tg2576 transgenic mouse model of Alzheimer's disease. J Neurosci 2001;21(2):372-381.

69. Irizarry MC, McNamara M, Fedorchak K, Hsiao K, Hyman BT. APPSw transgenic mice develop age-related A beta deposits and neuropil abnormalities, but no neuronal loss in CA1. J Neuropathol Exp Neurol 1997;56(9):965-973.

70. Herzig MC, Van Nostrand WE, Jucker M. Mechanism of cerebral beta-amyloid angiopathy: murine and cellular models. Brain Pathol 2006;16(1):40-54.

71. Sun SW, Song SK, Harms MP, Lin SJ, Holtzman DM, Merchant KM, Kotyk JJ. Detection of age-dependent brain injury in a mouse model of brain amyloidosis associated with Alzheimer's disease using magnetic resonance diffusion tensor imaging. Experimental neurology 2005;191(1):77-85.

72. Chishti MA, Yang DS, Janus C, Phinney AL, Horne P, Pearson J, Strome R, Zuker N, Loukides J, French J, Turner S, Lozza G, Grilli M, Kunicki S, Morissette C, Paquette J, Gervais F, Bergeron C, Fraser PE, Carlson GA, George-Hyslop PS, Westaway D. Early-onset amyloid deposition and cognitive deficits in transgenic mice expressing a double mutant form of amyloid precursor protein 695. J Biol Chem 2001;276(24):21562-21570.

73. Radde R, Bolmont T, Kaeser SA, Coomaraswamy J, Lindau D, Stoltze L, Calhoun ME, Jaggi F, Wolburg H, Gengler S, Haass C, Ghetti B, Czech C, Holscher C, Mathews PM, Jucker M. Abeta42-driven cerebral amyloidosis in transgenic mice reveals early and robust pathology. EMBO reports 2006;7(9):940-946.
74. Oddo S, Caccamo A, Shepherd JD, Murphy MP, Golde TE, Kayed R, Metherate R, Mattson MP, Akbari Y, LaFerla FM. Triple-transgenic model of Alzheimer's disease with plaques and tangles: intracellular Abeta and synaptic dysfunction. Neuron 2003;39(3):409-421.
75. Oddo S, Caccamo A, Kitazawa M, Tseng BP, LaFerla FM. Amyloid deposition precedes tangle formation in a triple transgenic model of Alzheimer's disease. Neurobiol Aging 2003;24(8):1063-1070.
76. Oakley H, Cole SL, Logan S, Maus E, Shao P, Craft J, Guillozet-Bongaarts A, Ohno M, Disterhoft J, Van Eldik L, Berry R, Vassar R. Intraneuronal beta-amyloid aggregates, neurodegeneration, and neuron loss in transgenic mice with five familial Alzheimer's disease mutations: potential factors in amyloid plaque formation. J Neurosci 2006;26(40):10129-10140.
77. Plewes DB, Kucharczyk W. Physics of MRI: a primer. J Magn Reson Imaging 2012;35(5):1038-1054.
78. Purcell EM, Torrey HC, Pound RV. Resonance Absorption by Nuclear Magnetic Moments in a Solid. Phys Rev 1946;69(1-2):37-38.
79. Bloch F. Nuclear Induction. Phys Rev 1946;70(7-8):460-474.
80. Armstrong P, Keevil SF. Magnetic resonance imaging--1: Basic principles of image production. BMJ 1991;303(6793):35-40.
81. Markl M, Leupold J. Gradient echo imaging. J Magn Reson Imaging 2012;35(6):1274-1289.
82. Jung BA, Weigel M. Spin echo magnetic resonance imaging. J Magn Reson Imaging 2013;37(4):805-817.
83. Hennig J, Nauerth A, Friedburg H. RARE imaging: a fast imaging method for clinical MR. Magn Reson Med 1986;3(6):823-833.
84. Hennig J, Friedburg H. Clinical applications and methodological developments of the RARE technique. Magnetic Resonance Imaging 1988;6(4):391-395.
85. Nishimura DG. Time-of-flight MR angiography. Magn Reson Med 1990;14(2):194-201.

86. Suryan G. Nuclear resonance in flowing liquids. Proceedings Mathematical Sciences 1951;33(2):107-111.
87. Graves MJ. Magnetic resonance angiography. Br J Radiol 1997;70:6-28.
88. Du YP, Parker DL, Davis WL, Cao G, Buswell HR, Goodrich KC. Experimental and theoretical studies of vessel contrast-to-noise ratio in intracranial time-of-flight MR angiography. J Magn Reson Imaging 1996;6(1):99-108.
89. Blatter DD, Parker DL, Robison RO. Cerebral MR angiography with multiple overlapping thin slab acquisition. Part I. Quantitative analysis of vessel visibility. Radiology 1991;179(3):805-811.
90. Beckmann N. High resolution magnetic resonance angiography non-invasively reveals mouse strain differences in the cerebrovascular anatomy in vivo. Magn Reson Med 2000;44(2):252-258.
91. Howles GP, Ghaghada KB, Qi Y, Mukundan S, Jr., Johnson GA. High-resolution magnetic resonance angiography in the mouse using a nanoparticle blood-pool contrast agent. Magn Reson Med 2009;62(6):1447-1456.
92. Laub G. Displays for MR angiography. Magn Reson Med 1990;14(2):222-229.
93. Kroeker RM, McVeigh ER, Hardy P, Bronskill MJ, Henkelman RM. In vivo measurements of NMR relaxation times. Magn Reson Med 1985;2(1):1-13.
94. Bothwell JH, Griffin JL. An introduction to biological nuclear magnetic resonance spectroscopy. Biological reviews of the Cambridge Philosophical Society 2011;86(2):493-510.
95. Kantarci K, Jack CR, Jr. Neuroimaging in Alzheimer disease: an evidence-based review. Neuroimaging Clin N Am 2003;13(2):197-209.
96. de Leon MJ, George AE, Stylopoulos LA, Smith G, Miller DC. Early marker for Alzheimer's disease: the atrophic hippocampus. Lancet 1989;2(8664):672-673.
97. Migliaccio R, Agosta F, Possin KL, Rabinovici GD, Miller BL, Gorno-Tempini ML. White matter atrophy in Alzheimer's disease variants. Alzheimer's & dementia : the journal of the Alzheimer's Association 2012;8(5 Suppl):S78-87 e71-72.
98. Wadghiri YZ, Hoang DM, Wisniewski T, Sigurdsson EM. In vivo magnetic resonance imaging of amyloid-beta plaques in mice. Methods Mol Biol 2012;849:435-451.
99. Jack CR, Jr., Garwood M, Wengenack TM, Borowski B, Curran GL, Lin J, Adriany G, Grohn OH, Grimm R, Poduslo JF. In vivo visualization of

Alzheimer's amyloid plaques by magnetic resonance imaging in transgenic mice without a contrast agent. Magn Reson Med 2004;52(6):1263-1271.

100. Nakada T, Matsuzawa H, Igarashi H, Fujii Y, Kwee IL. In vivo visualization of senile-plaque-like pathology in Alzheimer's disease patients by MR microscopy on a 7T system. Journal of neuroimaging : official journal of the American Society of Neuroimaging 2008;18(2):125-129.
101. Braakman N, Matysik J, van Duinen SG, Verbeek F, Schliebs R, de Groot HJ, Alia A. Longitudinal assessment of Alzheimer's beta-amyloid plaque development in transgenic mice monitored by in vivo magnetic resonance microimaging. J Magn Reson Imaging 2006;24(3):530-536.
102. Vanhoutte G, Dewachter I, Borghgraef P, Van Leuven F, Van der Linden A. Noninvasive in vivo MRI detection of neuritic plaques associated with iron in APP[V717I] transgenic mice, a model for Alzheimer's disease. Magnetic resonance in medicine : official journal of the Society of Magnetic Resonance in Medicine / Society of Magnetic Resonance in Medicine 2005;53(3):607-613.
103. Lee SP, Falangola MF, Nixon RA, Duff K, Helpern JA. Visualization of beta-amyloid plaques in a transgenic mouse model of Alzheimer's disease using MR microscopy without contrast reagents. Magn Reson Med 2004;52(3):538-544.
104. Whittall KP, MacKay AL, Li DK, Vavasour IM, Jones CK, Paty DW. Normal-appearing white matter in multiple sclerosis has heterogeneous, diffusely prolonged T(2). Magn Reson Med 2002;47(2):403-408.
105. House MJ, St Pierre TG, Foster JK, Martins RN, Clarnette R. Quantitative MR imaging R2 relaxometry in elderly participants reporting memory loss. AJNR Am J Neuroradiol 2006;27(2):430-439.
106. Sheline YI, Raichle ME. Resting State Functional Connectivity in Preclinical Alzheimer's Disease. Biol Psychiatry 2013.
107. Kantarci K. 1H Magnetic resonance spectroscopy in dementia. Br J Radiol 2007;80(Special_Issue_2):S146-152.
108. Kantarci K, Petersen R, Boeve B, Knopman D, Tang-Wai D, O'Brien P, Weigand S, Edland S, Smith G, Ivnik R. 1H MR spectroscopy in common dementias. Neurology 2004;63(8):1393 - 1398.
109. Beckmann N, Schuler A, Mueggler T, Meyer EP, Wiederhold KH, Staufenbiel M, Krucker T. Age-dependent cerebrovascular abnormalities and blood flow

disturbances in APP23 mice modeling Alzheimer's disease. J Neurosci 2003;23(24):8453-8459.

110. Ishibashi K, Tanaka K, Nakabayashi T, Nakamura M, Uchiyama M, Okawa M. Latent cerebral artery stenoses on magnetic resonance angiography in a patient diagnosed as probable Alzheimer disease. Psychiatry and clinical neurosciences 1998;52(1):93-96.

111. Pimentel-Coelho PM, Rivest S. The early contribution of cerebrovascular factors to the pathogenesis of Alzheimer's disease. Eur J Neurosci 2012;35(12):1917-1937.

112. El Tannir El Tayara NT, Delatour B, Volk A, Dhenain M. Detection of vascular alterations by in vivo magnetic resonance angiography and histology in APP/PS1 mouse model of Alzheimer's disease. MAGMA 2010;23(1):53-64.

113. Thal DR, Capetillo-Zarate E, Larionov S, Staufenbiel M, Zurbruegg S, Beckmann N. Capillary cerebral amyloid angiopathy is associated with vessel occlusion and cerebral blood flow disturbances. Neurobiol Aging 2009;30(12):1936-1948.

114. De Silva DA, Ancalan M, Doshi K, Chang HM, Wong MC, Chen C. Intracranial large artery disease in Alzheimer's disease and vascular dementia among ethnic Asians. Eur J Neurol 2009;16(5):643-645.

115. Bullitt E, Zeng D, Mortamet B, Ghosh A, Aylward SR, Lin W, Marks BL, Smith K. The effects of healthy aging on intracerebral blood vessels visualized by magnetic resonance angiography. Neurobiol Aging 2010;31(2):290-300.

116. Damadian R. Tumor detection by nuclear magnetic resonance. Science 1971;171(976):1151-1153.

117. Kirsch SJ, Jacobs RW, Butcher LL, Beatty J. Prolongation of magnetic resonance T2 time in hippocampus of human patients marks the presence and severity of Alzheimer's disease. Neurosci Lett 1992;134(2):187-190.

118. Wang H, Yuan H, Shu L, Xie J, Zhang D. Prolongation of T(2) relaxation times of hippocampus and amygdala in Alzheimer's disease. Neurosci Lett 2004;363(2):150-153.

119. Campeau NG, Petersen RC, Felmlee JP, O'Brien PC, Jack CR, Jr. Hippocampal transverse relaxation times in patients with Alzheimer disease. Radiology 1997;205(1):197-201.

120. Laakso MP, Partanen K, Soininen H, Lehtovirta M, Hallikainen M, Hanninen T, Helkala EL, Vainio P, Riekkinen PJ, Sr. MR T2 relaxometry in Alzheimer's

disease and age-associated memory impairment. Neurobiol Aging 1996;17(4):535-540.

121. Huesgen CT, Burger PC, Crain BJ, Johnson GA. In vitro MR microscopy of the hippocampus in Alzheimer's disease. Neurology 1993;43(1):145-152.
122. Kumar R, Delshad S, Macey PM, Woo MA, Harper RM. Development of T2-relaxation values in regional brain sites during adolescence. Magn Reson Imaging 2010;29(2):185-193.
123. Kumar R, Delshad S, Woo MA, Macey PM, Harper RM. Age-related regional brain T2-relaxation changes in healthy adults. J Magn Reson Imaging 2012;35(2):300-308.
124. Guilfoyle DN, Dyakin VV, O'Shea J, Pell GS, Helpern JA. Quantitative measurements of proton spin-lattice (T1) and spin-spin (T2) relaxation times in the mouse brain at 7.0 T. Magn Reson Med 2003;49(3):576-580.
125. Helpern JA, Lee SP, Falangola MF, Dyakin VV, Bogart A, Ardekani B, Duff K, Branch C, Wisniewski T, de Leon MJ, Wolf O, O'Shea J, Nixon RA. MRI assessment of neuropathology in a transgenic mouse model of Alzheimer's disease. Magn Reson Med 2004;51(4):794-798.
126. Braakman HM, van de Molengraft FJ, Hubert WW, Boerman DH. Lethal African trypanosomiasis in a traveler: MRI and neuropathology. Neurology 2006;66(7):1094-1096.
127. El Tannir El Tayara N, Delatour B, Le Cudennec C, Guegan M, Volk A, Dhenain M. Age-related evolution of amyloid burden, iron load, and MR relaxation times in a transgenic mouse model of Alzheimer's disease. Neurobiol Dis 2006;22(1):199-208.
128. Borthakur A, Gur T, Wheaton AJ, Corbo M, Trojanowski JQ, Lee VM, Reddy R. In vivo measurement of plaque burden in a mouse model of Alzheimer's disease. J Magn Reson Imaging 2006;24(5):1011-1017.
129. El Tannir El Tayara NT, Volk A, Dhenain M, Delatour B. Transverse relaxation time reflects brain amyloidosis in young APP/PS1 transgenic mice. Magn Reson Med 2007;58(1):179-184.
130. Falangola MF, Dyakin VV, Lee SP, Bogart A, Babb JS, Duff K, Nixon R, Helpern JA. Quantitative MRI reveals aging-associated T2 changes in mouse models of Alzheimer's disease. NMR Biomed 2007;20(3):343-351.

131. Weidensteiner C, Metzger F, Bruns A, Bohrmann B, Kuennecke B, von Kienlin M. Cortical hypoperfusion in the B6.PS2APP mouse model for Alzheimer's disease: comprehensive phenotyping of vascular and tissular parameters by MRI. Magn Reson Med 2009;62(1):35-45.

132. Teipel SJ, Kaza E, Hadlich S, Bauer A, Bruning T, Plath AS, Krohn M, Scheffler K, Walker LC, Lotze M, Pahnke J. Automated detection of amyloid-beta-related cortical and subcortical signal changes in a transgenic model of Alzheimer's disease using high-field MRI. J Alzheimers Dis 2011;23(2):221-237.

133. Bartzokis G, Cummings JL, Sultzer D, Henderson VW, Nuechterlein KH, Mintz J. White matter structural integrity in healthy aging adults and patients with Alzheimer disease: a magnetic resonance imaging study. Arch Neurol 2003;60(3):393-398.

134. Bartzokis G, Sultzer D, Lu PH, Nuechterlein KH, Mintz J, Cummings JL. Heterogeneous age-related breakdown of white matter structural integrity: implications for cortical "disconnection" in aging and Alzheimer's disease. Neurobiol Aging 2004;25(7):843-851.

135. Gold BT, Johnson NF, Powell DK, Smith CD. White matter integrity and vulnerability to Alzheimer's disease: preliminary findings and future directions. Biochim Biophys Acta 2012;1822(3):416-422.

136. Gold BT, Powell DK, Andersen AH, Smith CD. Alterations in multiple measures of white matter integrity in normal women at high risk for Alzheimer's disease. Neuroimage 2010;52(4):1487-1494.

137. Hu X, Norris DG. Advances in high-field magnetic resonance imaging. Annu Rev Biomed Eng 2004;6:157-184.

138. Fushimi Y, Miki Y, Kikuta K, Okada T, Kanagaki M, Yamamoto A, Nozaki K, Hashimoto N, Hanakawa T, Fukuyama H, Togashi K. Comparison of 3.0- and 1.5-T three-dimensional time-of-flight MR angiography in moyamoya disease: preliminary experience. Radiology 2006;239(1):232-237.

139. van de Ven RC, Hogers B, van den Maagdenberg AM, de Groot HJ, Ferrari MD, Frants RR, Poelmann RE, van der Weerd L, Kiihne SR. T(1) relaxation in in vivo mouse brain at ultra-high field. Magn Reson Med 2007;58(2):390-395.

2 Monitoring blood flow alterations in the Tg2576 mouse model of Alzheimer's disease*

2.1 Abstract

Many neurodegenerative diseases including Alzheimer's disease are linked to abnormalities in the vascular system. In AD, the deposition of Aβ peptide in the cerebral vessel walls, known as cerebral amyloid angiopathy is frequently observed, leading to blood flow abnormalities. Visualization of the changes in vascular structure is important for early diagnosis and treatment. Blood vessels can be imaged non-invasively by MRA. In this study we optimized high resolution MRA at 17.6 T to longitudinally monitor morphological changes in cerebral arteries in a Tg2576 mouse model, a widely used model of AD. Our results at 17.6 T show that MRA significantly benefits from the ultra-high magnetic field strength especially to visualize smaller vessels. Visual and quantitative analysis of MRA results revealed severe blood flow defects in large and medium sized arteries in Tg2576 mice. In particular blood flow defects were observed in the middle cerebral artery and in the anterior communicating artery in Tg2576 mice. Histological data show that Aβ levels in the vessel wall may be responsible for impaired cerebral blood flow, thereby contributing to the early progression of AD. To our knowledge this is the first ultra-high field MRA study monitoring blood flow alterations longitudinally in living Tg2576 mice, consequently providing a powerful tool to test new therapeutic intervention related to CAA in a mouse model of AD.

2.2 Introduction

Alzheimer's disease is the most common form of dementia with no effective treatment or definitive ante mortem diagnostic test. The neuropathologic features of AD include the occurrence of Aβ-containing plaques, neurofibrillary tangles, decreased synaptic density, and loss of neurons (1,2). In addition, cerebrovascular abnormalities coexist with these pathological features of AD. In particular, the deposition of amyloid in the cerebral vessel walls, known as cerebral amyloid angiopathy, is frequently observed, leading to blood flow abnormalities in AD (3,4). Small to medium-sized arteries and arterioles are the

*This chapter was published in NeuroImage 2012, 60(2);958-966

most frequently affected vessels by CAA in AD (5-7). Though CAA is very common in the advanced stages of AD, its contribution to the onset and progression of AD is unknown.

The evidence for blood flow disturbance in AD comes mainly from postmortem studies (8,9). Yamada (2002) has reported that among AD patients (n = 82), the frequency of CAA was 87%, whereas the frequency of CAA in elderly non-AD (n = 119) patients was only 35%. CAA of Aβ type, defined by the accumulation of β-amyloid peptide (Aβ) in cerebral vessels, is the most common form of CAA in elderly population as well as patients with AD (10). Currently *in vivo* diagnosis of CAA relies on detecting indirect symptoms such as hemorrhage, microbleeding and abnormal vascular reactivity (4,11). Although positron emission tomography in combination with Pittsburg compound, has been shown to detect CAA in AD patients (4), the need to use ionizing radiation for PET and unspecificity of Pittsburg compound for distinguishing between parenchymal and vascular Aβ plaques impede the use of this method on a large scale.

Transgenic mouse models of AD have been used to understand how CAA related blood flow abnormalities contribute to the onset and progression of AD (12-18). *Ex vivo* studies in human and in transgenic mouse models have reported similar observations regarding CAA related morphological changes in vascular structures leading to blood flow defects in AD. Recently, an upregulation of the angiogenic vascular endothelial growth factor by cortical vascular endothelial cells in 21-month-old transgenic Tg2576 mice has been observed suggesting a role of vascular endothelial growth factor in formation of vascular Aβ and mediating CAA (19,20). However, direct *in vivo* methods to probe blood flow disturbance during AD in mice are highly challenging. *In vivo* MR techniques currently used for AD evaluations in humans and mouse models of AD are in a state of progression with continued reassessment for enhanced diagnostic accuracy (21,22). Non-invasive MR imaging techniques, such as *in vivo* MRA, have shown great potential to study blood flow defects in APP23 and APP/PS1 mouse models of AD (23-25). In this technique shortening of the effective T_1 of moving blood provides the vessel contrast with stationary tissue (26). While the global architecture of the cerebral vasculature could be detected in both APP23 and APP/PS1 mice by *in vivo* MRA at 4.7 T magnetic field strength, further improvement in visualization is desirable, especially for detection of small arteries with low blood flow rate. The small size of the mouse brain has considerable limitations for MRA in visualizing cerebral vasculature with high spatial resolution and signal-to-noise ratio at low magnetic field strength (≥4.7 T). The T_1

relaxation time of tissue increases with the field strength (27). Increased T_1 relaxation time and high magnetization at higher fields provides improved signal-to-noise ratio and higher vessel-to-tissue contrast that may contribute to the improved quality of MRA (28). Therefore, moving to high (such as 9.4 T) or ultra-high (such as 17.6 T) magnetic field can significantly improve visualization of cerebral vasculature and blood flow abnormalities in mouse models of AD as well as for other neurodegenerative diseases. Tg2576 is one of the most widely used transgenic mouse models of AD (29). In this model accumulation of Aβ in cerebral vessels starts between 9-12 months of age and severity of CAA increases during aging (30-34). Reports on MRA for this mouse model are lacking. In addition, the *in vivo* relationship between amyloid plaque deposition in brain tissue and its correlation with blood flow alterations is not clear.

The aim of this study was to: (1) achieve improved visualization of cerebral vasculature by optimizing and applying *in vivo* MRA at 17.6 T magnetic field strength; (2) detect AD related blood flow defects in cerebral arties in Tg2576 mice; and (3) longitudinally follow, *in vivo* amyloid plaque deposition in brain tissue and its correlation with CAA related morphological changes in cerebral arteries and blood flow alterations in the same Tg2576 mice with age.

2.3 Materials and Methods

2.3.1 Mice

In this study transgenic Tg2576 mice developed and described by Hsiao *et al*. (1996) were used as model of AD. The mice contained as transgene the human amyloid precursor protein (APP695) with the Swedish double mutation (K670N, M671L) under control of a hamster prion protein promoter (29). Three founder mice were kindly provided by Dr Karen Hsiao Ashe (University of Minnesota) and used for further breeding. Mice heterozygous for the transgene and wild-type littermates were on a C57BL/6 x SJL background. At the age of four weeks transgeneity was identified by polymerase chain reaction of tail DNA as described elsewhere (29). The N2 generation mice of both genders were studied at the ages of 12–18 months. Age-matched non-transgenic littermates served as controls. In addition, C57BL/6 mice (9 months old) were used for optimization studies. All of the animal experiments were approved by the institutional animal care and animal use committee of the University of Leiden in accordance with the NIH Guide for the Care and Use of Laboratory Animals.

2.3.2 Histology

Histological analyses were performed to assess amyloid deposits and CAA in Tg2576 mice by following the procedure as described previously (21). The mice were decapitated and brains were fixed in 4% buffered paraformaldehyde (Zinc Formal-Fixx, ThermoShandon, UK) for 48 h. Following fixation brains were dehydrated and embedded in paraffin. Subsequently coronal sections (5 μm thick) were carefully cut using a vibratome while maintaining as much as possible the same spatial orientation of the mouse brain as in the μMRI experiments. To detect Aβ, brain sections were subjected to immunohistochemistry using anti-Aβ (6E10), anti-Aβ40 (BC40) or anti-Aβ42 (BC42). Immunolabeling was visualized by using the ABC kit (Vectastain) according to the manufacturer's instructions.

2.3.3 μMRI

All measurements were conducted on a vertical wide bore 9.4 T or 17.6 T Bruker spectrometer with a 1000 mTm^{-1} actively shielded imaging gradient insert (Bruker Biospin GmbH, Germany). A birdcage RF coil (inner diameter 2 cm) was used. The system was interfaced to a Linux PC running XWinNMR 3.2 and Paravision 5.0 (Bruker Biospin GmbH, Germany) software.

All *in vivo* MR imaging studies were conducted as previously described (21). Before MR imaging, the mice were anesthetized with 2% isoflurane (Forene, Abott, UK), in air (0.3 l/min) and oxygen (0.3 l/min). During scanning the isoflurane concentration was maintained between 1 and 1.5% to keep the breathing of the animal at a constant rate of ~50 breaths per minute. Animals were placed in a birdcage RF coil with a special mouse head mask, which was used to administer the anesthetic gas during MR experiments. A respiration sensor, connected to a respiration unit, was placed on the abdomen of the mouse, to monitor it's respiration rate during the MR imaging. The respiration unit was connected to a computer having Bio-SAM respiration monitoring software (Bruker Biospin, Germany). The body temperature of the mouse was kept constant by pumping warm water through the gradient system. The rectal body temperature of the mouse during scanning was measured to be 35±1°C.

T_2-weighted MR images were acquired with a multislice RARE (35) sequence at 9.4 T. Coronal images were obtained with a slice thickness of 0.5 mm. A resolution of 78x78 μm was achieved within an acquisition time of ~25 min. The imaging parameters used for the RARE sequence were: TE = 11.6 ms (effective TE = 23.33 ms); TR = 6 s; FA = 90°,

averages = 4, RARE factor (echo train length) = 4; FOV = 2.00 × 2.00 cm^2 and image matrix = 256 × 256. Quantification of Aβ plaque load in MR images was done as described earlier (21).

2.3.4 MRA

TOF angiograms were obtained using a 3D gradient-echo sequence. To find the optimum combination of parameters for TOF-MRA at 17.6 T, variable flip angle (FA) and TR parameters of the 3D TOF gradient echo sequence were systematically varied to obtain the best image quality in a reasonable imaging time. The following parameters were used: TE = 1.86 ms; FOV = 15 X 15 X 15 mm; matrix size= 128 X 128 X 128; FA = 10°, 15°, 20°, 30°, 40° or 50°; TR = 15, 20, 30, or 40 ms.

Optimized scan parameters used to acquire high-resolution 3D-MRA of transgenic mice and non-transgenic littermates were as follows: TE = 1.86 ms; FOV = 17 X 17 X 17 mm; matrix size = 256 X 192 X 192; FA = 20°; and TR = 20 ms. All data were zero-filled to 256 X 256 X 256.

Three-dimensional TOF MRA was compared at 9.4 T and 17.6 T. All imaging parameters were kept the same at both magnetic fields. Imaging parameters were TE = 1.86 ms; TR = 20 ms; FA = 20°. All data (matrix size 256 X 192 X 192) were zero-filled to 256 X 256 X 256. The total acquisition time of 3D-TOF was ~9 min. Three-dimensional views were obtained by generating MIP using Paravision 5 software (Bruker Biospin, GmbH, Germany).

Identification of cerebral arteries was performed by inspecting the angiograms under various angles and comparing the vessels to the anatomical atlas of Dorr *et al*. (36) and previous reports in the literature (25,37-40).

2.3.5 Image analysis and quantification

The severity of the vascular abnormalities in Tg2576 mice and non-transgenic control mice was evaluated by visual assessment as well as by a semi-quantitative analysis. Visual assessment of MCA was based on the pointing system as described earlier (25) According to this system, blood flow abnormalities were graded on the basis of the number and extent of signal voids detected on the MR angiograms. A flow disturbance was counted when a decrease of the signal was visible on the scan, but the signal intensity at the level of the artery did not yet reach background level. A void was counted

when the signal intensity at the level of the artery reaches the background level. Furthermore a distinction was made between a small void and an extended void. The grades were defined as follows: (1) flow disturbance visible, but the artery shape was unaltered; (2) one or two small signal voids: a small signal void was defined as a void with a maximum length of twice the diameter of the artery; (3) more than 2 small signal voids; (4) one extended signal void: an extended void was defined as a void with a length larger than twice the diameter of the artery; (5) a combination of small and extended voids; and (6) artery was partially or completely missing.

For the semi-quantitative method, the average contrast-to-noise ratio and signal-to-noise ratio were calculated from the coronal slices (n = 5-9) of the MRA data set. Three ROIs were selected in each slice: (1) an ROI manually delineated in the vessel contour on cross-sectional slices; (2) an ROI of the background brain tissue without vessels (BG); and (3) an ROI of the surrounding air. The average standard deviation of the ROI in surrounding air was defined as noise (σ). The CNR of each region was calculated as: CNR = (sROI-sBG)/σ (air). The SNR was calculated as: SNR = sROI/σ (air). "s" refers to average signal intensity within the selected area. Signal intensity of ROI placed on the vessel was calculated above a threshold value corresponding to s(BG)+[0.1x s(BG)].

The means and standard deviations of each region were calculated. The statistical comparisons were made by pooling all slice measurements from all the datasets in a given sample group and performing one-tailed and/or two-tailed Student's t-test. Statistical significance was assigned for P values < 0.05.

2.4 Results and Discussion

2.4.1 Optimization of MRA at 17.6 T

The 3D TOF MRA sequence was optimized at 17.6 T to visualize cerebral arteries in living mouse. To find the optimum combination of parameters for TOF MRA at 17.6 T, radiofrequency pulse TR and pulse FA were steadily varied.

Fig. 2.1 shows the effect of varying FA and TR on CNR of MCA (Fig. 2.1A) and azPA (Fig. 2.1B). As is clear from this figure, MCA, which is one of the large vessels with relatively high blood flow (Dorr *et al*., 2007), has excellent visibility at all combinations

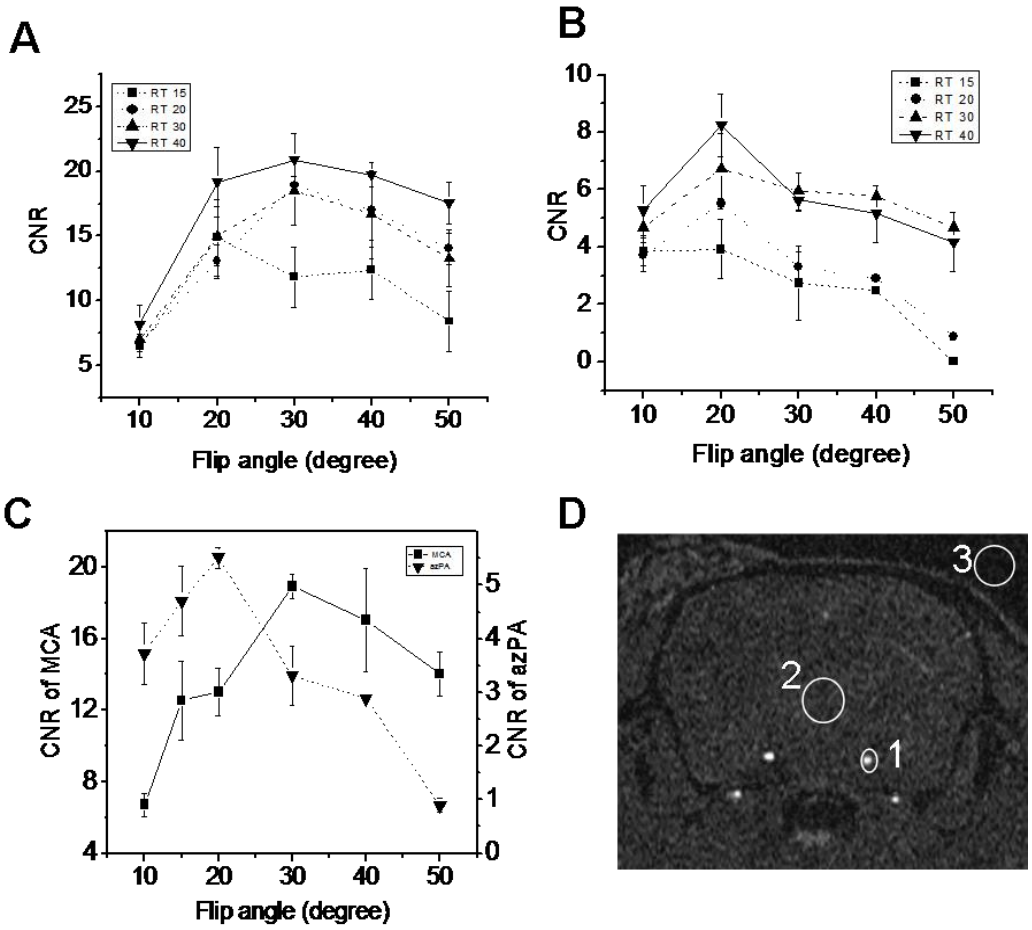

Fig. 2.1. *Optimization of 3D TOF-MRA at 17.6 T magnetic field strength. (A) The effect of varying the radiofrequency pulse flip angle (FA) and inflow time (repetition time, TR) was evaluated on contrast to noise ratio (CNR) of middle cerebral artery (MCA) (A) and azygos pericallosal artery (azPA) (B). The effect of varying the FA on the CNR of MCA and azPA measured at a constant TR of 20 ms (C). Vessels having higher blood flow such as MCA were better visualized at higher FA (30°), however smaller vessels such as azPA having low blood flow were better visualized at smaller FA (15°-20°). (D) Slice of a 3D data set indicating the region of interest for which CNR evaluation was performed (1= vessel; 2= background brain tissue; 3= surrounding air). The optimization was performed on three mice, with nearly identical results. For clarity, the plots are from a single specimen. The values are the mean ± SD (error bars) over five slices.*

of FA (20°-50°) and TR (15-40 ms). However small vessels such as azPA are better delineated at smaller FA (20°). While a longer TR offers greater CNR, the TR of 20 ms had been chosen as optimum to obtain reasonable resolution in a relatively short scan time for subsequent measurements. The relationship between CNR and FA (10°-50°) at constant TR (20 ms) of MCA and azPA is shown in Fig. 2.1C. A representative slice of a

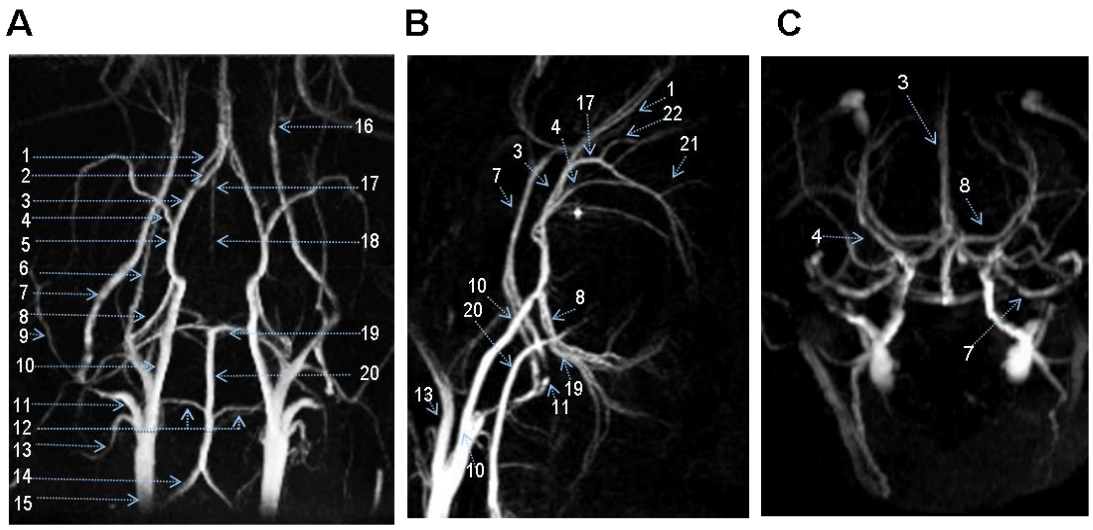

Fig. 2.2. *Coronal (A), sagittal (B) and transverse (C) projection of high-resolution MIPs of a 3D-TOF angiogram of a mouse cerebrovascular system revealing arterial anatomy at 17.6 T magnet field strength. The following arteries were clearly identified: (1) Olfactory artery (OlfA); (2) Anterior communicating artery (AComA); (3) Anterior cerebral artery (ACA); (4) Middle cerebral artery (MCA); (5) & (10) Internal carotid artery (ICA); (6) Facial artery (external Maxillary artery);(7) Palatine portion of pterygopalatine (PPP); (8) Posterior cerebral artery (PCA); (9) Maxillary artery; (11) Pterygo portion of pterygopalatine; (12) Caudal cellebellar artery;(13) A branch of common carotid artery; (14) Vertebral artery (VA); (15) Common carotid artery (CCA); (16) Ophthalmic artery; (17) Anterior azygos cerebral artery (azACA); (18) Azygos pericallosal artery (azPA); (19) Superior cerebellar artery (SCA); (20) Basilar artery (BA); (21) Middle internal frontal artery; (22) Anterior internal frontal artery; and (23) External carotid artery (ECA).*

3D data set of MRA showing the region of interest used for estimation of CNR of vessels with respect to background brain tissue and surrounding air is shown in Fig. 2.1D. Fig. 2.1 depicts a high resolution MRA of a 14-months-old mouse along the coronal (A) and sagittal (B) and transverse (C) directions acquired in 9 min using optimized sequence parameters at 17.6 T. Many small and medium size vessels were nicely delineated at 17.6 T within this short scan time.

2.4.2 Field dependence

Fig. 2.3 compares the angiogram of the vascular system of the same wild-type mouse imaged at 9.4 T (Fig. 2.3A) and 17.6 T (Fig. 2.3B). In general MRA at 17.6 T revealed enhanced visualization of vessels compared to the data collected in a field of 9.4 T, especially for small vessels. For example, branches of azACA are better resolved at 17.6 T as compared to 9.4 T. Figs. 2.3 C and D summarize the effect of field strength on CNR

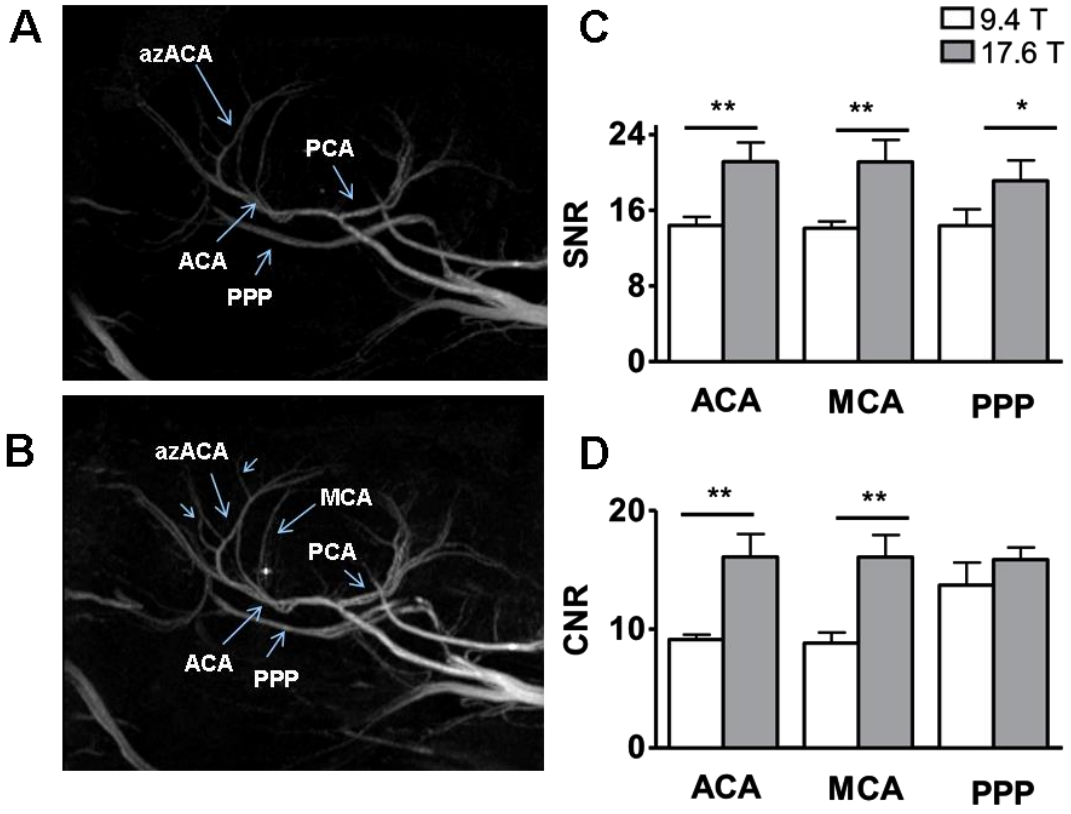

Fig. 2.3. *Angiogram in sagittal view of same 9-month-old wild-type mouse imaged at 9.4 T (A) and 17.6 T (B) magnetic field strengths. Arrows indicate vascular branches, which are better resolved at 17.6 T as compared to 9.4 T. Comparison of SNR (C) and CNR (D) of ACA, MCA and PPP vessels estimated at 9.4 T and 17.6 T. Both CNR and SNR in all three vessels were higher at 17.6 T as compared to 9.4 T. Values are expressed as mean ± SD (error bars). Two-tail student T test, *P <0.05, **P <0.01, n = 3.*

(a) and SNR (b) of vessels including MCA, ACA and PPP. The calculated SNR (Fig. 2.3C) of all three vessels are significantly higher at 17.6 T as compared to 9.4 T. The SNR of MCA, ACA and PPP were ~50%, ~47% and ~33% higher at 17.6 T than at 9.4 T, respectively. MCA and ACA also showed significantly higher CNR (~70-80%) at 17.6 T than at 9.4 T (Fig. 2.3D). The superior contrast at 17.6 T could be attributed to longer T_1 of background tissue as well as greater magnetization of inflowing blood (41). The longer T_1s of tissues provide better background suppression, which allows improved visualization of smaller distal vessels with MRA. The observed increase in SNR was less than expected for the higher field of 17.6T. This could be due to increased susceptibility effects and larger field inhomogeneity at higher magnetic field. Since SNR is inversely proportional to the square root of T_1, longer T_1 at higher field also has an inverse effect on SNR (42). Nevertheless the substantial increase of vessel SNR at 17.6 T is offering the

possibility to either increase the spatial resolution or to shorten scan times for future mouse MRA studies.

2.4.3 Evaluation of vascular alterations in control and Tg2576 mice with age

To evaluate and compare the *in vivo* vascular alterations in control and Tg2576 mice and to follow changes over time, we applied high resolution MRA at 17.6 T. In general blood flow alterations detected on TOF-angiograms were more frequent in Tg2576 mice as compared to control mice. In particular, the overall decrease in the brightness of arteries and alterations such as flow voids and vessel signal loss were more visible in Tg2576 mice as compared to control mice. Fig. 2.4 (A and B) shows representative angiograms of two 18-month-old Tg2576 mice. The numbers on the angiogram indicate the appointed score to the level of severity of alterations. The higher the score, the more severe the alteration was. For example, a flow disturbance without apparent change in vessel shape is visible in AComA (score 1 in Fig. 2.4A); A small signal void was observed at the origin of AComA (score 2 in Fig. 2.4B); More than two small voids in the same artery were observed in MCA on both sides (score 3 in Fig. 2.4B); An extended void can be seen in the small branch of CCA on both sides (score 4 in Fig. 2.4A); A combination of an extended void and several small signal voids was observed in the small branches of carotid artery on both sides (score 5 in Fig. 2.4B). Signal was no longer visible for the pterygo portion of the pterygopalatine artery (score 6 in Figs. 2.4A and B). Fig. 2.4C shows the enlarge view of these alterations.

In general, MCA was one of the most altered vessels in the TOF-angiogram of Tg2576 mice. A comparison of the alteration mean scores in MCA in Tg2576 and control mice with age is shown in Fig. 2.4D. The changes in the MCA alteration score in control and Tg2576 mice were insignificant at the age of 14 and 16 months while became significantly higher (~57%) at the age of 18 months in Tg2576 mice as compared to the control mice (Fig. 2.4D). The abnormalities in MCA in Tg2576 mice, detected by MRA in this study, are consistent with *in vivo* cerebral blood flow alterations observed in MCA in human AD patients (43,44). In these patients, stenosis and cerebral hypoperfusion have been reported in the MCA. Fig. 2.5 (A and B) compares 3D angiogram and its source-slice data set of control and a Tg2576 mouse. Severe decrease of signal intensity can be seen in the AComA in addition to MCA in Tg2576 mouse, but not in control mice.

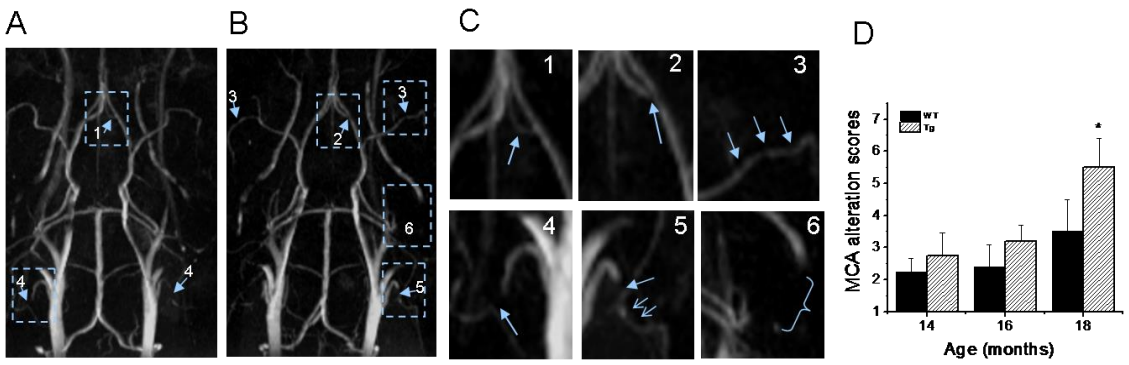

Fig. 2.4. (A, B) *Angiograms collected in the 17.6 T magnet, of 18-month-old transgenic mice showing various level of severities of morphological changes appointed in 3D MIP. The number indicates the appointed score to the level of severity of alterations. For example: 1= a flow disturbance (as seen in AComA in image* ***A****); 2= a small signal void (as observed at the origin of AComA in image* ***B****); 3= more than two small voids in the same artery (as observed on the MCA on both sides in image* ***B****); 4= an extended void (as observed in the external carotid artery on both sides in image* ***A****); 5= a combination of an extended void and several small signal voids (as observed in the external carotid artery on both sides in image* ***B****); 6= the signal is no longer visible (as shown at the pterygo portion of the pterygopalatine artery in image* ***A*** *and* ***B****). The enlarge view of alterations is shown in* ***C)****.* ***(D)*** *MCA alteration mean score in control and Tg2576 mice with age. Values are mean ± SE (error bars); one-tail student T test; *P <0.05; n = 4.*

Visibility of alterations in individual slices of MRA data sets validates the changes seen in 3D MIP in Tg2576 mice. An age-dependent evaluation of CNR changes was performed in the source data images for every mouse for MCA and AComA (Figs. 2.5C and D). In both control and Tg2576 mice, an overall decrease in vessel CNR was observed with age. However, the decrease in CNR was more significant in Tg2576 mice than in control mice, in particular at the age of 18 months (Figs. 2.5C and D). A 3D representation of age-dependent changes seen in AComA in control and Tg2576 mice is shown in Fig. 2.5E. The arteries such as ACA, and OlfA in Tg2576 mice also showed a decreasing trend in CNR as compared with control mice, although this decrease did not reach statistical significance (supplementary Fig. 2.1S). Age-dependent increase in blood flow defects was also observed in a small branch of common carotid artery in Tg2576 mice (Fig.2.2 S).

Thus, our results show that blood flow alterations in Tg2576 mice can be very well detected with MRA at 17.6 T and can be followed longitudinally in the same mice with age. The blood flow abnormalities detected by MRA in the Tg2576 mice are consistent

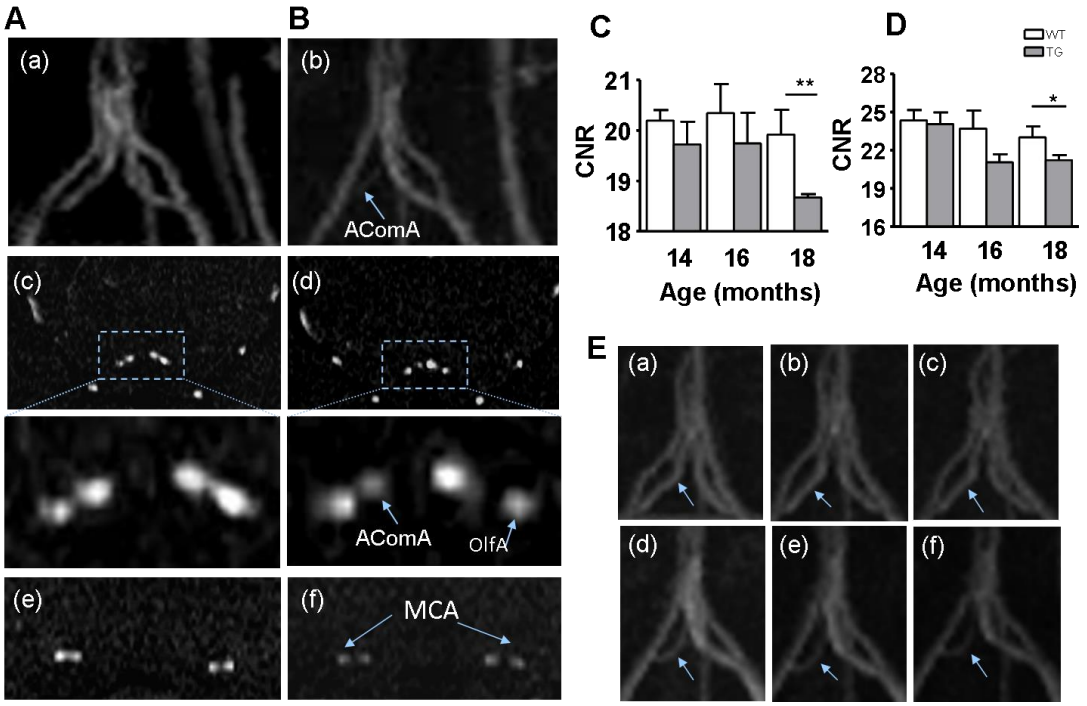

Fig. 2.5. *Representative MIP images and source-slice data sets of an 18-month-old control* ***(A)*** *and Tg2576 mouse* ***(B)****. Tg2576 mouse exhibited severe blood flow alteration at one of the AComA as depicted by arrow (b) which was not visible in control mice (a). The slices of 3D angio data collected in the 17.6 T magnet indicating the regions used for the signal intensity evaluation for control (c, e) and Tg2576 (d, f) mice. Severe decrease of signal intensity was observed in AComA and MCA in Tg2576 mice.* ***(C)*** *Age-dependent changes in contrast-to-noise ratio (CNR) of AComA* ***(C)*** *and MCA* ***(D)*** *in control and Tg2576 mice. One-tail student T test was used for statistical evaluation. *P <0.05 and **P <0.01. The number of animals per age is as follows: control mice: age 14th month (n = 8), 16th month (n = 6), and 18th month (n = 6); Tg2576 age 14th month (n = 8), 16th month (n =7), and 18th month (n = 6).* ***(E)*** *Age-dependent changes in AComA in a control mouse (a−c) and a Tg2576 (d-f) mouse imaged at the age of 14 (a,d); 16 (b, e) and 18 (c, f) months.*

with cerebrovascular abnormalities reported in human AD patients (43,44). These findings suggest that Tg2576 is a valid mouse model for studying CAA related blood flow abnormalities *in vivo*. The hypointensities seen in 3D MIP of the mouse brain might be caused by a number of interrelated factors such as changes in vessel morphology (narrowing, compression, partial occlusion *etc*) and/or complex blood flow patterns (turbulent flow, reversal, acceleration or very slow blood flow) (23,25). Any of these factors can lead to loss of signal within cerebral arteries. Beckman *et al*. (2003) used the corrosion casts method to identify the underlying structural changes in the cerebrovascular system of APP23 AD mouse and showed that morphological anomalies of the vessel, such as constrictions and/or narrowing, occur at the sites where altered

perfusion were detected by MRA (24). More recently the study of Thal *et al*. (2009) has signified the association of CAA with cerebral blood flow disturbance seen in MRA in APP23 mice (18). The blood flow alterations in Tg2576 seen in the present study may be associated with CAA related elevation of Aβ levels in the vessel wall (31). Figure 2.6 shows the angiogram of an 18 month-old wild-type and a Tg2576 mouse, indicating flow disturbance in the branches of the MCA in Tg2576 mice (Fig. 2.6A-D). Histological staining of Aβ confirmed the presence of CAA in the territory of the pial branches of the MCA of the Tg2576 mouse, but not in the wild-type mouse (Fig. 2.6 E-F), suggesting a causal role of CAA on the blood flow alterations monitored by MRA. In addition, the immunohistochemistry also shows large prevalence of the Aβ40 isoform in cerebral vessel walls of Tg2576 mice, as compared to the Aβ42 isoform (Fig. 2.7A-C). These results are consistent with previous reports showing that dense plaques and CAA in Tg2576 mice are predominantly composed of Aβ40 (33,45) and that Aβ40 could play a role in the cerebrovascular alterations observed in Alzheimer's disease (46,47).

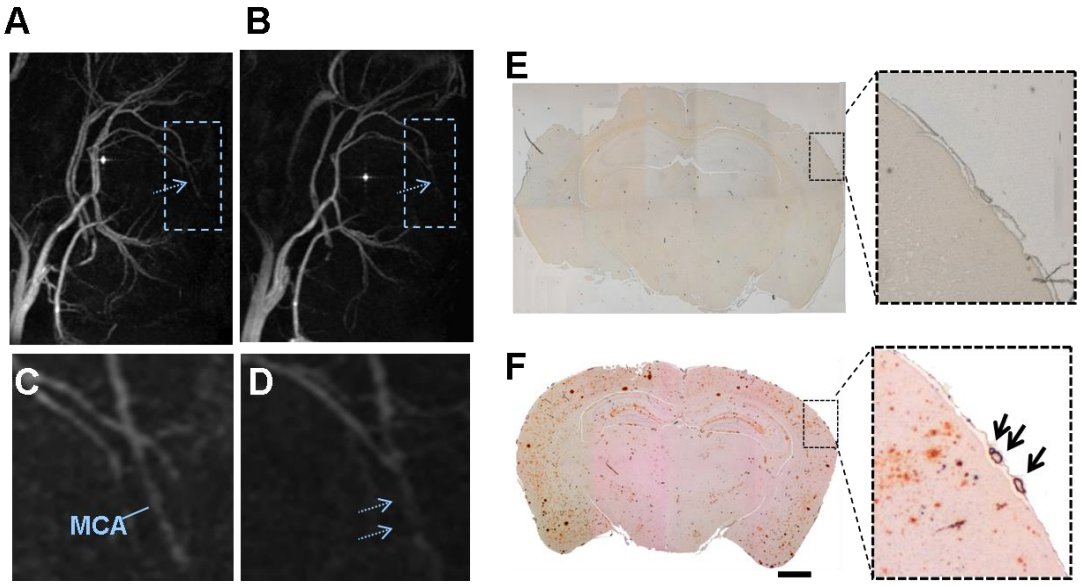

Fig. 2.6. *Angiogram in sagittal view of an 18-month-old wild-type* ***(A)*** *and a Tg2576 mouse* ***(B)****. The magnified subsampled area of the wild-type mouse shows the visible blood flow signal from branches of middle cerebral artery (MCA)* ***(C)****, however in the Tg2576 mouse a marked decrease in blood flow signal intensity from the branches of the MCA was observed* ***(D)****. Histological section of the brain of an 18-month-old wild-type* ***(E)*** *and a Tg2576 mouse* ***(F),*** *stained with monoclonal anti-Aβ (6E10) antibodies. CAA was detected in the territory of the pial branches of the MCA of the Tg2576 mouse, as can be clearly seen (arrows) in the magnified subsampled area on the right in* ***(F)****. Scale bar, 1mm.*

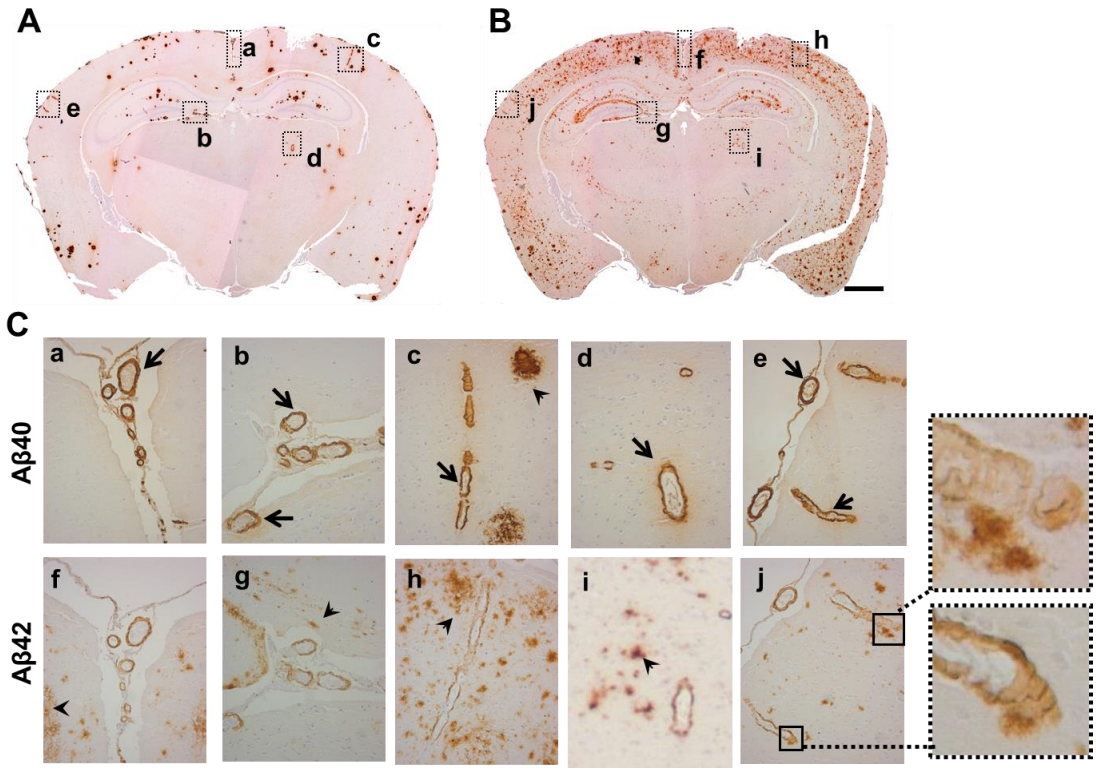

Fig. 2.7. *CAA detected in the brain sections of 23-month-old Tg2576 mouse stained with anti Aβ40* ***(A)*** *and anti Aβ42* ***(B)****. Magnified subsample areas of* ***A*** *(a-e) and* ***B*** *(f-j) are depicted in* ***(C).*** *Aβ-positive plaques in the cortex and hippocampus are shown with arrowheads and CAA affected blood vessels are shown with arrows. Plaques attached to vessels in brain sections stained with Aβ42 are depicted in the enlarged view at the right****.*** *Scale bars in A and B, 1mm.*

The magnetic susceptibility effects due to the presence of iron in the amyloid plaques near or around the vessels may create signal voids in MRA that may have no connection with flow disturbance (25). However, we did not observe any severe iron deposition in Tg2576 mouse brain (Fig. 2.3S), thus ruling out the contribution of iron-related susceptibility effects to the signal voids seen in the MRA images for this mouse model.

The frequency and severity of CAA in Tg2576 mice are age related (31). The CAA first accumulates in the anterior region of the brain in large arteries around the 10th month of age and then progress toward smaller vessels distal from the midline and lateral side of the brain (16 months) and finally at an advanced age of 23 months almost all the vessels are affected by CAA (31). Our *in vivo* age-dependent MRA studies have shown severe impairment of blood flow starting only at the older age of 18 months, (Fig. 2.4D and Fig. 2.5 C, D) suggesting that after a certain level of elevation of Aβ, cerebrovascular abnormalities can be observed with MRA in these Tg2576 mice. Consistent with this suggestion, extensive loss of vascular smooth cells correlated with severity of the CAA

was reported in older Tg2576 mice (30,46). These results confirmed that mild amounts of CAA have little or no effect on vessel wall integrity. However, as amounts of CAA increase significant disruptions of vessel wall integrity develop, including considerable losses of vascular smooth cells (46). In addition, a more recent MRA study reported blood flow alterations in the thalamic vessels of APP23 mice and histology results showed capillary CAA association with vessel occlusion and cerebral blood flow disturbances in APP23 mice (18). Despite these findings, in another MRA study drastic cerebral blood flow disturbance was observed in APP23 mice brain, which did not correlate with CAA levels, such that deposits of amyloid plaques were not observed in arteries located in the circle of Willis (48). It was suggested that blood flow abnormalities in the brain might have been caused by soluble Aβ in these mice (48,49). Another study has proposed that small amyloid aggregates associated with the microvasculature lead to morphological and architectural alterations of the vasculature before amyloid plaques appear; resulting in altered local blood flow in APP23 mice (15).

Blood flow alterations associated with increased CAA levels are more severe in APP23 mice (24), compared to the Tg2576 mice (this study). If mainly soluble Aβ in the blood caused severe blood flow alterations in APP23 mice, this effect should have been very drastic in Tg2576 mice, due to the fact that Tg2576 mice have higher levels of soluble Aβ in the blood (24,50,51). It was stressed that the reason for the relatively rare occurrence of CAA in Tg2576 mice and the significant occurrence in APP23 mice can be related with expression levels and genetic background of the transgenic lines (49).

Potential causal factors for cerebral blood flow abnormalities observed in our study and other studies may not be limited to Aβ levels (soluble and/or insoluble), but also other factors that are independent of CAA level might have been contributed blood flow abnormalities (24,25,34,52,53). Vascular oxidative stresses have been related to alterations in cerebrovascular dysfunction in AD (54). Superoxide-producing enzyme NADPH oxidase, a major source of ROS, appears to play a central role in cerebrovascular dysfunction (55). Recently, it has been reported that 12- to 15-month-old Tg2576 mice lacking the catalytic subunit, Nox2, of NADPH oxidase do not develop oxidative stress, cerebrovascular dysfunction, or behavioural deficits, suggesting a potential role for ROS in CAA-induced vessel dysfunction (55). Subsequently it was reported that cerebrovascular dysfunction in aged Tg2576 mice can be fully rescued by antioxidants and the peroxisome proliferator-activated receptor agonist pioglitazone (56). In addition, Aβ induced endothelial dysfunction, which is characterized by impaired

endothelium-dependent vasodilation due to an reduced endothelial production of vasodilators, such as nitric oxide and an increased release of vasoconstrictors including endothelin-1, might be playing a role in cerebral flow abnormalities in AD (57). In spite of this multitude of findings, the causal factors for blood flow abnormalities occurring in vessels of Tg2576 mice and other AD mouse models require further investigation. Being able to follow progression of vascular abnormalities *in vivo* can increase our understanding of such causal factors.

2.4.4 Age-dependent increase in Aβ plaque load

To explore the temporal relationship between *in vivo* plaque load development in the brain tissue and blood flow abnormalities, we performed high-resolution μMRI in parallel to MRA in the same Tg2576 mice with age. Fig. 2.8A depicts *in vivo* T_2–weighted MR images of the brain of a 16 and 23-month-old control and Tg2576 mouse. Hypointense regions corresponding to Aβ plaques were observed in Tg2576 mouse brain and increased with age (Fig. 2.8A.). As expected Aβ plaques were not visible in control mouse brain. The quantitative analysis of Aβ plaque load in cortex in Tg2576 mice between 12 and 18 months of age is shown in Fig. 2.8B. A marked increase in plaque load was observed in Tg2576 mice with age. However, the increase in plaque load was

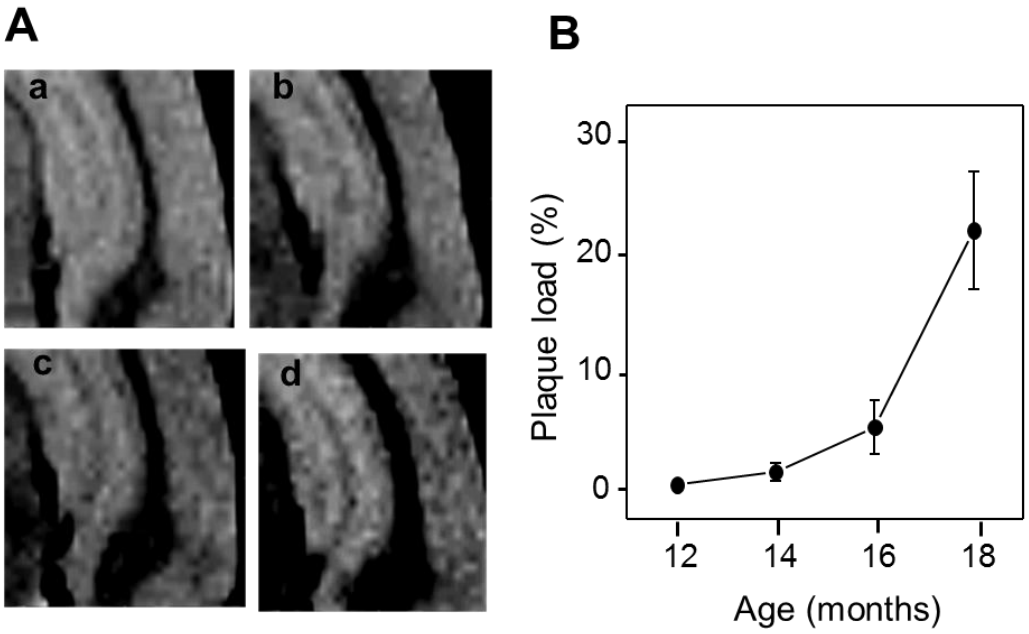

Fig. 2.8. (A) *In vivo T_2–weighted MR images of the brain of a 16 (a, c) and 23 (b, d) month old control (a, b) and Tg2576 mice (c, d) showing that hypointense regions corresponding to Aβ plaques increased with age in the Tg2576 mouse.* ***(B)*** *Age-dependent changes in Aβ plaques load in a Tg2576 mouse detected by μMRI.*

more rapid between 16 and 18 months of age (Fig. 2.8B). This time course matches well with the drastic increase in blood flow defect between 16 and 18 months of age seen in same Tg2576 mice (Fig. 2.4D and Fig. 2.5C, D). These results indicate that severity of amyloid plaque deposition in the brain parenchyma and cerebrovascular deposition of Aβ may be closely linked.

In conclusion, in this study we optimized and performed 3D TOF MRA at 17.6 T for detailed *in vivo* assessment of mouse cerebral vasculature and to compare the age-dependent alteration in cerebral vasculature in control and Tg2576 transgenic mouse models of AD. Our results show that MRA significantly benefits from the ultra-high magnetic field strength (17.6 T) especially to visualize smaller vessels. Age-dependent blood flow abnormalities were observed *in vivo* in MCA and AComA of 18-month-old Tg2576 mice. In addition, histology data showed cerebrovascular amyloid deposition in Tg2576 mice. These results show that vascular abnormalities observed in this study are part of the pathological alterations developed by Tg2576 mouse models of AD. MRA studies at ultra-high magnetic field provide a powerful non-invasive tool to test the effectiveness of putative disease-modifying therapeutic intervention in mouse model of AD *in vivo*.

Acknowledgements

This work was partly supported by grants from Internationale Stichting Alzheimer Onderzoek (ISAO) and Centre for Medical Systems Biology (CMSB). We thank Janneke Ravensbergen, Niels Braakman, Fons Lefeber, Kees Erkelens and S.G. van Duinen for help and useful discussions. The authors like to express their gratitude to Dr. Karen Hsiao Ashe, Department of Neurology, University of Minnesota, USA, for kindly providing three Tg2576 founder mice.

Supplementary Material

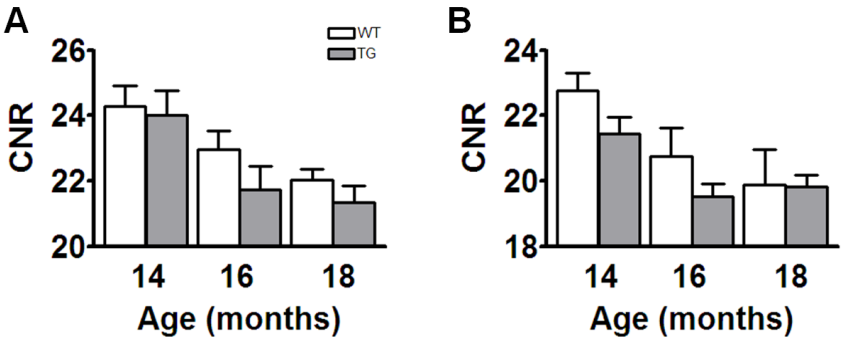

Fig. 2.1S. *Age dependent changes in contrast-to-noise ratio (CNR) of ACA (A) and OlfA (B) in wild type and Tg2576 mice. The number of animals per age is as follow: wild type age 14th month (n = 8), 16th month (n = 6), and 18th month (n =4); Tg2576 age 14th month (n = 8), 16th month (n =7) and 18th month (n = 6). One-tail student T test was used for statistical evaluation. Although a decreasing trend in CNR was observed with age in Tg2576 mice as compared with control mice, the differences were statistically insignificant.*

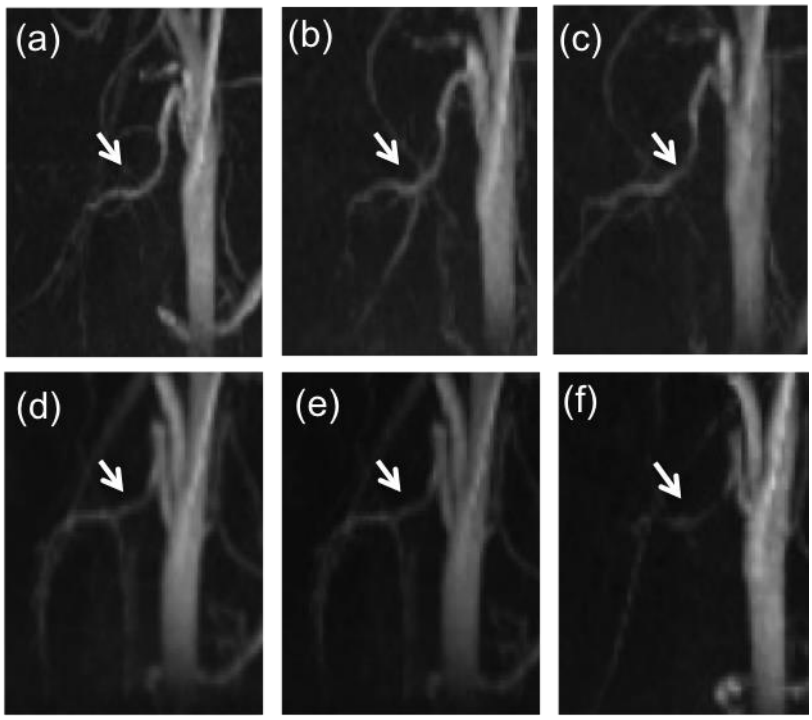

Fig. 2.2S. *Age dependent changes in a small artery branched from CCA in wild type (a, b, c) and Tg2576 (d, e, f) mouse imaged at the age of 14 (a,d); 16 (b, e) and 18 (c, f) months at a magnetic field strength of 17.6 T.*

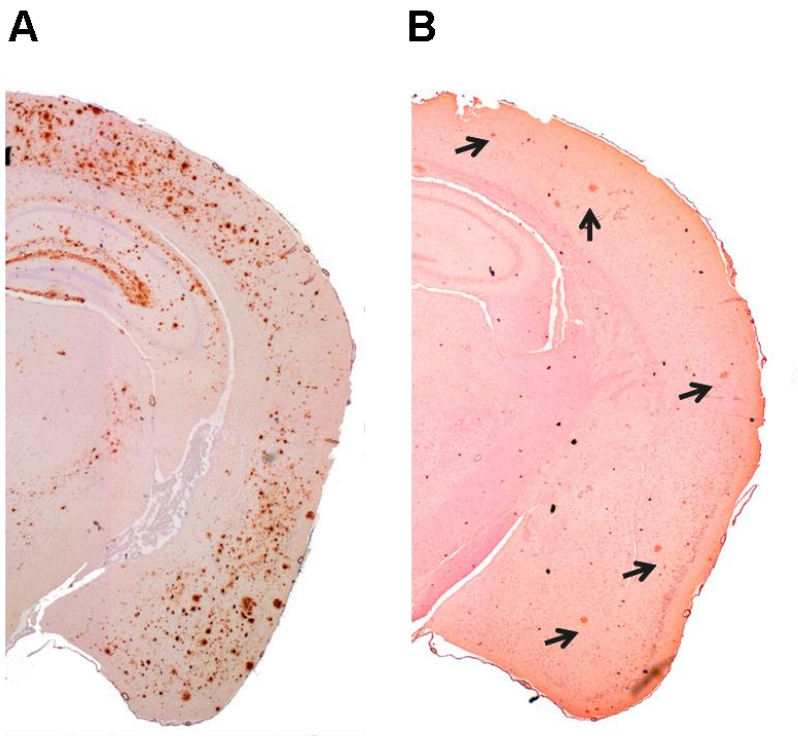

Fig. 2.3S. *Aβ plaques and iron in the adjacent brain sections of an 18-month-old Tg2576 mouse. Brain sections were stained with* ***(a)*** *an Aβ antibody or* ***(b)*** *Perl's reaction following 3, 3-diaminobenzidine enhancement. Arrows indicate presence of iron. Only few plaques contain iron. Since no severe iron deposition was seen in Tg2576 mouse brain, we can rule out the possible contribution of iron-related susceptibility effects to the signal voids in vessels seen on MRA in this mouse model.*

References

1. Duyckaerts C, Potier MC, Delatour B. Alzheimer disease models and human neuropathology: similarities and differences. Acta Neuropathol 2008;115(1):5-38.
2. Schliebs R, Arendt T. The cholinergic system in aging and neuronal degeneration. Behav Brain Res 2011;221:555-563.
3. Kumar-Singh S. Cerebral amyloid angiopathy: pathogenetic mechanisms and link to dense amyloid plaques. Genes Brain Behav 2008;7 Suppl 1:67-82.
4. Biffi A, Greenberg SM. Cerebral amyloid angiopathy: a systematic review. J Clin Neurol 2011;7(1):1-9.
5. Revesz T, Holton JL, Lashley T, Plant G, Rostagno A, Ghiso J, Frangione B. Sporadic and familial cerebral amyloid angiopathies. Brain Pathol 2002;12(3):343-357.
6. Pezzini A, Del Zotto E, Volonghi I, Giossi A, Costa P, Padovani A. Cerebral amyloid angiopathy: a common cause of cerebral hemorrhage. Curr Med Chem 2009;16(20):2498-2513.
7. Ghiso J, Frangione B. Cerebral amyloidosis, amyloid angiopathy, and their relationship to stroke and dementia. J Alzheimers Dis 2001;3(1):65-73.
8. Ellis RJ, Olichney JM, Thal LJ, Mirra SS, Morris JC, Beekly D, Heyman A. Cerebral amyloid angiopathy in the brains of patients with Alzheimer's disease: the CERAD experience, Part XV. Neurology 1996;46(6):1592-1596.
9. Pfeifer LA, White LR, Ross GW, Petrovitch H, Launer LJ. Cerebral amyloid angiopathy and cognitive function: the HAAS autopsy study. Neurology 2002;58(11):1629-1634.
10. Yamada M. Cerebral amyloid angiopathy: an overview. Neuropathology 2000;20(1):8-22.
11. Smith EE, Vijayappa M, Lima F, Delgado P, Wendell L, Rosand J, Greenberg SM. Impaired visual evoked flow velocity response in cerebral amyloid angiopathy. Neurology 2008;71:1424-1430.
12. Hawkes CA, Hartig W, Kacza J, Schliebs R, Weller RO, Nicoll JA, Carare RO. Perivascular drainage of solutes is impaired in the ageing mouse brain and in the presence of cerebral amyloid angiopathy. Acta Neuropathol 2011;121(4):431-443.
13. Herzig MC, Winkler DT, Burgermeister P, Pfeifer M, Kohler E, Schmidt SD, Danner S, Abramowski D, Sturchler-Pierrat C, Burki K, van Duinen SG, Maat-

Schieman ML, Staufenbiel M, Mathews PM, Jucker M. Abeta is targeted to the vasculature in a mouse model of hereditary cerebral hemorrhage with amyloidosis. Nat Neurosci 2004;7(9):954-960.

14. Merlini M, Meyer EP, Ulmann-Schuler A, Nitsch RM. Vascular beta-amyloid and early astrocyte alterations impair cerebrovascular function and cerebral metabolism in transgenic arcAbeta mice. Acta Neuropathol 2011.
15. Meyer EP, Ulmann-Schuler A, Staufenbiel M, Krucker T. Altered morphology and 3D architecture of brain vasculature in a mouse model for Alzheimer's disease. Proc Natl Acad Sci U S A 2008;105(9):3587-3592.
16. Nishitsuji K, Tomiyama T, Ishibashi K, Kametani F, Ozawa K, Okada R, Maat-Schieman ML, Roos RA, Iwai K, Mori H. Cerebral vascular accumulation of Dutch-type Abeta42, but not wild-type Abeta42, in hereditary cerebral hemorrhage with amyloidosis, Dutch type. J Neurosci Res 2007;85(13):2917-2923.
17. Poduslo JF, Hultman KL, Curran GL, Preboske GM, Chamberlain R, Marjanska M, Garwood M, Jack CR, Jr., Wengenack TM. Targeting Vascular Amyloid in Arterioles of Alzheimer Disease Transgenic Mice With Amyloid beta Protein Antibody-Coated Nanoparticles. J Neuropathol Exp Neurol 2011;70(8):653-661.
18. Thal DR, Capetillo-Zarate E, Larionov S, Staufenbiel M, Zurbruegg S, Beckmann N. Capillary cerebral amyloid angiopathy is associated with vessel occlusion and cerebral blood flow disturbances. Neurobiol Aging 2009;30(12):1936-1948.
19. Burger S, Noack M, Kirazov LP, Kirazov EP, Naydenov CL, Kouznetsova E, Yafai Y, Schliebs R. Vascular endothelial growth factor (VEGF) affects processing of amyloid precursor protein and beta-amyloidogenesis in brain slice cultures derived from transgenic Tg2576 mouse brain. Int J Dev Neurosci 2009;27(6):517-523.
20. Burger S, Yafai Y, Bigl M, Wiedemann P, Schliebs R. Effect of VEGF and its receptor antagonist SU-5416, an inhibitor of angiogenesis, on processing of the beta-amyloid precursor protein in primary neuronal cells derived from brain tissue of Tg2576 mice. Int J Dev Neurosci 2010;28(7):597-604.
21. Braakman N, Matysik J, van Duinen SG, Verbeek F, Schliebs R, de Groot HJ, Alia A. Longitudinal assessment of Alzheimer's beta-amyloid plaque development in transgenic mice monitored by in vivo magnetic resonance microimaging. J Magn Reson Imaging 2006;24(3):530-536.

22. Kantarci K, Petersen R, Boeve B, Knopman D, Tang-Wai D, O'Brien P, Weigand S, Edland S, Smith G, Ivnik R. 1H MR spectroscopy in common dementias. Neurology 2004;63(8):1393 - 1398.
23. Beckmann N. Probing cerebrovascular alterations in Alzheimer's disease using MRI: From transgenic models to patients. Curr Med Imaging Rev 2011;7:51-61.
24. Beckmann N, Schuler A, Mueggler T, Meyer EP, Wiederhold KH, Staufenbiel M, Krucker T. Age-dependent cerebrovascular abnormalities and blood flow disturbances in APP23 mice modeling Alzheimer's disease. J Neurosci 2003;23(24):8453-8459.
25. El Tannir El Tayara NT, Delatour B, Volk A, Dhenain M. Detection of vascular alterations by in vivo magnetic resonance angiography and histology in APP/PS1 mouse model of Alzheimer's disease. MAGMA 2010;23(1):53-64.
26. Hu X, Norris DG. Advances in high-field magnetic resonance imaging. Annu Rev Biomed Eng 2004;6:157-184.
27. van de Ven RC, Hogers B, van den Maagdenberg AM, de Groot HJ, Ferrari MD, Frants RR, Poelmann RE, van der Weerd L, Kiihne SR. T(1) relaxation in in vivo mouse brain at ultra-high field. Magn Reson Med 2007;58(2):390-395.
28. Fushimi Y, Miki Y, Kikuta K, Okada T, Kanagaki M, Yamamoto A, Nozaki K, Hashimoto N, Hanakawa T, Fukuyama H, Togashi K. Comparison of 3.0- and 1.5-T three-dimensional time-of-flight MR angiography in moyamoya disease: preliminary experience. Radiology 2006;239(1):232-237.
29. Hsiao K, Chapman P, Nilsen S, Eckman C, Harigaya Y, Younkin S, Yang F, Cole G. Correlative memory deficits, Abeta elevation, and amyloid plaques in transgenic mice. Science 1996;274(5284):99-102.
30. Christie R, Yamada M, Moskowitz M, Hyman B. Structural and functional disruption of vascular smooth muscle cells in a transgenic mouse model of amyloid angiopathy. Am J Pathol 2001;158(3):1065-1071.
31. Domnitz SB, Robbins EM, Hoang AW, Garcia-Alloza M, Hyman BT, Rebeck GW, Greenberg SM, Bacskai BJ, Frosch MP. Progression of cerebral amyloid angiopathy in transgenic mouse models of Alzheimer disease. J Neuropathol Exp Neurol 2005;64(7):588-594.
32. Holtzman DM, Fagan AM, Mackey B, Tenkova T, Sartorius L, Paul SM, Bales K, Ashe KH, Irizarry MC, Hyman BT. Apolipoprotein E facilitates neuritic and

cerebrovascular plaque formation in an Alzheimer's disease model. Ann Neurol 2000;47(6):739-747.

33. Kumar-Singh S, Pirici D, McGowan E, Serneels S, Ceuterick C, Hardy J, Duff K, Dickson D, Van Broeckhoven C. Dense-core plaques in Tg2576 and PSAPP mouse models of Alzheimer's disease are centered on vessel walls. Am J Pathol 2005;167(2):527-543.
34. Shin HK, Jones PB, Garcia-Alloza M, Borrelli L, Greenberg SM, Bacskai BJ, Frosch MP, Hyman BT, Moskowitz MA, Ayata C. Age-dependent cerebrovascular dysfunction in a transgenic mouse model of cerebral amyloid angiopathy. Brain 2007;130(Pt 9):2310-2319.
35. Hennig J, Nauerth A, Friedburg H. RARE imaging: a fast imaging method for clinical MR. Magn Reson Med 1986;3(6):823-833.
36. Dorr A, Sled JG, Kabani N. Three-dimensional cerebral vasculature of the CBA mouse brain: a magnetic resonance imaging and micro computed tomography study. Neuroimage 2007;35(4):1409-1423.
37. Beckmann N, Stirnimann R, Bochelen D. High-resolution magnetic resonance angiography of the mouse brain: application to murine focal cerebral ischemia models. J Magn Reson 1999;140(2):442-450.
38. Okuyama S, Okuyama J, Tamatsu Y, Shimada K, Hoshi H, Iwai J. The arterial circle of Willis of the mouse helps to decipher secrets of cerebral vascular accidents in the human. Med Hypotheses 2004;63(6):997-1009.
39. Reese T, Bochelen D, Sauter A, Beckmann N, Rudin M. Magnetic resonance angiography of the rat cerebrovascular system without the use of contrast agents. NMR Biomed 1999;12(4):189-196.
40. Schambach SJ, Bag S, Steil V, Isaza C, Schilling L, Groden C, Brockmann MA. Ultrafast high-resolution in vivo volume-CTA of mice cerebral vessels. Stroke 2009;40(4):1444-1450.
41. Howles GP, Ghaghada KB, Qi Y, Mukundan S, Jr., Johnson GA. High-resolution magnetic resonance angiography in the mouse using a nanoparticle blood-pool contrast agent. Magn Reson Med 2009;62(6):1447-1456.
42. Dydak U, Schar M. MR spectroscopy and spectroscopic imaging: comparing 3.0 T versus 1.5 T. Neuroimaging Clin N Am 2006;16(2):269-283, x.
43. Franceschi M, Alberoni, M., Bressi, S., Canal, N., Comi, G., Fazio, F., Grassi, F., Perani, D., Volonte, M.A. Correlations between cognitive impairment, middle

cerebral artery flow velocity and cortical glucose metabolism in the early phase of Alzheimer's disease. Dementia 1995;6:32-38.

44. Ishibashi K, Tanaka K, Nakabayashi T, Nakamura M, Uchiyama M, Okawa M. Latent cerebral artery stenoses on magnetic resonance angiography in a patient diagnosed as probable Alzheimer disease. Psychiatry and clinical neurosciences 1998;52(1):93-96.
45. Harigaya Y, Tomidokoro Y, Ikeda M, Sasaki A, Kawarabayashi T, Matsubara E, Kanai M, Saido TC, Younkin SG, Shoji M. Type-specific evolution of amyloid plaque and angiopathy in APPsw mice. Neurosci Lett 2006;395(1):37-41.
46. Han BH, Zhou ML, Abousaleh F, Brendza RP, Dietrich HH, Koenigsknecht-Talboo J, Cirrito JR, Milner E, Holtzman DM, Zipfel GJ. Cerebrovascular dysfunction in amyloid precursor protein transgenic mice: contribution of soluble and insoluble amyloid-beta peptide, partial restoration via gamma-secretase inhibition. J Neurosci 2008;28(50):13542-13550.
47. Niwa K, Carlson GA, Iadecola C. Exogenous A beta1-40 reproduces cerebrovascular alterations resulting from amyloid precursor protein overexpression in mice. J Cereb Blood Flow Metab 2000;20(12):1659-1668.
48. Bartzokis G, Cummings JL, Sultzer D, Henderson VW, Nuechterlein KH, Mintz J. White matter structural integrity in healthy aging adults and patients with Alzheimer disease: a magnetic resonance imaging study. Arch Neurol 2003;60(3):393-398.
49. Burgermeister P, Calhoun ME, Winkler DT, Jucker M. Mechanisms of cerebrovascular amyloid deposition. Lessons from mouse models. Ann N Y Acad Sci 2000;903:307-316.
50. Kuo YM, Beach TG, Sue LI, Scott S, Layne KJ, Kokjohn TA, Kalback WM, Luehrs DC, Vishnivetskaya TA, Abramowski D, Sturchler-Pierrat C, Staufenbiel M, Weller RO, Roher AE. The evolution of A beta peptide burden in the APP23 transgenic mice: implications for A beta deposition in Alzheimer disease. Mol Med 2001;7(9):609-618.
51. Kuo YM, Crawford F, Mullan M, Kokjohn TA, Emmerling MR, Weller RO, Roher AE. Elevated A beta and apolipoprotein E in A betaPP transgenic mice and its relationship to amyloid accumulation in Alzheimer's disease. Mol Med 2000;6(5):430-439.

52. Anderson CM, Saloner D, Tsuruda JS, Shapeero LG, Lee RE. Artifacts in maximum-intensity-projection display of MR angiograms. AJR Am J Roentgenol 1990;154(3):623-629.
53. Thal DR, Griffin WS, de Vos RA, Ghebremedhin E. Cerebral amyloid angiopathy and its relationship to Alzheimer's disease. Acta Neuropathol 2008;115:599-609.
54. Bennett S, Grant MM, Aldred S. Oxidative stress in vascular dementia and Alzheimer's disease: a common pathology. J Alzheimers Dis 2009;17(2):245-257.
55. Park L, Zhou P, Pitstick R, Capone C, Anrather J, Norris EH, Younkin L, Younkin S, Carlson G, McEwen BS, Iadecola C. Nox2-derived radicals contribute to neurovascular and behavioral dysfunction in mice overexpressing the amyloid precursor protein. Proc Natl Acad Sci U S A 2008;105(4):1347-1352.
56. Nicolakakis N, Aboulkassim T, Ongali B, Lecrux C, Fernandes P, Rosa-Neto P, Tong XK, Hamel E. Complete rescue of cerebrovascular function in aged Alzheimer's disease transgenic mice by antioxidants and pioglitazone, a peroxisome proliferator-activated receptor gamma agonist. J Neurosci 2008;28(37):9287-9296.
57. Elesber AA, Bonetti PO, Woodrum JE, Zhu XY, Lerman LO, Younkin SG, Lerman A. Bosentan preserves endothelial function in mice overexpressing APP. Neurobiol Aging 2006;27(3):446-450.

3 Longitudinal monitoring of transverse relaxation time (T_2) changes in the corpus callosum region of a mouse model of Alzheimer' disease*

3.1 Abstract

The corpus callosum is the largest commissural fiber connecting left and right hemisphere of the brain. Emerging evidence suggests that a variety of abnormalities, detected in the microstructure of this white matter fiber, can be an early event in Alzheimer's disease pathology. However, little is known about tissue characteristics of these abnormalities and how these abnormalities evolve during AD progression. In this study, we measured *in vivo* the magnetic resonance T_2 to longitudinally monitor changes in tissue integrity and abnormalities related to myelination and demyelination processes in corpus callosum of AD mouse models. The most striking finding of our study was significant elongation of T_2 values in the corpus callosum at 10, 14, 16 and 18 months of age, compared to age-matched wild-type mice. In contrast, grey matter regions surrounding the corpus callosum, such as the cortex and hippocampus, showed a significant T_2 decrease compared to wild-type mice. Histological analyses clearly revealed demyelination, gliosis and amyloid-plaque deposition in the corpus callosum. Our results suggest that demyelinating and inflammatory pathology may lead to prolonged relaxation times and can mark an early event during Alzheimer's disease progression. To our knowledge, this is the first *in vivo* T_2 study assessing microstructural changes with age in the corpus callosum of the Tg2576 mouse model. It demonstrates the application of T_2 measurements in non-invasively detecting tissue degradation of corpus callosum, which can be early event in disease progression.

3.2 Introduction

Alzheimer's disease is the leading neurodegenerative disorder in the elderly with no effective treatment. The neuropathological features of AD include extracellular deposits of Aβ, intraneuronal fibrillary changes, gliosis, decreased synaptic density,

* Submitted

demyelination, and brain regional atrophy (1,2). Neuropathological diagnosis of AD is still based on the presence of primarily gray matter alterations due to abundant Aβ deposition in the region. In recent years, a strong interest in white matter pathology, *e.g.* demyelination, seen in AD has developed (3-8). Corpus callosum, made of dense myelinated fibers, is the major white matter tract of the brain, and plays an important role in functional connectivity and in cognition (9). It has been suggested that corpus callosum can be susceptible to myelin breakdown during AD progression (4). Demyelination in corpus callosum might already be present in the early stages of AD (10,11), however its role in disease onset and progression remains unclear. There is an emergent need for new studies to monitor corpus callosum changes longitudinally in order to clarify how and when the integrity of corpus callosum changes in AD.

The evidences for white matter abnormalities seen in AD came mainly from postmortem studies (8,12-16). These studies reported reduction of oligodendrocytes, in parallel with axonal degeneration, activation of glial cells and decrease in myelin integrity in white matter of AD patients. To determine changes in myelin integrity and its underlying causes *in vivo*, however, is challenging.

The T_2 measurement serves as a powerful non-invasive MRI tool to explore subtle microstructural changes in white and gray matter regions of brain (17,18). The T_2 values are sensitive to pathology related changes such as demyelination, axonal injury, gliosis and iron deposition. For example, myelin breakdown increases the free tissue water, and thus increases T_2 (19,20), whereas accumulation of iron in tissue decreases T_2 (21). Due to the sensitivity of T_2 to tissue pathology, the changes in T_2 values of various brain regions have been commonly used as a marker in evaluations of aging and a variety of brain disorders such as AD (22-24). In a recent study, an increased T_2 for the genu of the corpus callosum was significantly correlated with an age-related slowing in cognitive processing speed in healthy elderly people (25), suggesting myelin integrity in the corpus callosum as a surrogate marker of assessing cognitive decline. However, little is known about age-related T_2 changes in the corpus callosum region of AD patients (26), and its correlation with pathology such as Aβ deposition and gliosis remains unclear. Studies using transgenic mouse models of AD have the potential to clarify these *in vivo* changes.

The transgenic mouse models of AD, which develop AD like pathology (*e.g.* accumulation of Aβ plaques), serve as valuable biological tools to observe changes in the integrity of the white matter (*e.g.* corpus callosum) and clarify underlying

neurobiological factors (27,28). Although assessment of *in vivo* brain tissue relaxation time in the AD mice models has great potential to detect abnormalities in the corpus callosum and other white matter regions, till now measurements of relaxation times for these AD models has been mainly restricted to gray matter regions of the brain, *e.g.* the cortex and hippocampus, which are prominently affected by Aβ pathology (24,29-32). A summary of previous T_2 studies in a variety of AD mouse models and healthy mice are presented in Table 1.2 (Chapter 1). Only two cross-sectional studies in the APP-PS1 mouse model of AD have measured relaxation time changes in the corpus callosum (31,32). However, longitudinal monitoring of T_2 changes with age in the corpus callosum regions are missing. The Tg2576 is a widely used model of AD. This transgenic AD mouse develops several pathologies, including overproduction of human Aβ40, Aβ42 and gliosis, which fit well with biochemical and epidemiological findings in the disease (33). In addition, Tg2576 mouse models develop progressive learning and memory impairment accompanied by Aβ plaque deposition starting at 9-12 months of age (33). Consequently Tg2576 mice serve as a truly useful model to study a variety of aspects of AD related pathology. The T_2 measurements in corpus callosum of Tg2576 mice have not been attempted so far.

The aim of this study was to probe *in vivo* T_2 changes longitudinally in the corpus callosum region of the Tg2576 mice with age. Since T_2 values have been shown to be sensitive to axonal injury, gliosis and demyelination, probing changes of the T_2 will provide a sensitive marker of dynamic microscopic changes in the corpus callosum, and will eventually yield new insights into the pathology underlying AD. In this study, along with the T_2 for the corpus callosum, values of gray matter regions were also measured. Histological and immunohistochemical analysis were also performed for determining potential neurobiological factors contributing changes in T_2.

3.3 Materials and Methods

3.3.1 Mouse models

In the present study Tg2576 mice were used as a transgenic model of AD (33). These mice contain as the transgene the human amyloid precursor protein (APP695) with the Swedish double mutation (K670N, M671L) under control of a hamster prion protein promoter (33). The founder mice were kindly provided by Dr Karen Hsiao Ashe (University of Minnesota) and used for further breeding. Mice heterozygous for the

transgene and wild-type littermates were on a C57BL/6 x SJL background. At the age of four weeks transgeneity was identified by the polymerase chain reaction of tail DNA, as described elsewhere (33). The N2 generation mice of both genders were studied at the ages of 10–18 months. Age-matched non-transgenic littermates served as controls. In addition, C57BL/6 mice (4 months old) were used for optimization studies. All of the animal experiments were approved by the institutional animal care and animal use committee of the University of Leiden in accordance with the NIH Guide for the Care and Use of Laboratory Animals.

3.3.2 Histology

Histological analyses were performed to assess Aβ deposits, gliosis and demyelination in Tg2576 and wild-type mice. After the MRI experiments, the animals were sacrificed and the brains were fixed in 4% buffered paraformaldehyde (Zinc Formal- Fixx, ThermoShandon, UK) for 48 h. Following fixation, brains were dehydrated and embedded in paraffin. Subsequently coronal sections (5 μm thick) were carefully cut using a vibratome while maintaining as much as possible the same spatial orientation of the mouse brain as in the MRI experiments. These sections were stained with H&E and LFB to compare white matter changes between wild-type and Tg2576 mice, using standard histology protocols (34). LFB dye is commonly used for the demonstration of normal myelin. Myelin fibers are seen blue under the light microscope (34). To stain activated astrocytes, brain sections were subjected to immunohistochemistry using a primary polyclonal anti-GFAP antibody (DAKO) as described earlier (35). To detect activated microglial cells and macrophages, a primary polyclonal anti-IBA-1 antibody 1:1000 (Wako Chemicals, Neuss, Germany) was used as described previously (35). To detect Aβ, brain sections were subjected to immunohistochemistry using monoclonal anti-Aβ42 (BC42), anti Aβ40 (BC40) and polyclonal anti-Aβ 40–42 as described earlier (35). Immunolabeling was visualized by using the ABC kit (Vectastain) according to the manufacturer's instructions. Images of the histological sections were obtained using a Leica DM RE HC microscope interfaced to a Leica DC500 3CCD digital camera.

3.3.3 MRI experiments

Magnetic resonance imaging was performed using a 400 MHz (9.4 T) vertical 89-mm bore magnet equipped with a 1 Tm^{-1} actively shielded imaging gradient insert (Bruker, Germany). A birdcage transmit/receive RF coil (inner diameter 2 cm) was used. The

system was interfaced with a Linux PC running Topspin 2.0 and Paravision 5.0 imaging software (Bruker Biospin GmbH, Germany).

All *in vivo* MRI studies were performed as previously described (35,36). A special mouse head mask was used to fix the head of the animal inside a 20 mm birdcage RF coil and to administer the anesthetic gas during MR experiments. The mice were initially anesthetized with 2% isoflurane (Forane, Abott, UK) in air (0.3 L/min) and oxygen (0.3 L/min). During scanning the level of anesthetic was maintained between 1 and 1.5% to keep the breathing of the animal at a constant rate of ~50 breaths per minute. During scanning, the respiration rate was constantly monitored using a respiration sensor, (placed on the animal's abdomen) connected to a respiration unit. The respiration unit was connected to a computer with Bio-SAM respiration monitoring software (Bruker Biospin, Germany). The mouse's body temperature was kept at a constant temperature by pumping warm water through the gradient system. Cooling of the gradient was performed by circulating water. The rectal body temperature of the mouse during scanning was measured to be 32±1°C.

T_2 values were acquired with the MSME sequence that is based on the CPMG sequence, where transverse magnetization of a 90º pulse is refocused by a train of 180º pulses generating a series of echoes (37,38). The following imaging parameters were used: NA = 2; Number of slices = 10 with a slice thickness of 1.0 mm and an interslice thickness of 1.5 mm; Number of echoes = 12 with echo spacing = 8.5; A TR = 1.5 s with an effective spectral bandwidth = 69.44 kHz; FOV = 2.0 x 2.0 cm; Matrix size = 256 x 256; This yields an effective in-plane resolution of 0.078 x 0.078 mm and a voxel resolution of 6.10 x 10^{-3} mm^3. The total acquisition time for the experiment was 12 min 48 s. To study the dependence of T_2 on the CPMG refocusing interpulse interval (τ), the T_2 measurements were performed using the MSME sequence with 16 echo and 5 different refocusing interpulse intervals, namely 6.6, 8.5, 10.5, 15.5 and 18.5 ms. The last few echoes were discarded to provide five comparable temporal sampling windows, 6.6-79.4 ms, 8.5-85.50 ms, 10.5-94.5 ms, 15.5-93.0, 18.5-92.5 ms acquisitions, respectively. To minimize the contribution of the partial volume effect from cerebrospinal fluid, the ROIs were checked carefully on images collected with thin slices using T_2-weighted MR images acquired with a rapid acquisition with the RARE sequence (39), with following parameters: TR = 6000 ms; TE = 17 ms; FOV = 2.0 x 2.0 cm; Matrix size= 256 x 256; NS = 30, with slice thickness 0.5 mm; interslice thickness = 0.5 mm. To establish the

test–retest reliability of T_2 measurements, the same C57BL/6J mice (n= 5) were scanned twice on two subsequent days.

3.3.4 Data processing

3.3.4.1 Estimation of T_2

To calculate T_2 maps of selected regions, ROIs were drawn manually on the images by using an image sequence analysis tool package (Paravision 5, Bruker), which uses a monoexponential fit function [$y= A+C*\exp(-t/T_2)$], where A stands for the absolute bias, C is the signal intensity, and T_2 represents the transverse relaxation time as usual. ROIs were manually defined for the white matter regions such as the corpus callosum, cerebral peduncle, anterior commissure, and the gray matter regions including the hippocampus, cortex, thalamus, hypothalamus, caudate-putamen and olfactory bulb on a T_2-weighted image using the "Allen Brain Atlas" with the brain explorer program (http://mouse.brain-map.org) as the reference atlas. For all animals, the T_2 was the mean of the ROIs drawn on the right and left sides of the brain, except for the corpus callosum. Two consequent slices were used to delineate the corpus callosum.

3.3.4.2 Statistics

The paired and/or unpaired two-tailed student's t-test was used to compare mean values. Statistical significance was assigned for values of $P < 0.05$. The reliability of the measurements was assessed by computing the ICC2,1 using a 2-way random effects ANOVA model and the absolute agreement definition (40,41). An ICC close to 1.0 indicates high reliability. The ICC can only be 1.0 if the measures are identical.

3.4 Results

3.4.1 Longitudinal monitoring of T_2 changes

Fig. 3.1A shows the ROIs, used to quantify the age-dependent T_2 relaxation time changes in various gray and white matter regions of wild-type and transgenic mouse brain. Before the longitudinal T_2 study, the test-retest reliability of *in vivo* T_2 measurements using the MSME sequence was analyzed by imaging the same mice at two consecutive days.

A

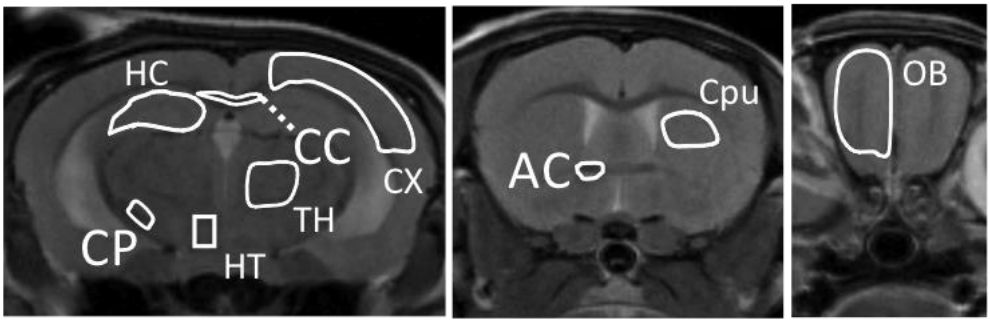

B

Structure	Mean ± SD		$ICC_{2,1}$	Paired t test
	Session 1	Session 2		
White M				
CC	34.34 ± 0.84	34.44 ± 0.79	0.84	ns
CP	32.78 ± 0.20	33.07 ± 0.42	0.12[b]	ns
AC	34.10 ± 0.39	33.62 ± 0.40	0.61[b]	ns
Gray M				
CX	37.64 ± 0.28	37.47 ± 0.28	0.72	ns
HC	38.13 ± 0.10	38.11 ± 0.10	0.90	ns
TH	35.16 ± 0.46	35.20 ± 0.37	0.85	ns
HT	35.44 ± 0.18	35.48 ± 0.30	0.67[b]	ns
Cpu	36.77 ± 0.62	36.33 ± 0.30	0.36[b]	ns
OB	38.55 ± 0.64	38.24 ± 0.59	0.54[b]	ns

Fig. 3.1. (A) Anatomical T_2-weighted MR coronal slices of a mouse brain, showing various brain regions for T_2 measurements acquired with the RARE sequence at 9.4 T. (B) Test-retest reliability measurements were performed for a variety of brain regions [a]ICC = intraclass correlation using a 2-way random-effects ANOVA (subject by session) and the absolute agreement, $P < 0.05$ if otherwise is not indicated ([b]$P > 0.05$). T_2 (ms) means from five subjects, SD, paired t test = session 1 and session 2 results collected from the same mice were compared. $P > 0.05$ in all cases for paired t test. There is a one-day interval between session 1 and session 2. Corpus callosum (CC), hippocampus (HC), cortex (CX) and thalamus (TH), Cerebral peduncle (CP), anterior commissure (AC), Hypothalamus (HT), Caudate putamen (Cpu), Olfactory bulb (OB).

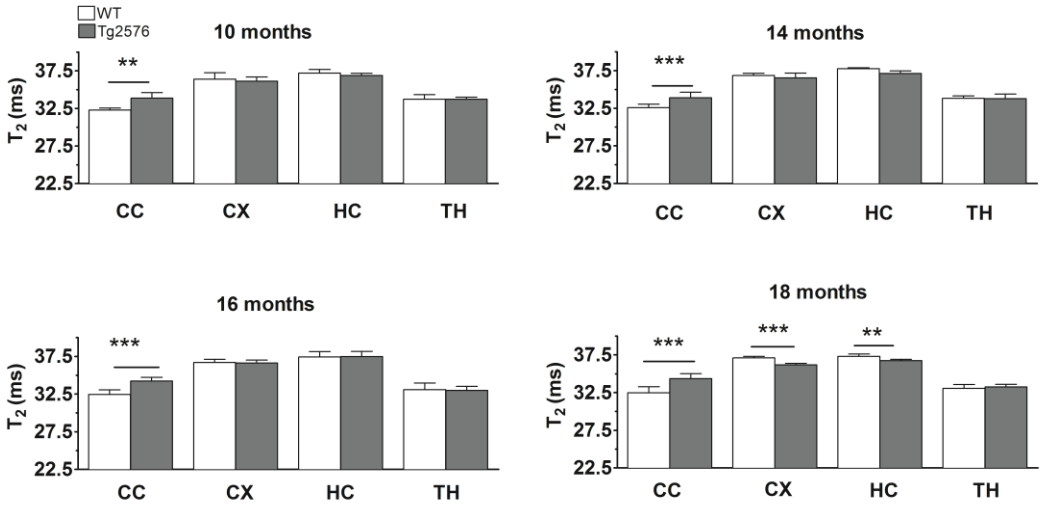

*Fig. 3.2. In vivo T_2 changes in the corpus callosum (CC), cortex (CX), hippocampus (HC) and thalamus (TH) regions of the wild-type (WT) and Tg2576 mice at the age of 10, 14, 16 and 18 months. Values are expressed as mean T_2 in ms ± SD (error bars). Two tailed student t- test, **P < 0.01, ***P < 0.001 significant from T_2 of control mice. The number of animals per age is as follows: control mice: age 10 months (n = 8), 14 months (n = 8), 16 months (n = 6) and 18 months (n = 6);*

Fig. 3.1B shows test-retest reliability results of *in vivo* T_2 measurements in multiple brain regions. Reliability was found to be very high for corpus callosum (ICC = 0.84, P < 0.05), hippocampus (ICC = 0.90, P < 0.05), cortex (ICC = 0.72, P < 0.05) and thalamus (ICC = 0.85, P < 0.05) regions. The ICC values for other regions did not reach statistical significance. The systematic error was checked by a paired t-test and no systematic error was observed between measurements. The dependence of T_2 on the CPMG refocusing interpulse interval (τ) was investigated for cortex and corpus callosum regions (Fig. 3.1S). No statistically significant effect of the interpulse interval in the range of interest (6.6 and 8.5 ms) was observed on the T_2 of the cortex and of corpus callosum. Thus confirming that the changes observed in T_2 values in individual brain structures depend on changes in tissue properties rather than magnetic field disturbances.

Fig. 3.2 shows the variation of the T_2 for various brain regions including the corpus callosum of Tg2576 and wild-type mice with age. As is clear from this figure, T_2 values in the corpus callosum region of Tg2576 mice were significantly higher compared to the T_2 observed for wild-type mice, at 10 (P < 0.005), 14 (P < 0.001), 16 (P < 0.001) and 18

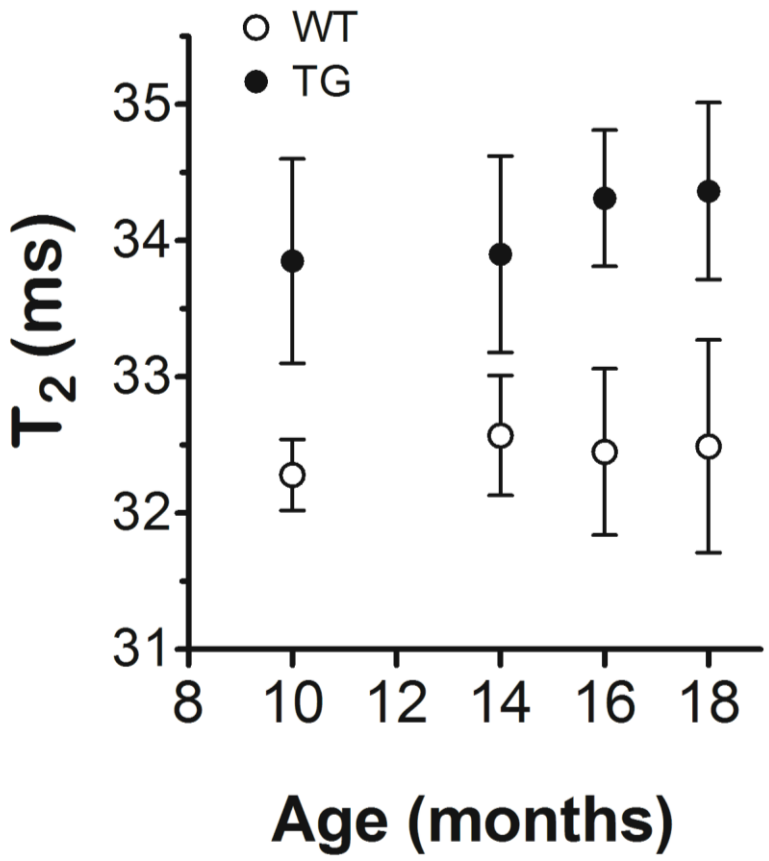

*Fig. 3.3. Age-dependent in vivo T_2 changes of corpus callosum region of the wild-type (WT) and Tg2576 (TG) mice. Values are expressed as mean T_2 in ms ± SD (error bars) (95% C.I.). Two tailed student t-test, **P < 0.01, ***P < 0.001 significant from T_2 of WT mice. The number of animals per age is as follows: control mice: age 10 months (n = 8), 14 months (n = 8), 16 months (n = 6) and 18 months (n = 6); Tg2576: age 10 months (n = 8), 14 months (n = 9), 16 months (n = 8) and 18 months (n = 7).*

months of age (P < 0.001). The T_2 values of the hippocampus and cortex of the Tg2576 miceshowed, however, a significant decrease (P < 0.05) compared to the age-matched wild-type mice at 18 months of age. No significant differences in T_2 values were observed in the thalamus regions between the Tg2576 and wild-type mice.

Fig. 3.3 shows a comparison of the alteration in T_2 with age for the corpus callosum in Tg2576 and wild-type mice. The changes in T_2 values in the corpus callosum in the wild-type and Tg2576 mice were statistically significant at the all ages. As is clear from this figure, a trend of increase in T_2 values of Tg2576 with age was evident between the ages of 14 to 18 months but not in wild-type mice. The level of increase in T_2 in the corpus callosum of Tg2576 mice relative to wild-type mice is 4.09%, 5.45% and 6.40 % for 14, 16, and 18 months of age, respectively.

3.4.2 Histological evaluation

To examine AD related demyelination and other structural changes, histological analysis was performed. Fig. 3.4 (A, B) shows brain slices stained with LFB stain for staining myelin. A marked demyelination was noted in the corpus callosum region of the 18 months old Tg2576 mouse as compared to the wild-type mouse (Figs. 3.4A and B). Furthermore, H&E stain revealed clear vacuolation and demyelination in the corpus callosum region of the Tg2576 mouse (Fig. 3.4D), but not in the wild-type mouse (Fig. 3.4C).

Fig. 3.5 shows brain slices stained for reactive gliosis (astrocytosis and/or microgliosis) in the control (Figs. 3.5A and B) and Tg2576 (Figs. 3.5C and D) mice. Anti-IBA-1 antibody staining was used to identify microglial activation (Figs. 3.5A and C), whereas anti-GFAP antibody staining was used to check the astrocytosis (Figs. 3.5B and D). As is clear from these figures both astrocytosis and microgliosis were observed in the corpus callosum region of the 18 months old Tg2576 mouse brain but not in the wild-type mouse. Black arrows shown in Figs. 3.5 C and D show co-localized reactive microglial and astrocytic cells. Fig. 3.6 depicts the results of Aβ staining in the brain sections of the 18 months Tg2576 mouse. Both Aβ42 (Fig. 3.6C) as well as Aβ40 (Fig. 3.6D) positive plaques were clearly present in the territory of the corpus callosum of Tg2576 mouse but not in wild-type mice (Figs. 3.6A and B). It is noteworthy that activated astrocytes and

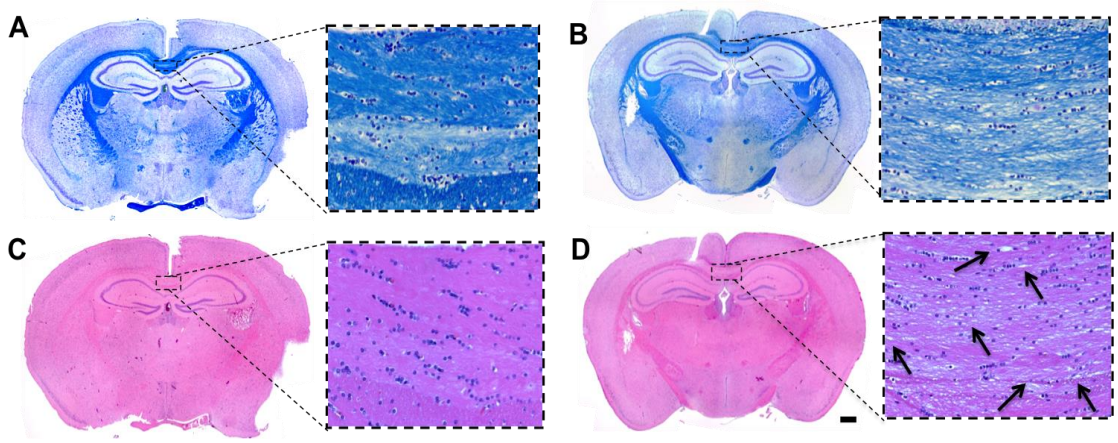

Fig. 3.4: Histological section of the brain of an 18 months old wild-type (A, C) and a Tg2576 (B,D) mouse, stained with the Luxol fast blue (A, B), and hematoxylin and eosin (C, D). Demyelination and vacuolation in the corpus callosum region of transgenic mouse (B and D) is more prominent compared to the wild-type mouse (A, C) as can be clearly seen (arrows) in the magnified subsample areas. Scale bars: 500 µm.

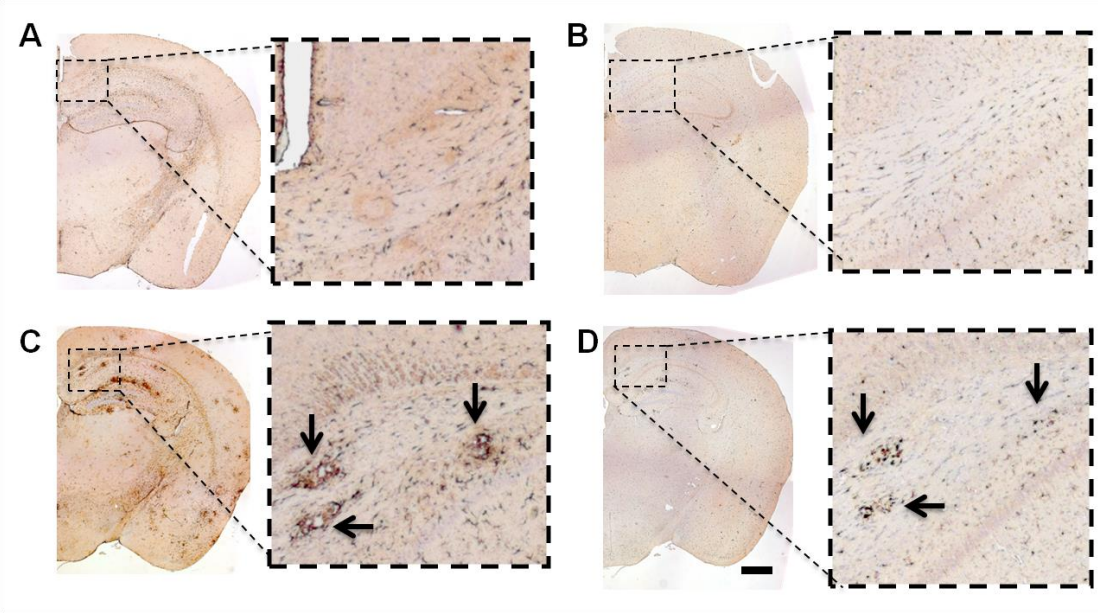

Fig. 3.5. Histological section of the brain of an 18 months old wild-type (A, B) and a Tg2576 (C, D) mouse, stained with anti-GFAP (A, C), anti-IBA1 (B, D) antibodies. Activated astrocytes (C) and microglial activity (D) were detected in the CC region of the transgenic mouse brain as can be clearly seen (arrows) in the magnified subsampled areas. Scale bars: 500 µm.

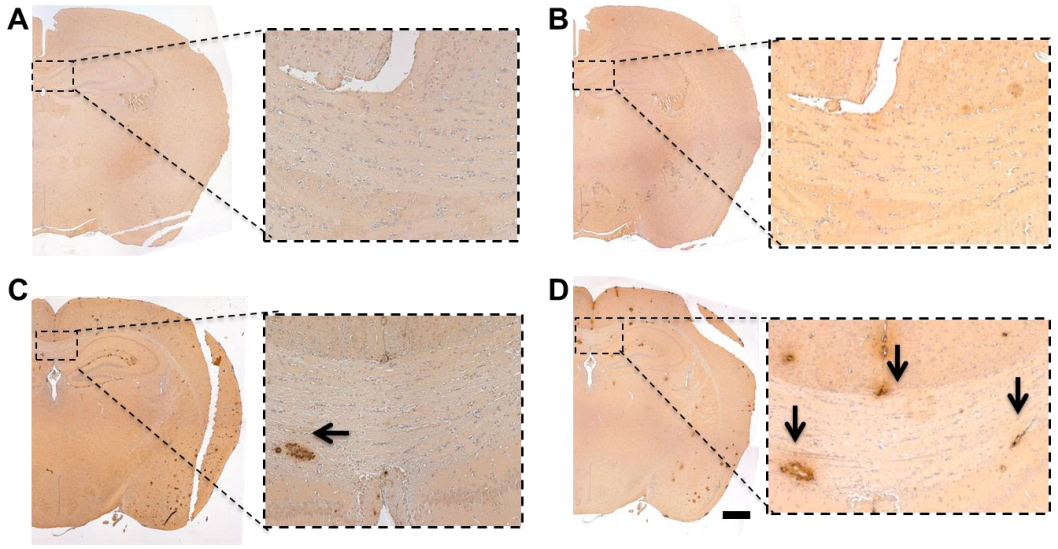

Fig. 3.6. Histological section of the brain of an 18 months old wild-type (A, B) and a Tg2576 (C, D) mouse, stained with anti-Aβ42 (A, C), anti-Aβ40 (B, D) antibodies. Aβ-positive plaques (C, D) were detected in the CC regions of the transgenic mouse brain, as can be clearly seen (arrows) in the magnified subsampled areas. Scale bars: 500 µm.

microglia cells were clustered usually around Aβ deposits as is clear from Fig. 3.7, which reveals the co-registration of Aβ deposition with activated glial cells for the 18 months old Tg2576 mouse.

Fig. 3.8 depicts histological staining of the corpus callosum region of 29 months old Tg2576 mouse. Severe Aβ plaque deposition (Fig. 3.8A-C) as well as a marked increase in the amount of GFAP (Fig. 3.8D), IBA-1 (Fig. 3.8E) and demyelination (Fig 3.8F) were observed at 29 months of age, compared with 18 months old Tg2576 mice. The expression of GFAP and IBA-1 is visible in the same region where the Aβ plaques are deposited. Interestingly Aβ40 positive plaques were larger in size than Aβ42 positive plaques in the corpus callosum of 29 months old mice.

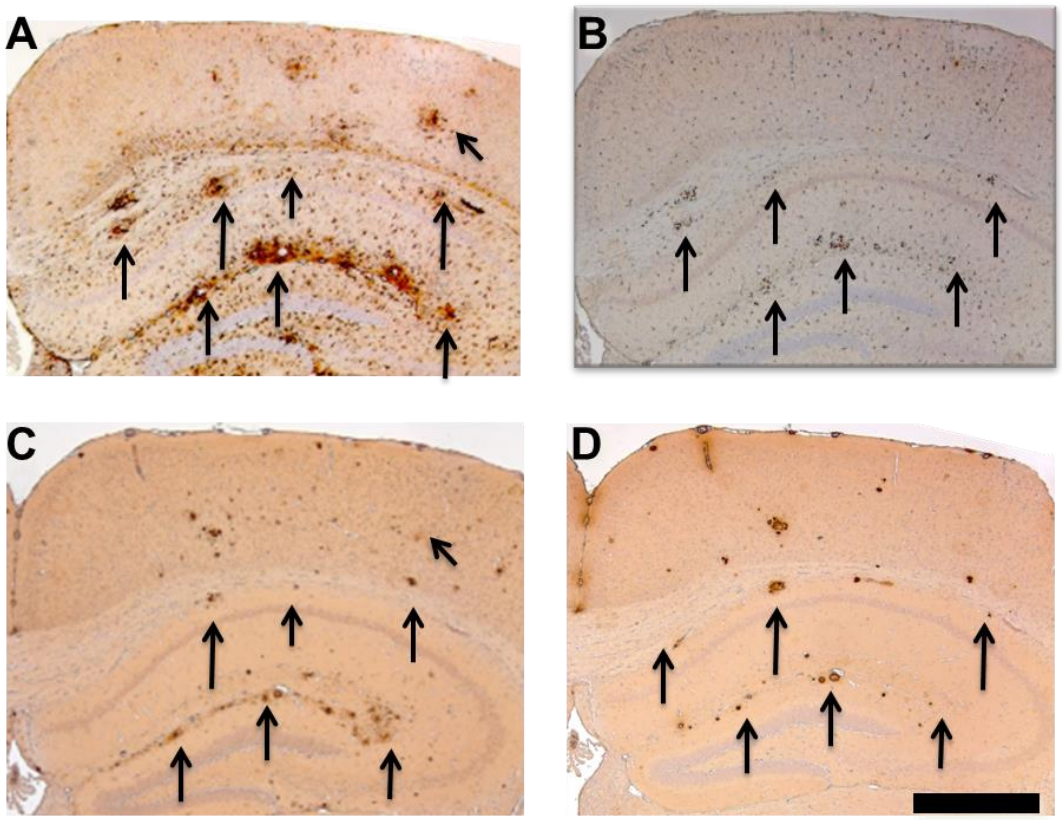

Fig. 3.7. Histological section of the brain of an 18 months old Tg2576 mouse stained with anti-GFAP (A), anti-IBA1 (B) anti-Aβ42 (C), anti-Aβ40 (D) antibodies. Note reactive astrocytes (A) and microglial cells (B) in close proximity to the Aβ deposits (C,D) (black arrows). Scale bars: 500 μm.

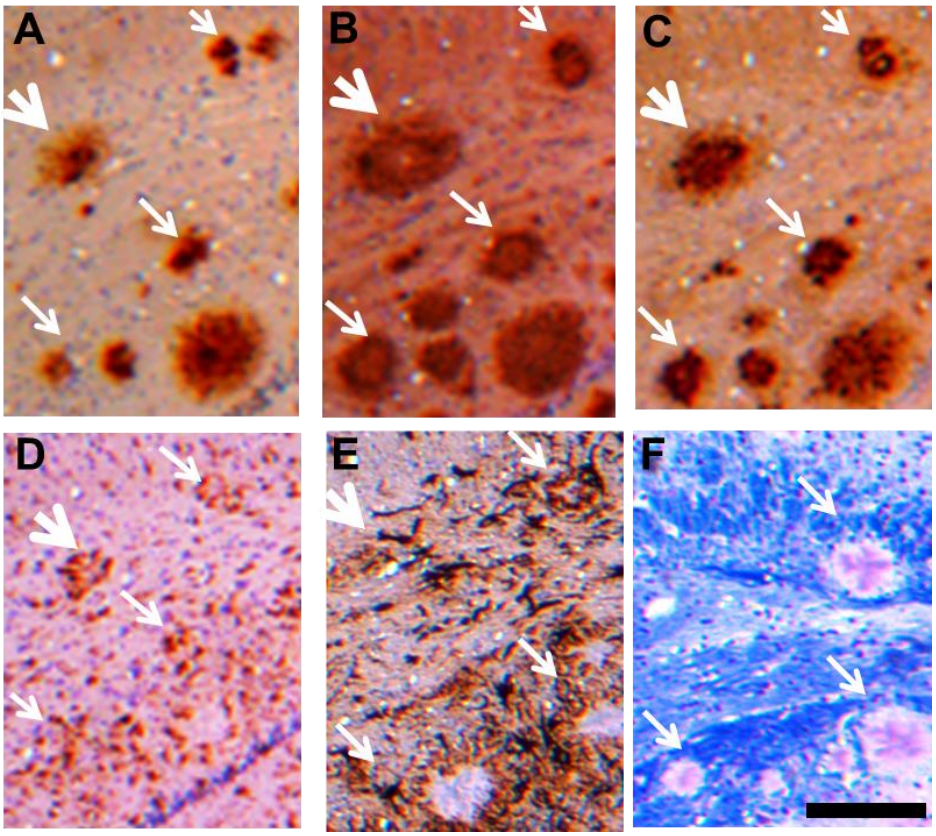

Fig. 3.8. Representative histological sections of the corpus callosum of a 29 months old Tg2576 mouse stained with anti-Aβ42-40 (A), anti-Aβ40 (B), anti-Aβ42 (C), anti-IBA1 (D), anti-GFAP (E) antibodies and myelin reactive stain (F). Arrows depict microglial activity and Aβ deposits in the corpus callosum of the Tg2576 mouse. The areas where Aβ deposits appear show marked demyelination (Arrows). Scale bars: 80 µm..

3.5 Discussion

Recent evidence suggests that the integrity of the corpus callosum changes prior to development of severe AD pathology (42). How and when these integrity changes occur and their contribution to the disease progression *in vivo* remains unclear. In this study, T_2 relaxation measurements were used to probe subtle microstructural changes in the corpus callosum *in vivo*. The study was followed longitudinally to monitor changes in the integrity of corpus callosum during AD progression in the same Tg2576 mice with age, and the results were supported by histological examinations of demyelination, gliosis and Aβ plaques deposition.

3.5.1 Longitudinal T_2 analysis

T_2 changes were followed longitudinally in the corpus callosum region of the wild-type and Tg2576 mice between 10 and 18 months of age. The major finding of this study was a significant prolongation of the T_2 in the corpus callosum, reflecting significant microstructural changes in Tg2576 mice as compared to wild-type mice. The elongation of T_2 values observed in our study is well in line with previous human studies where increase of the T_2 was reported in corpus callosum with increasing dementia score (26). Interestingly, the T_2 of corpus callosum was already significantly longer for 10 months old Tg2576 mice, compared to age-matched wild-type mice, well before the onset of the development of severe AD pathology in this mouse model. These results suggest that microstructural changes in the corpus callosum may occur early during progression of AD (27,28,42,43). A trend of increasing T_2 with age for Tg2576 mice was observed between 14 and 18 months of age, suggesting progressive decrease of the corpus callosum integrity. Microstructural changes in the corpus callosum have also been observed by DTI in Tg2576 mice (28,43) and PDAPP mice (44).

In our study by means of T_2 relaxation measurements, changes in the corpus callosum of Tg2576 mice were observed as early as 10 months of age, in line with a good sensitivity of T_2 to microstructural changes. We focused on T_2 measurements in the splenium, the posterior portion, of the corpus callosum of Tg2576 mice, since several AD studies have indicated that the posterior corpus callosum is affected more than the anterior part of the corpus callosum (45,46). In parallel, electron microscopy studies have revealed partial or complete demyelination in white matter regions near the Aβ plaques in an AD mouse model (PDAPP) (44). For another mouse model of AD (APP/PS1) however, very little change of the T_2 was observed for the corpus callosum (31,32). In this study the region of interest for T_2 measurements was placed close to the genu, the anterior part of the corpus callosum (31,32). It is thus likely that the ROI and corresponding differences in the expression levels of Aβ and the genetic background of the Tg2576 mice and APP/PS1 mice affects the T_2 results in the corpus callosum between both models.

In addition to the corpus callosum, T_2 changes were also investigated in gray matter regions. Our results confirm and extend previous studies (24,47), which showed a notable decrease in T_2 for Aβ plaque rich regions such as the hippocampus and cortex in the old Tg2576 mice, compared to age-matched wild-type mice. Although the cause of the T_2 reduction in grey matter regions remains unclear, previous studies suggested that iron associated Aβ plaques may be involved in reducing the T_2 in AD brain (24,47). In

contrast to Aβ-rich regions, T_2 values did not show any significant change in the thalamus region between wild-type and Tg2576 mice at any age, which was associated with very low Aβ deposition in this region (47).

3.5.2 Evaluation of microstructural changes in wild-type and Tg2576 mice with age

A variety of interconnected pathological factors may contribute to changes in T_2 values. For example myelin breakdown (48,49), axonal damage, gliosis (50) and vacuolation may increase T_2 values and/or signal intensity in T_2-weighted images (51), whereas iron and Aβ deposition decrease T_2. To explore the potential molecular sources of the increased T_2 relaxation time in the corpus callosum in our study, extensive histological analysis was performed. The histological data revealed severe abnormalities, such as marked demyelination, gliosis, vacuolation and Aβ deposition in the corpus callosum of the 18 months old Tg2576 mouse compared to age matched wild-type mouse. Interestingly, normal appearing white matter structure was observed in 11 month of age Tg2576 using myelin staining (data not shown). However a modest increase in activated astrocyte was visible in the corpus callosum of 11 months old Tg2576 mouse as compared to wild-type mouse (Fig. 3.2S). These results suggest that there might be some diffuse changes in normal appearing corpus callosum that activates the astrocytes, and these changes can be detected with quantitative T_2 measurements. While an earlier study showed focal demyelination around Aβ plaques in gray matter and in the superficial subcortical white matter in Tg2576 mice (52), the demyelination in corpus callosum of Tg2576 mice has not been reported previously. The oligodendrocytes, which form myelin sheets, have been shown to be vulnerable to Aβ peptide (53), inflammatory agents, such as nitric oxide and reactive oxygen species (54-56). A recent study showed that when human derived Aβ plaques were injected into corpus callosum of rat brain, a variety of white matter abnormalities such as demyelination, decrease in oligodentrocyte number, and gliosis, occurred (57). Our results are consistent with previous *in vivo* (5) and postmortem studies in humans (12), showing that demyelination in the white matter regions is a marked morphologic component of AD.

In addition, histological analyses revealed that activated glial cells are present in close proximity to Aβ deposits in the corpus callosum as well as the hippocampus and cortex regions supporting earlier findings where a strong association between Aβ and gliosis was observed (28,33,58-65). To observe how pathological changes in corpus callosum

will further evolve at later age, histological analysis was performed in 29 months old Tg2576 mice. Comparison of histological data from 18 months and 29 months old Tg2576 mice show a clear increase in Aβ deposition, gliosis and demyelination with age. How activated astrocytes and microglia contribute to AD process remains unclear. When glial cells are activated, common inflammatory agents, such as the pro-inflammatory cytokines and reactive oxygen species, secreted from these cells can cause demyelination (66) and contribute to the disease progression. The damaged myelin, which is removed by activated microglia, can create microscopic fluid-filled spaces. Eventually this can increase free to bound water ratio, and thus, may increase the T_2 relaxation. However, the interpretation of T_2 variation in AD due to activated microglia is complicated. For example, iron accumulated in microglial cells and Aβ deposits might decrease the T_2 relaxation time (67,68). When astrocytes, which play an important role in regulation of water homeostasis, are activated, they might cause enlargement of the extracellular space, which then becomes filled with more fluid (69), and thus increases the T_2 values. Interestingly, abnormal functioning of a few astrocytic proteins such as aquaporin-4 (AQP4), have been shown to play an important role in the occurrence of white matter microstructural changes including loss of axons and demyelination (70). However, the role of AQP4 and other astrocytic proteins in AD has not been fully revealed. A recent study reported a decrease in AQP4 expression in cultured mouse cortical astrocytes when these cell were subjected to high dose of Aβ42 (71). In another study, down regulation of aquaporin-1 gene expression is shown in AD (72). If AQP4 is down regulated due to Aβ deposits in the corpus callosum region, this might lead to a variety of abnormalities, such as reduced membrane water transport (73). Subsequently these abnormalities might lead to an increase in extracellular fluid and/or demyelination leading to an increase in the T_2 of the affected regions.

The T_2 values of the corpus callosum and gray matter regions of Tg2576 and control mice, acquired in this study, were not absolute (true) T_2 values. The T_2 depends on numerous factors, such as iron content of the tissue, free to bound water ratio and instrument parameters such as magnetic field strength and refocusing pulse interval (τ). Nevertheless, in preclinical and clinical studies, acquiring absolute T_2 values of tissues is not the major concern, a good test-retest reliability of T_2, and whether the value of diseased tissue is normal or not, is more important than absolute accuracy. In the present study good test-retest reliability was observed in the corpus callosum, thalamus, cortex and hippocampus regions of wild-type mice, showing that the T_2 protocol used in this study is reliable with respect to the evaluation of disease progression.

To summarize**,** we have found promising results for the application of T_2 measurements to track changes in the corpus callosum region of Tg2576 transgenic mice. Our results showed highly significant differences in the T_2 values of the corpus callosum region of transgenic mice compared to the non-transgenic control group. The microstructural changes in the corpus callosum region were associated with demyelination and gliosis, which can lead to an increase in T_2 values of the corpus callosum region. This suggests that T_2 is a viable biomarker for the onset of symptoms of AD in this animal model.

Acknowledgements

The authors thank Ingrid Hegeman for assistance in immunohistology and Fons Lefeber, and Karthick Babu Sai Sankar Gupta for their assistance during various stages of MRI measurements and Itimar Ronen (Radiology Department, LUMC, Leiden, The Netherlands), Greetje Vanhoutte and Rafael Delgado Y Palacios (Bio-imaging Lab, Antwerp, Belgium) for useful discussion. We are grateful to Dr. Karen Hsiao Ashe (University of Minesota, USA) for providing the initial three Tg2576 F1 mice for further breeding. This work was partially supported by grants from Internationale Stichting Alzheimer Onderzoek (ISAO) and Centre for Medical Systems Biology (CMSB).

Supplementary Material

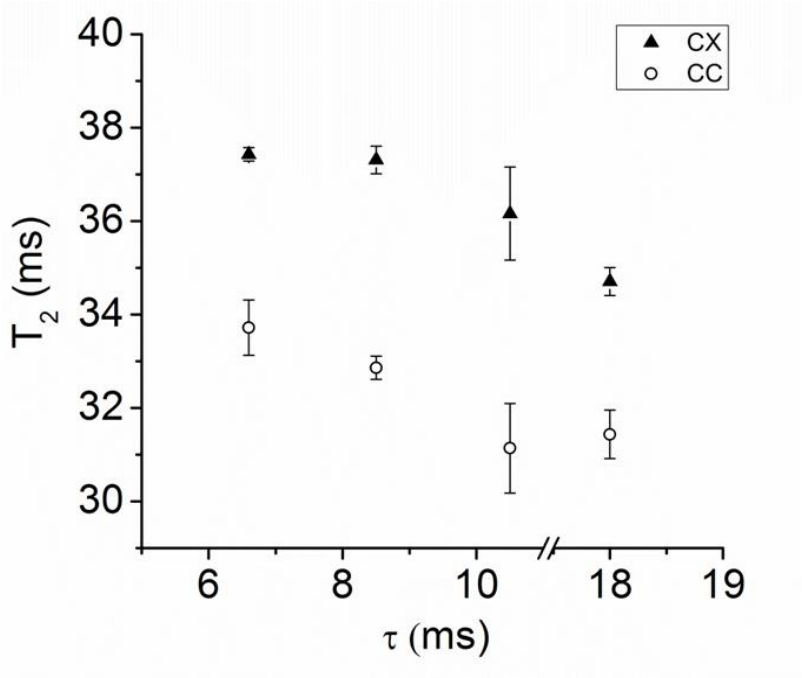

Fig. 3.1S. *Effect of refocusing interpulse interval (τ) on T_2 in cortex (CX) and corpu collasum (CC). T_2 values were measured using MSME sequence with 4 different τ valu namely 6.6, 8.5, 10.5, and 18 ms. Values are expressed as mean T_2 in ms ± standa deviation (error bars); n = 3.*

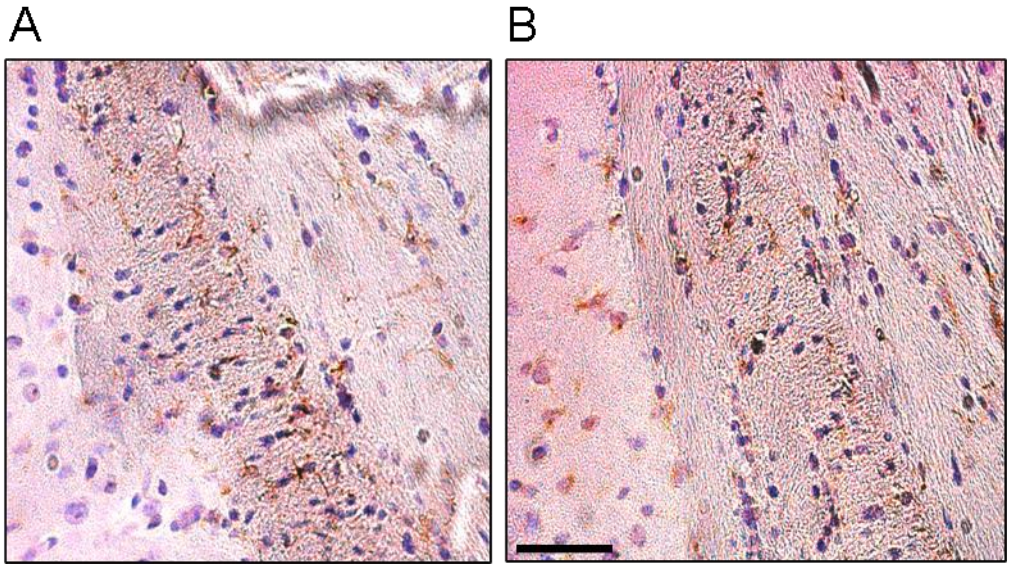

Fig. 3.2S. *Histological section (30 μm thick) of the brain of 11 months old wild type (A) and Tg2576 (B) mouse, stained with anti-GFAP antibodies. Note how reactive astrocytes are more abundant in Tg2576 mouse, as compared to wild type mouse. Scale bars: 125 μm*

References

1. Blennow K, de Leon MJ, Zetterberg H. Alzheimer's disease. Lancet 2006;368(9533):387-403.
2. Masdeu JC, Kreisl WC, Berman KF. The neurobiology of Alzheimer disease defined by neuroimaging. Curr Opin Neurol 2012;25(4):410-420.
3. Bartzokis G, Sultzer D, Lu PH, Nuechterlein KH, Mintz J, Cummings JL. Heterogeneous age-related breakdown of white matter structural integrity: implications for cortical "disconnection" in aging and Alzheimer's disease. Neurobiol Aging 2004;25(7):843-851.
4. Bartzokis G. Age-related myelin breakdown: a developmental model of cognitive decline and Alzheimer's disease. Neurobiol Aging 2004;25(1):5-18; author reply 49-62.
5. Bartzokis G, Cummings JL, Sultzer D, Henderson VW, Nuechterlein KH, Mintz J. White matter structural integrity in healthy aging adults and patients with Alzheimer disease: a magnetic resonance imaging study. Arch Neurol 2003;60(3):393-398.
6. Smith CD, Chebrolu H, Andersen AH, Powell DA, Lovell MA, Xiong S, Gold BT. White matter diffusion alterations in normal women at risk of Alzheimer's disease. Neurobiol Aging 2010;31(7):1122-1131.
7. Gold BT, Powell DK, Andersen AH, Smith CD. Alterations in multiple measures of white matter integrity in normal women at high risk for Alzheimer's disease. Neuroimage 2010;52(4):1487-1494.
8. Roher AE, Weiss N, Kokjohn TA, Kuo YM, Kalback W, Anthony J, Watson D, Luehrs DC, Sue L, Walker D, Emmerling M, Goux W, Beach T. Increased A beta peptides and reduced cholesterol and myelin proteins characterize white matter degeneration in Alzheimer's disease. Biochemistry 2002;41(37):11080-11090.
9. Hinkley LB, Marco EJ, Findlay AM, Honma S, Jeremy RJ, Strominger Z, Bukshpun P, Wakahiro M, Brown WS, Paul LK, Barkovich AJ, Mukherjee P, Nagarajan SS, Sherr EH. The role of corpus callosum development in functional connectivity and cognitive processing. PLoS One 2012;7(8):e39804.
10. Di Paola M, Spalletta G, Caltagirone C. In vivo structural neuroanatomy of corpus callosum in Alzheimer's disease and mild cognitive impairment using different MRI techniques: a review. J Alzheimers Dis 2010;20(1):67-95.

11. Acosta-Cabronero J, Alley S, Williams GB, Pengas G, Nestor PJ. Diffusion tensor metrics as biomarkers in Alzheimer's disease. PLoS One 2012;7(11):e49072.
12. Sjobeck M, Haglund M, Englund E. Decreasing myelin density reflected increasing white matter pathology in Alzheimer's disease--a neuropathological study. Int J Geriatr Psychiatry 2005;20(10):919-926.
13. Englund E, Brun A, Alling C. White matter changes in dementia of Alzheimer's type. Biochemical and neuropathological correlates. Brain 1988;111 (Pt 6):1425-1439.
14. Brun A, Englund E. A white matter disorder in dementia of the Alzheimer type: a pathoanatomical study. Ann Neurol 1986;19(3):253-262.
15. Englund E, Brun A, Persson B. Correlations between histopathologic white matter changes and proton MR relaxation times in dementia. Alzheimer Dis Assoc Disord 1987;1(3):156-170.
16. Sjobeck M, Englund E. Glial levels determine severity of white matter disease in Alzheimer's disease: a neuropathological study of glial changes. Neuropathol Appl Neurobiol 2003;29(2):159-169.
17. Miot-Noirault E, Barantin L, Akoka S, Le Pape A. T2 relaxation time as a marker of brain myelination: experimental MR study in two neonatal animal models. Journal of neuroscience methods 1997;72(1):5-14.
18. MacKay A, Whittall K, Adler J, Li D, Paty D, Graeb D. In vivo visualization of myelin water in brain by magnetic resonance. Magn Reson Med 1994;31(6):673-677.
19. Laule C, Vavasour IM, Moore GR, Oger J, Li DK, Paty DW, MacKay AL. Water content and myelin water fraction in multiple sclerosis. A T2 relaxation study. J Neurol 2004;251(3):284-293.
20. Dyakin VV, Chen Y, Branch CA, Veeranna, Yuan A, Rao M, Kumar A, Peterhoff CM, Nixon RA. The contributions of myelin and axonal caliber to transverse relaxation time in shiverer and neurofilament-deficient mouse models. Neuroimage 2010;51(3):1098-1105.
21. Vymazal J, Brooks RA, Baumgarner C, Tran V, Katz D, Bulte JW, Bauminger R, Di Chiro G. The relation between brain iron and NMR relaxation times: an in vitro study. Magn Reson Med 1996;35(1):56-61.

22. Kumar R, Delshad S, Woo MA, Macey PM, Harper RM. Age-related regional brain T2-relaxation changes in healthy adults. J Magn Reson Imaging 2012;35(2):300-308.
23. Kumar R, Delshad S, Macey PM, Woo MA, Harper RM. Development of T2-relaxation values in regional brain sites during adolescence. Magn Reson Imaging 2010;29(2):185-193.
24. Falangola MF, Dyakin VV, Lee SP, Bogart A, Babb JS, Duff K, Nixon R, Helpern JA. Quantitative MRI reveals aging-associated T2 changes in mouse models of Alzheimer's disease. NMR Biomed 2007;20(3):343-351.
25. Lu PH, Lee GJ, Raven EP, Tingus K, Khoo T, Thompson PM, Bartzokis G. Age-related slowing in cognitive processing speed is associated with myelin integrity in a very healthy elderly sample. Journal of clinical and experimental neuropsychology 2011;33(10):1059-1068.
26. Bondareff W, Raval J, Colletti PM, Hauser DL. Quantitative magnetic resonance imaging and the severity of dementia in Alzheimer's disease. Am J Psychiatry 1988;145(7):853-856.
27. Chen H, Epelbaum S, Delatour B. Fiber Tracts Anomalies in APPxPS1 Transgenic Mice Modeling Alzheimer's Disease. Journal of aging research 2011;2011:281274.
28. Sun SW, Song SK, Harms MP, Lin SJ, Holtzman DM, Merchant KM, Kotyk JJ. Detection of age-dependent brain injury in a mouse model of brain amyloidosis associated with Alzheimer's disease using magnetic resonance diffusion tensor imaging. Experimental neurology 2005;191(1):77-85.
29. Weidensteiner C, Metzger F, Bruns A, Bohrmann B, Kuennecke B, von Kienlin M. Cortical hypoperfusion in the B6.PS2APP mouse model for Alzheimer's disease: comprehensive phenotyping of vascular and tissular parameters by MRI. Magn Reson Med 2009;62(1):35-45.
30. El Tannir El Tayara NT, Volk A, Dhenain M, Delatour B. Transverse relaxation time reflects brain amyloidosis in young APP/PS1 transgenic mice. Magn Reson Med 2007;58(1):179-184.
31. El Tannir El Tayara N, Delatour B, Le Cudennec C, Guegan M, Volk A, Dhenain M. Age-related evolution of amyloid burden, iron load, and MR relaxation times in a transgenic mouse model of Alzheimer's disease. Neurobiol Dis 2006;22(1):199-208.

32. Helpern JA, Lee SP, Falangola MF, Dyakin VV, Bogart A, Ardekani B, Duff K, Branch C, Wisniewski T, de Leon MJ, Wolf O, O'Shea J, Nixon RA. MRI assessment of neuropathology in a transgenic mouse model of Alzheimer's disease. Magn Reson Med 2004;51(4):794-798.
33. Hsiao K, Chapman P, Nilsen S, Eckman C, Harigaya Y, Younkin S, Yang F, Cole G. Correlative memory deficits, Abeta elevation, and amyloid plaques in transgenic mice. Science 1996;274(5284):99-102.
34. Kluver H, Barrera E. A method for the combined staining of cells and fibers in the nervous system. J Neuropathol Exp Neurol 1953;12(4):400-403.
35. Braakman N, Matysik J, van Duinen SG, Verbeek F, Schliebs R, de Groot HJ, Alia A. Longitudinal assessment of Alzheimer's beta-amyloid plaque development in transgenic mice monitored by in vivo magnetic resonance microimaging. J Magn Reson Imaging 2006;24(3):530-536.
36. Kara F, Chen F, Ronen I, de Groot HJ, Matysik J, Alia A. In vivo measurement of transverse relaxation time in the mouse brain at 17.6 T. Magnetic resonance in medicine : official journal of the Society of Magnetic Resonance in Medicine / Society of Magnetic Resonance in Medicine 2012.
37. Carr HY, Purcell EM. Effects of Diffusion on Free Precession in Nuclear Magnetic Resonance Experiments. Phys Rev 1954;94(3):630-638.
38. Meiboom S, Gill D. Modified Spin-Echo Method for Measuring Nuclear Relaxation Times. Rev Sci Instrum 1958;29(8):688-691.
39. Hennig J, Nauerth A, Friedburg H. RARE imaging: a fast imaging method for clinical MR. Magn Reson Med 1986;3(6):823-833.
40. Muller R, Buttner P. A critical discussion of intraclass correlation coefficients. Stat Med 1994;13(23-24):2465-2476.
41. Bartzokis G, Mintz J, Marx P, Osborn D, Gutkind D, Chiang F, Phelan CK, Marder SR. Reliability of in vivo volume measures of hippocampus and other brain structures using MRI. Magn Reson Imaging 1993;11(7):993-1006.
42. Meguro K, Constans JM, Shimada M, Yamaguchi S, Ishizaki J, Ishii H, Yamadori A, Sekita Y. Corpus callosum atrophy, white matter lesions, and frontal executive dysfunction in normal aging and Alzheimer's disease. A community-based study: the Tajiri Project. International psychogeriatrics / IPA 2003;15(1):9-25.

43. Harms MP, Kotyk JJ, Merchant KM. Evaluation of white matter integrity in ex vivo brains of amyloid plaque-bearing APPsw transgenic mice using magnetic resonance diffusion tensor imaging. Exp Neurol 2006;199(2):408-415.
44. Song SK, Kim JH, Lin SJ, Brendza RP, Holtzman DM. Diffusion tensor imaging detects age-dependent white matter changes in a transgenic mouse model with amyloid deposition. Neurobiol Dis 2004;15(3):640-647.
45. Duan JH, Wang HQ, Xu J, Lin X, Chen SQ, Kang Z, Yao ZB. White matter damage of patients with Alzheimer's disease correlated with the decreased cognitive function. Surgical and radiologic anatomy : SRA 2006;28(2):150-156.
46. Naggara O, Oppenheim C, Rieu D, Raoux N, Rodrigo S, Dalla Barba G, Meder JF. Diffusion tensor imaging in early Alzheimer's disease. Psychiatry Res 2006;146(3):243-249.
47. Braakman N, Matysik J, van Duinen SG, Verbeek F, Schliebs R, de Groot HJ, Alia A. Longitudinal assessment of Alzheimer's beta-amyloid plaque development in transgenic mice monitored by in vivo magnetic resonance microimaging. Journal of magnetic resonance imaging : JMRI 2006;24(3):530-536.
48. Ono J, Kodaka R, Imai K, Itagaki Y, Tanaka J, Inui K, Nagai T, Sakurai K, Harada K, Okada S. Evaluation of myelination by means of the T2 value on magnetic resonance imaging. Brain & development 1993;15(6):433-438.
49. Laule C, Leung E, Lis DK, Traboulsee AL, Paty DW, MacKay AL, Moore GR. Myelin water imaging in multiple sclerosis: quantitative correlations with histopathology. Multiple sclerosis 2006;12(6):747-753.
50. Bouilleret V, Nehlig A, Marescaux C, Namer IJ. Magnetic resonance imaging follow-up of progressive hippocampal changes in a mouse model of mesial temporal lobe epilepsy. Epilepsia 2000;41(6):642-650.
51. Heinz R, Ferris N, Lee EK, Radtke R, Crain B, Hoffman JM, Hanson M, Paine S, Friedman A. MR and positron emission tomography in the diagnosis of surgically correctable temporal lobe epilepsy. AJNR Am J Neuroradiol 1994;15(7):1341-1348.
52. Mitew S, Kirkcaldie MT, Halliday GM, Shepherd CE, Vickers JC, Dickson TC. Focal demyelination in Alzheimer's disease and transgenic mouse models. Acta Neuropathol 2010;119(5):567-577.

53. Xu J, Chen S, Ahmed SH, Chen H, Ku G, Goldberg MP, Hsu CY. Amyloid-beta peptides are cytotoxic to oligodendrocytes. J Neurosci 2001;21(1):RC118.
54. Haynes RL, Folkerth RD, Keefe RJ, Sung I, Swzeda LI, Rosenberg PA, Volpe JJ, Kinney HC. Nitrosative and oxidative injury to premyelinating oligodendrocytes in periventricular leukomalacia. J Neuropathol Exp Neurol 2003;62(5):441-450.
55. Zeng C, Lee JT, Chen H, Chen S, Hsu CY, Xu J. Amyloid-beta peptide enhances tumor necrosis factor-alpha-induced iNOS through neutral sphingomyelinase/ceramide pathway in oligodendrocytes. J Neurochem 2005;94(3):703-712.
56. Desai MK, Sudol KL, Janelsins MC, Mastrangelo MA, Frazer ME, Bowers WJ. Triple-transgenic Alzheimer's disease mice exhibit region-specific abnormalities in brain myelination patterns prior to appearance of amyloid and tau pathology. Glia 2009;57(1):54-65.
57. Jantaratnotai N, Ryu JK, Kim SU, McLarnon JG. Amyloid beta peptide-induced corpus callosum damage and glial activation in vivo. Neuroreport 2003;14(11):1429-1433.
58. Rossner S, Apelt J, Schliebs R, Perez-Polo JR, Bigl V. Neuronal and glial beta-secretase (BACE) protein expression in transgenic Tg2576 mice with amyloid plaque pathology. J Neurosci Res 2001;64(5):437-446.
59. Apelt J, Schliebs R. Beta-amyloid-induced glial expression of both pro- and anti-inflammatory cytokines in cerebral cortex of aged transgenic Tg2576 mice with Alzheimer plaque pathology. Brain research 2001;894(1):21-30.
60. Sasaki A, Shoji M, Harigaya Y, Kawarabayashi T, Ikeda M, Naito M, Matsubara E, Abe K, Nakazato Y. Amyloid cored plaques in Tg2576 transgenic mice are characterized by giant plaques, slightly activated microglia, and the lack of paired helical filament-typed, dystrophic neurites. Virchows Arch 2002;441(4):358-367.
61. Itagaki S, McGeer PL, Akiyama H, Zhu S, Selkoe D. Relationship of microglia and astrocytes to amyloid deposits of Alzheimer disease. J Neuroimmunol 1989;24(3):173-182.
62. Mackenzie IR, Hao C, Munoz DG. Role of microglia in senile plaque formation. Neurobiol Aging 1995;16(5):797-804.
63. D'Andrea MR, Cole GM, Ard MD. The microglial phagocytic role with specific plaque types in the Alzheimer disease brain. Neurobiol Aging 2004;25(5):675-683.

64. Schwab C, McGeer PL. Inflammatory aspects of Alzheimer disease and other neurodegenerative disorders. J Alzheimers Dis 2008;13(4):359-369.
65. Mori T, Koyama N, Arendash GW, Horikoshi-Sakuraba Y, Tan J, Town T. Overexpression of human S100B exacerbates cerebral amyloidosis and gliosis in the Tg2576 mouse model of Alzheimer's disease. Glia 2010;58(3):300-314.
66. Smith KJ, Kapoor R, Felts PA. Demyelination: the role of reactive oxygen and nitrogen species. Brain Pathol 1999;9(1):69-92.
67. Laakso MP, Partanen K, Soininen H, Lehtovirta M, Hallikainen M, Hanninen T, Helkala EL, Vainio P, Riekkinen PJ, Sr. MR T2 relaxometry in Alzheimer's disease and age-associated memory impairment. Neurobiol Aging 1996;17(4):535-540.
68. Schenck JF, Zimmerman EA, Li Z, Adak S, Saha A, Tandon R, Fish KM, Belden C, Gillen RW, Barba A, Henderson DL, Neil W, O'Keefe T. High-field magnetic resonance imaging of brain iron in Alzheimer disease. Top Magn Reson Imaging 2006;17(1):41-50.
69. Nakahara M, Hayashi H, Kumazaki T, Mori O. Value of magnetization transfer contrast as a sensitive technique to reflect histopathological changes in the white matter adjacent to the frontal horns of lateral ventricles. Nihon Ika Daigaku zasshi 1999;66(4):245-252.
70. Cotrina ML, Nedergaard M. Brain connexins in demyelinating diseases: therapeutic potential of glial targets. Brain Res 2012;1487:61-68.
71. Yang W, Wu Q, Yuan C, Gao J, Xiao M, Gu M, Ding J, Hu G. Aquaporin-4 mediates astrocyte response to beta-amyloid. Molecular and cellular neurosciences 2012;49(4):406-414.
72. Shin J, Yu SB, Yu UY, Jo SA, Ahn JH. Swedish mutation within amyloid precursor protein modulates global gene expression towards the pathogenesis of Alzheimer's disease. BMB reports 2010;43(10):704-709.
73. Gunnarson E, Axehult G, Baturina G, Zelenin S, Zelenina M, Aperia A. Lead induces increased water permeability in astrocytes expressing aquaporin 4. Neuroscience 2005;136(1):105-114.

4 *In vivo* Measurement of Transverse Relaxation Times in the Mouse Brain at 17.6 T*

4.1 Abstract

The goal of this study is to establish the regional T_1 and T_2 values of the healthy mouse brain at ultra high magnetic field strength of 17.6 T and to follow regional brain T_1 and T_2 changes with age. *In vivo* T_1 and T_2 values in several anatomical regions of the mouse brain: the hippocampus, cortex, thalamus, hypothalamus, corpus collosum, caudate putamen were measured. A field-dependent decrease in T_2 is shown and validated with phantom measurements. T_2 values at 17.6T typically increased with age in multiple brain regions except in the hypothalamus and the caudate-putamen, where a slight decrease was observed. Furthermore, T_1 values in various brain regions of young and old mice are presented at 17.6T. A large gain in signal-to-noise ratio was observed at 17.6T. This study establishes for the first time the normative T_1 and T_2 values at 17.6T over different mouse brain regions with age. The estimates of *in vivo* T_1 and T_2 will be useful to optimize pulse sequences for optimal image contrast at 17.6T and will serve as baseline values against which disease related relaxation changes can be assessed in mice.

4.2 Introduction

Transverse and longitudinal relaxation times play an important role in optimizing MRI parameters such as contrast level or signal-to-noise ratio, and provide a quantitative indicator of tissue changes induced by various pathological conditions (1,2). The changes in T_2 values of the brain tissue are widely used as a surrogate marker in the evaluation of various brain disorders (3,4). The *in vivo* T_2 of brain tissue is related to the local water environment and the free-to-bound water ratio, which may change in response to cellular and axonal loss or membrane breakdown (5-8). For example, the process of breakdown of myelin in certain types of neurodegenerative disorders such as MS and AD, leads to alterations in the local water environment that increase the ratio of the free-to-bound water in tissue and thus increases T_2 and T_1 of white matter (5,9,10). The T_2 and T_1 also change in brain regions where brain iron is deposited in the form of ferritin and

*This chapter was published in Magn Reson Med, 2012 doi: 10.1002/mrm.24533.

hemosiderin (11). In addition both T_1 and T_2 values provide quantitative information about tissue changes in the healthy brain during aging (12,13).

Mice are routinely used as models for studying human brain disorder. Due to the small size of the mouse brain, the present trend in *in vivo* mouse brain MRI is to move toward ultra-high magnetic field (≥ 7 T) for improved SNR, higher resolution, sensitivity and specificity (14-18). Thus, ultra-high magnetic field systems, such as 17.6 T, can serve as a powerful tool to detect more subtle abnormalities in anatomical and functional characteristics of emerging mouse models of neurodegenerative diseases (19). While the values for T_2 relaxation time in different parts of the mouse brain have been published in different field strengths (2,12,20-23), there is no systematic assessment of the regional T_2 values for the healthy mouse brain at 17.6 T. The values of T_1 relaxation time of various mouse brain regions have been reported at 17.6 T in young mice (18). However, age-dependent changes in T_1 have not been analyzed at this magnetic field strength. The C57BL/6J mouse is one of the most widely used inbred strains and the first to have its genome sequenced (24). It is generally used as a background strain for the generation of transgenic models of various brain diseases such as AD (19). In this study, we aimed to establish the values of regional T_2 relaxation time for healthy C57BL/6J mouse brain *in vivo* at 17.6 T and to determine magnetic field dependent changes in T_2. Phantom solutions were used to validate changes in T_2 at different field strengths and to explore the validity of MSME sequence to measure T_2. In addition we assessed age-related regional T_2 and T_1 changes in the mouse brain at 17.6 T. These estimates of *in vivo* T_2 and T_1 relaxation of the mouse brain will be useful to optimize MRI sequences for optimal image contrast and sensitivity in the mouse brain at 17.6 T. In addition, knowledge of age-related T_2 and T_1 changes in the healthy mouse brain is mandatory if disease-related deviations in T_2 and T_1 have to be studied in longitudinal studies.

4.3 Materials and Methods

4.3.1 Phantoms

Phantom solutions containing different concentrations of Gadolinium-tetra-azacyclo-dodecane-tetra-acetic acid (Gd-DOTA) (Dotarem; Guerbet Nederland BV, Gorinchem, the Netherlands) were prepared by diluting a stock solution of GD-DOTA (0.5 M) in phosphate buffer saline (pH=7.50). Dilution factors used for T_2 measurements were 1/50 (i.e., 10 mmol Gd-DOTA/L), 1/100, 1/200, 1/400, 1/800). The same phantoms were used

for both MRI and NMR experiments. For the SNR analysis, a phantom solution consisting of 20% H2O, 80% D2O, 1g/l $CuSO_4$ was prepared.

4.3.2 High-resolution NMR

High-resolution NMR experiments were performed at 2.35 T, 9.4 T, and 17.6 T using a broadband 5-mm solution-state NMR probe. Radiation damping was minimized by using a restricted sample volume (capillary NMR tubes) in low-Q probes. The pulse sequence used for T_2 measurements was based on the CPMG scheme. The pulse lengths of 90º and 180º at all fields were 9.6 and 19.2 μs, respectively. A variable list of 16 duration times between 90º and 180º pulse was adopted. Both the recycle delay and the longest duration time were kept at larger than 10 times of the expected T_2 of each sample.

4.3.3 Mice

For all *in vivo* measurements female C57BL/6J mice were used. All of the animal experiments were approved by the institutional animal care and animal use committee of the University of Leiden in accordance with the NIH Guide for the Care and Use of Laboratory Animals.

4.3.4 MRI

All MRI measurements were performed using 400 MHz (9.4 T) and 750 MHz (17.6 T) vertical 89-mm bore magnets equipped with a 1 Tm^{-1} actively shielded imaging gradient insert (Bruker, Germany). A birdcage RF coil with an inner diameter of 2 cm was used for excitation and detection. The system was interfaced to a Linux PC running Topspin 2.0 and ParaVision 5.0 software (Bruker Biospin GmbH, Germany).

All *in vivo* MRI studies were conducted as previously described (25). Before imaging, the mice were initially anesthetized with 2% isoflurane (Forane, Abott, UK), in air (0.3 l/min) and oxygen (0.3 l/min). During scanning the level of anesthetic was maintained between 1 and 1.5% to keep the breathing of the animal at a constant rate of ~50 breaths per minute. Animals were placed in the 20 mm birdcage RF coil with a special mouse head mask, which was used to administer the anaesthetic gas during the MR experiments. A respiration sensor, connected to a respiration unit, was placed on the abdomen to monitor the respiration rate. The respiration unit was connected to a computer running Bio-SAM respiration monitoring software (Bruker Biospin, Germany). During MRI imaging, the respiration rate of the mouse was constantly monitored and the body temperature of the mouse was kept constant by pumping warm water (30±1°C) through the gradient system. The rectal body temperature of the mouse during scanning was

measured to be 30±1°C. T_2 measurements in phantom solutions were also conducted at 30±1°C and were repeated at least 4 times.

T_2 values were measured with the MSME sequence that is based on the CPMG sequence, where transverse magnetization of a 90º pulse is refocused by a train of 180º pulses generating a series of echoes (26,27). The following imaging parameters were used for the phantom and *in vivo* experiments both at 9.4 T and 17.6 T: NA = 2; NS = 1 and/or 10 with a slice thickness of 1.0 mm and an interslice thickness of 1.5 mm; Number of echoes = 16 with echo spacing = 8.5; A TR = 3 s with an effective spectral bandwidth = 50 kHz; FOV = 2.0 x 2.0 cm; Matrix size= 256 x 256; This yields an effective in-plane resolution of 0.078 x 0.078 mm and a voxel resolution of 6.10 x 10^{-3} mm^3. The total acquisition time for the experiment was 19 min 12 s. To study the dependence of T_2 on the CPMG refocusing interpulse interval, the T_2 measurements were performed using the MSME sequence with 16 echo and 4 different refocusing interpulse intervals, namely 5.6, 8.5, 10, and 18 ms. The last 5 echo of 8.5 ms acquisition, the last 7 echo of 10 ms acquisition and the last 10 echo of 18 ms acquisition were discarded to provide comparable temporal sampling windows (namely, 5.6-91.04 ms, 8.5-93.50 ms, 10-90 ms, 18-90 ms acquisitions, respectively). For the precise localization of ROIs on the brain regions for T_2 measurements, a pilot scan of a mouse brain was acquired with multi-slice rapid acquisition using the RARE sequence (28) and subsequently ROIs were transferred to T_2 maps to ensure precise regional placement. The following imaging parameters were used for the RARE sequence: TE = 11.67 ms (at 9.4 T) and 8.5 ms (at 17.6 T); TR = 1500 ms (at 9.4 T) and 2000 ms (at 17.6 T); NA = 1, rare factor = 6; NS = 10, with slice thickness 1.0 mm; interslice thickness = 1.5 mm. To establish the test–retest reliability of T_2 measurements, the same mice (n= 7) were scanned twice with an interval of 4 days and the phantom solution (10 mM) was scanned twice with an interval of six weeks. For the measurement of the SNR in the phantom solution, the mic-MSME sequence (Bruker, Paravision 5) was used. The following imaging parameters were applied both at 9.4 T and 17.6 T: TE= 7 ms, RT = 1000 ms, NA = 1, FOV = 6.0 x 6.0, matrix = 256 x256, slice thickness = 1mm, NS = 11.

T_1 was measured with a multiple spin echo saturation recovery method with variable repetition time (RAREVTR). Slice excitation and refocusing were accomplished by hermite pulses, resulting in 90° and 180° pulse lengths of 1.4 and 0.9 ms, respectively. The following imaging parameters were used at 17.6 T: TE = 5.5 ms; TR-array = 0.1, 0.18, 0.36, 0.6, 0.8, 1.0, 1.5, 2.0, 4.0, 6.0, 10.0 and 15.0 s; Matrix size= 128 x 128; FOV

= 1.7 x 1.7 cm; slice thickness = 0.9 mm. The total acquisition time for the experiment was 33 min 13 s. All images acquired single slices to prevent interslice modulation effects. The slice was positioned as described previously (18). To minimize the contribution of partial volume effects from cerebrospinal fluid, the ROIs were checked carefully on images collected with very thin slices (0.25 mm) using the same RAREVTR sequence with following parameters: RT = 6000 ms; TE = 17 ms; FOV = 1.5 x 1.5 cm; Matrix size = 256 x 256; NS = 10.

For the comparison of the SNR for *in vivo* imaging at two different magnetic field strength (9.4 T and 17.6 T), the experiment was performed with the RAREVTR sequence using three different TR (6, 10 and 15 s) and TE (5.5, 16.5 and 27.5 ms). The following imaging parameters were used: NA = 1; TR-array = 15000, 10000, 6000; TE = 5.5, 16.5, 27.4 ms; FOV = 1.7 x 1.7 cm; Matrix size= 128 x 128; slice thickness = 0.6 mm; Effective spectral bandwidth = 71428 kHz. The same mouse was used for SNR measurements at 9.4 T and 17.6 T.

4.3.5 Data Processing

4.3.5.1 Estimation of T_2 and T_1

To calculate T_2, ROIs were drawn on the images by using an image sequence analysis (ISA) tool package (Paravision 5, Bruker), which uses a fit function [$y= A+C*\exp(-t/T_2)$], where A stands for the absolute bias, C is the signal intensity, and T_2 represents the transverse relaxation time as defined earlier. The T_1 values were determined by ISA using a fit function: $M(t) = A + M_0 * (1 - \exp(t/T_1)$, where M_0 is the equilibrium magnetization. ROIs were manually defined for the hippocampus, cortex, thalamus, hypothalamus, corpus callosum, caudate-putamen, olfactory bulb and its glomerular layer and muscle using the Allen Brain Atlas with the brain explorer program (http://mouse.brain-map.org) for referencing. For all animals, the T_2 and T_1 were the mean of the ROIs drawn on the right and left sides of the brain, except for the corpus callosum region. For phantoms, a cylinder was drawn on the inside of the axial figures of the tubes. The transverse relaxation rate (R_2) was obtained from the equation: $R_2 = 1/T_2$ (s^{-1}). Relaxivity of the contrast agent is defined as the efficiency by which an MRI contrast agent can accelerate the proton relaxation rate in a homogeneous medium (29). Relaxivity was calculated as the slope of the linear regression line of a plot of R_2 *vs* concentration of MRI contrast agent (30).

4.3.5.2 Estimation of SNR

The SNR in the images is measured as the average signal intensity over the ROI divided by the standard deviation of the noise.

4.3.5.3 Statistics

A paired and/or two-tailed student's t-test was used to compare mean values. Statistical significance was assigned for values of $P < 0.05$. The reliability of the measurements was assessed by computing the ICC2,1 using a 2-way random effects ANOVA model and the absolute agreement definition (31,32). The associations between test-retest data were analyzed by the Pearson's correlation coefficient (r) at a 0.05 significance level. An ICC close to 1 indicates excellent reliability. The Pearson's r close to 1 indicates excellent association (31).

4.4 Results

4.4.1 Phantom studies

Fig. 4.1a depicts the quantitative relaxivity of Gd-DOTA phantom solutions at 17.6 T using MRI and high-resolution NMR methods. The MSME and the single-slice multi-echo MRI methods showed 11% and 8% lower r_2 values, respectively, relative to the value acquired with the NMR method. Fig. 4.1b shows the r_2 of Gd-DOTA phantom solutions determined at 2.35 T, 9.4 T, and 17.6 T using the high-resolution NMR method. As is clear from this figure, plots of the transverse relaxation rate, R_2 ($1/T_2$), vs. the Gd-DOTA concentrations (mM) reveal a linear dependence of the R_2 on the concentration. In addition, the r_2 values increased with increasing field strength. The value of r_2 at 17.6 T is ~18% and at 9.4 T ~11% higher relative to the value at 2.35 T. These results clearly show that T_2 relaxation times of Gd-DOTA decrease with increasing field strength. To confirm that the 180° pulses in the MSME sequence did not introduce spurious magnetization from stimulated echoes or from signals originating from outside the selected slices, T_2 decay curves from a Gd-DOTA phantom with echo spacings of 8.5, 13, 15, and 17 ms were acquired. An example of a T_2 decay curve with an 8.5 echo spacing is depicted in Fig. 4.1S a (supplementary). The differences among T_2 values acquired using the various echo spacings were statistically insignificant. In order to observe the variation of the T_2 between the 10 slices used in the multi-echo sequence, the T_2 of the phantom (10 mM) was measured for each slice. No statistically significant variation in T_2 values was observed between the slices ($P > 0.05$) (Fig. 4.1S b). To assess the test-retest reliability of

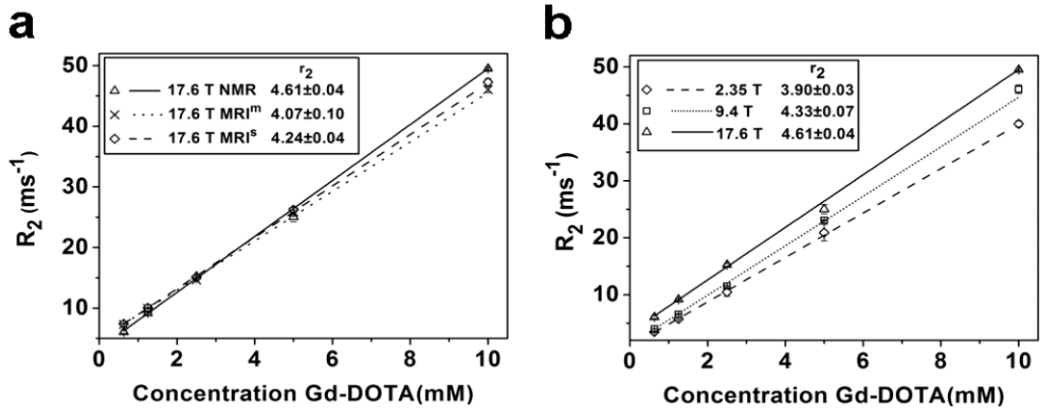

Fig. 4.1. (a) Scatter plots showing the changes in relaxation rates (R_2) as a function of the Gd-DOTA concentration measured using MRI and NMR at 17.6 T; (b) Scatter plots showing the changes in R_2 as a function of magnetic field strength (2.35 T, 9.4 T and 17.6 T) measured using NMR. Mean R_2 in s^{-1} ± error bars (SE). The slopes of the weighted linear regression curves are the T_2 relaxivities (r_2). r_2 in $mM^{-1}\ s^{-1}$ ± SE; MRI^m, multi-slice multi-echo MRI; MRI^S, single-slice multi-echo MRI. The correlation coefficient (Pearson's r) of the linear fitting for all lines is 0.99.

the Gd-DOTA phantom, T_2 data were acquired at 17.6 T using the MSME sequence at two different time points, separated by an interval of 46 days. The differences in mean T_2 values between two sessions were statistically insignificant, with $P > 0.05$. The intra-class correlation coefficient and Pearson's r values were measured as $r = 0.92$ and $r = 0.97$, respectively, suggesting superior test-rest reliability ($P < 0.05$ in all cases) and minimum instrumental variations. The SNR performance at both magnetic field strengths was compared and was found to increase by a factor of 1.5 at 17.6 T as compared to 9.4 T.

4.4.2 *In vivo* studies

Fig. 4.2a shows ROIs that were selected on a representative series of RARE images from a normal mouse to acquire T_2. Fig. 4.2b depicts a graphical summary of the *in vivo* T_2 relaxation times for the mouse brain, at 9.4 T and at 17.6 T. A clear decrease in T_2 values was observed in various brain regions at 17.6 T as compared to 9.4 T. However, the T_2 in the muscle showed a relatively small decrease at 17.6 T as compared to 9.4 T. At both magnetic field strengths, the T_2 were longest for the olfactory bulb and the grill regions, whereas the thalamus, the corpus callosum consistently show a shorter T_2 compared to other brain regions. Table 4.1 depicts the quantitative summary of the *in vivo* T_2 of the

mouse brain at 9.4 T and at 17.6 T. To validate the *in vivo* T_2 dataset that was acquired using a multi-slice mode, the measurement was repeated in the single-slice mode. The T_2 values measured using the multi-slice mode were slightly higher than those from the single-slice mode (Fig. 4.2S); however, the systematic overestimation was less than 3 ms. The SNR for the cortex region of the mouse brain at both magnetic field strengths were compared and the SNR was found to increase by a factor of 1.6 at 17.6 T as compared to 9.4 T. The dependence of cortex and corpus callosum T_2 on the CPMG refocusing interpulse interval was investigated at 17.6 T (Fig. 4.3S). No statistically significant effect of the interpulse interval in the range of interest (between 5.6 and 18 ms) was observed on the T_2 of cortex and corpus callosum.

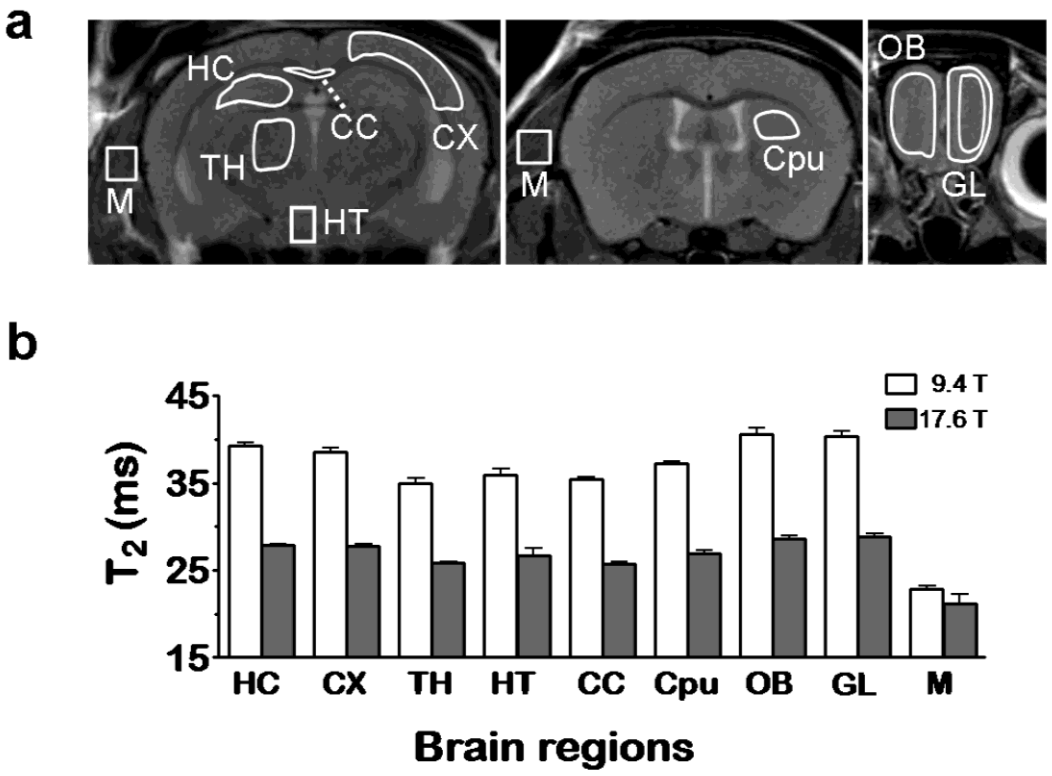

Fig. 4.2. (a) MR coronal slices of a mouse brain, showing relevant ROIs, acquired with the RARE sequence at 17.6 T; (b) In vivo T_2 relaxation times of different mouse brain regions acquired at 9.4 T and 17.6 T. The analyzed brain structures include the hippocampus (HC), cortex (CX), thalamus (TH), hypothalamus (HT), corpus callosum (CC), caudate-putamen (Cpu), olfactory bulb (OB), glomerular layer (GL) of OB; Muscle (M, internal reference). Values are expressed as mean T_2 in ms ± SE (error bars). Two-tail student t test, $P < 0.05$ in all regions; n=5.

Table 4.2 shows test-retest reliability results of *in vivo* T_2 measurements in multiple brain regions. The ICCs were statistically significant ($P < 0.05$) for all regions. The test-retest reliability was very good for cortex, thalamus, corpus callosum, caudate-putamen as well as muscle tissue, with the ICC ranging between 0.84 and 0.92. For hippocampus, and hypothalamus, ICC was 0.64 and 0.53, respectively. Table 2 also presents Pearson's *r*, which showed superior association for all regions between two sessions. For all the brain regions Pearson's *r* was statistically significant ($P < 0.05$). However, Pearson's *r* for HT regions was somewhat less than for the other regions ($P = 0.062$). The systematic error was checked by a paired t-test and results are
shown in Table 4.2.

Fig. 4.3 summarizes the age-related changes of the T_2 for the mouse brain at 17.6 T. The *in vivo* T_2 increases with age for multiple brain regions except for the hypothalamus and the caudate-putamen, where a slight decrease in T_2 was observed. A significant increase in T_2 was observed in the cortex region in 13.6 and 15.1 months old mice as compared to 3.6 months old mice (Table 4.3).

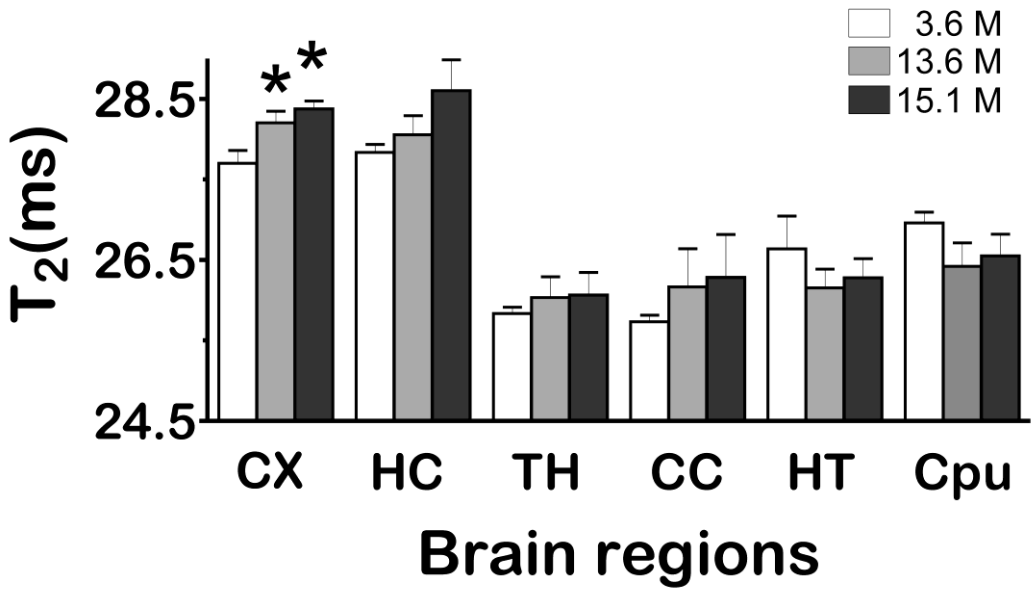

*Fig. 4.3. Variation of in vivo T_2 relaxation times of the mouse brain with age for the datasets measured in a magnetic field of 17.6 T. The analyzed brain structures include the hippocampus (HC), cortex (CX), thalamus (TH), hypothalamus (HT), corpus callosum (CC) and caudate-putamen (Cpu). Values are expressed as mean T_2 in ms ± SE (error bars); n=5. Paired t test, *P < 0.05, significant from T_2 at 3.6 month (M). Same mice were scanned at the age of 3.6, 13.6 and 15.1 months.*

Table 4.4 depicts the T_1 values in multiple mouse brain regions in young (3 months old) and old (23 months old) mice at 17.6 T. Slightly shorter T_1 in the corpus callosum and the caudate-putamen and slightly longer T_1 in thalamus regions were observed in old mice as compared to young mice.

4.5 Discussion

4.5.1 Phantom studies

The r_2 acquired with the MSME sequence was in very close agreement with the values obtained using high-resolution NMR methods and the r_2 derived from the data collected with the single-slice multi-echo sequence. The results validate the accuracy of the T_2 extracted from the data acquired with the MSME sequence at 17.6 T. In addition, phantom experiments showed that r_2 decreases with increasing magnetic field strength. The apparent decrease of the T_2 with increasing field strength is incompatible with straightforward BPP model dipolar relaxation processes that would lead to a T_2 that is independent of the field strength (14,33). A decrease of the T_2 with increasing field strength can be attributed to increasing microscopic susceptibility gradients, causing irreversible dephasing due to diffusion across those gradients (34-36). The MSME method used in this study to acquire T_2 data is time-effective, since the sequence allows for imaging of several slices in a single scan (37,38).

Previous studies, however, have reported that many factors, such as spurious echoes, can influence the ability to obtain accurate T_2 data using the MSME method (37-42). Moreover, there are additional concerns regarding the effect of higher magnetic field strength including: magnetic field inhomogeneity, increased stimulated echo artifacts, and increased power deposition (43). We have demonstrated that spurious magnetization contribution from stimulated echoes in the 180° pulses in the MSME sequence is negligible, since the estimated T_2 values for the phantom did not change significantly for echo spacings of 8.5, 13, 15, and 17 ms. Also a spatially uniform T_2 was observed throughout the 10 slices suggesting that the performance of the 180° refocusing trains was spatially uniform for the MSME sequence (Fig. 4.1S b). In addition, excellent test-retest T_2 reliability was measured by the MSME sequence. These results suggested very little contamination of T_2 via spurious echoes and the instrumental variation at 17.6 T.

A better SNR was observed for the phantom and the mouse brain at 17.6 T as compared to 9.4 T. If the relaxation parameters are ignored, the SNR is expected to increase linearly with magnetic field strength (14). The SNR has been reported to be proportional to magnetic field strength (B_0) and the square root of (T_2 /T_1) in a fully relaxed pulse [SNR $\propto B_0 \sqrt{T_2/T_1}$] (14). The lower-than-predicted increase in SNR at 17.6 T could be related with many factors such as changes in relaxation times (shorter T_2 and longer T_1), increased susceptibility effects, and larger field inhomogeneity (44,45). All these factors can limit the SNR increment at higher fields. In addition, it has been reported that experimental conditions such as RF coils, pulse sequences and preamplifiers also affect the SNR quantification (46).

4.5.2 *In vivo* studies

In this study, the *in vivo* T_2 for several regions of the healthy mouse brain have been presented at 17.6 T. While the T_2 in different parts of the transgenic and non-transgenic mouse brain have been published for different field strengths (2,12,20-23), and T_2 maps of the ischemic mouse brain were provided at 17.6 T, a systematic assessment of the T_2 for the healthy mouse at 17.6 T was not yet obtained. Our results at 17.6 T are well in line with data from healthy rat brain acquired at 16.4 T (47). In addition, the *in vivo* T_2 of the mouse brain determined at 9.4 T in this study reproduces well with earlier published data (2,12,20,22). In particular, the T_2 values of the corpus callosum, hippocampus and

Table 4.3: *In Vivo* T_2 Values of the Mouse Brain with Age at 17.6 T[a]

	Age (Month)		
Structure	3.6	13.6	15.1
HC	27.84 ± 0.10	28.06 ± 0.24	28.60 ± 0.38
CX	27.70 ± 0.16	28.20 ± 0.15*	28.38 ± 0.10*
TH	25.83 ± 0.08	26.03 ± 0.26	26.06 ± 0.28
HT	26.64 ± 0.41	26.15 ± 0.23	26.28 ± 0.23
CC	25.73 ± 0.08	26.17 ± 0,48	26.28 ± 0.53
Cpu	26.96 ± 0.13	26.42 ± 0.29	26.55 ± 0.27
M	21.25 ± 0.44	21.53 ± 0.31	21.23 ± 0.16

[a]Values are expressed as mean relaxation times (ms ± SE), kn = 5. HC = Hippocampus, CX = Cortex, TH = Thalamus, HT = Hypothalamus, CC = Corpus callosum, Cpu= Caudate-putamen, M = Muscle. Paired two-tailed t-test,* $P < 0.05$ compared to mice at the age of 3.6 month.

caudate-putamen are in excellent agreement with earlier reports at 9.4 T (20). Our results also illustrate for various brain regions that the T_2 decreases with increasing magnetic field strength. While this is consistent with earlier reports (14,36,43,48,49), the extent of T_2 reduction was found to depend on the composition of the tissue. The T_2 of the muscle tissue did not show a strong field dependence, which could be attributed to a lower intracellular molecular mobility of the water in the muscle tissue than for the brain tissue. The decrease of tissue T_2 with increasing magnetic field strength has been explained in terms of the molecular processes of diffusion and/or chemical exchange of spins between regions with different magnetic field strengths (34,36,50,51). Magnetic field inhomogeneities increase linearly with increasing magnetic field strength, and are created by local susceptibility gradients, which can be microscopic (*e.g.*, surrounding blood vessels) as well as macroscopic (*e.g.*, around the sinuses and petrous bone) (34). Diffusion across these magnetic field gradients dephases the transverse magnetization of the water protons, resulting in an overall decrease of the T_2. The magnitude of these gradients increases with field strength and therefore their effect on T_2 increases with the magnetic field strength (14). This process is referred to as dynamic dephasing and it depends, among other things, on the refocusing interpulse interval τ, defined as half the interval between successive 180° pulses in a CPMG sequence (36,52). It has been shown, in theory and experiments, that T_2 decreases with increasing τ (36,52-54). Several works have investigated the effect of varying τ on T_2 measurements in biological tissues (51,52,54-56). In our experiments, in order to obtain an estimate of the effect that the refocusing interpulse interval has on T_2, we repeated the T_2 measurements with 4 different τ values, between 5.6 ms to 18 ms (supplementary Fig. 4.3S). No statistically significant dependence of the T_2 on the interpulse interval was observed. This result suggests that the changes observed in T_2 values with age depend more on changes in tissue properties in the individual brain structures rather than magnetic field disturbances. In our study, a relatively short refocusing interpulse interval (8.5 ms) was used. However even in these conditions, contribution of diffusion and/or chemical exchange on T_2 is inevitable. In practice, most studies are performed with τ values no shorter than those used here, and thus for optimization of contrast and general clinical applications, the T_2 values represented here are expected to be valid and reproducible under similar experimental conditions across platforms. In our study, age-dependent changes in T_2 in multiple brain regions, including the cortex, hippocampus, thalamus and corpus callosum, was observed at 17.6 T (Fig. 4.3; Table 3.3). In particular, for the cortex the T_2 relaxation time shows a significant increase with age. These results are in good agreement with a

Table 4.4: *In vivo* T_1 values of the mouse brain at 17.6 T[a]

Tissue	Young	Old
HC	2.14 ± 0.04	2.16 ± 0.03
CX	2.02 ± 0.05	2.07 ± 0.04
TH	2.05 ± 0.06	2.17 ± 0.08*
CC	1.99 ± 0.05	1.92 ± 0.05*
Cpu	2.01 ± 0.03	1.96 ± 0.04*
OB	1.97 ± 0.03	1.96 ± 0.04
M	2.39 ± 0.07	2.37 ± 0.03

[a]Mean T_1 relaxation times of young (3 months) and old (23 months) mice (s ± SD), n=5. HC = Hippocampus, CX = Cortex, TH = Thalamus, CC = Corpus callosum, Cpu= Caudate-putamen, OB = Olfactory Bulb, M = Muscle. Two-tailed t-test: *$P < 0.05$ compared to young mice.

recently published age-dependent T_2 measurement in human brain at 3 T (13). T_2 values of the brain tissue can increase with age in response to cellular and axonal loss or membrane breakdown (5,57,58). These aging processes reduce the number of macromolecules and increase free water content. This raises the ratio of free-to-bound water protons and as a result contributes to the increase in T_2 values (13). The lower T_2 values in the younger mice as compared to the older mice might also be caused by the increased susceptibility effects at 17.6 T. The higher susceptibility effects in the younger mice due to a very high ratio of air space to brain tissue may reduce T_2 values, especially at higher fields (17.6T). Nevertheless, T_2, acquired in this study using a short interpulse interval τ = 8.5 ms, is in the plateau region and seems to be less sensitive to magnetic disturbances induced by local magnetic susceptibility effects. This would also indicate that the changes observed in T_2 values with age in our study depend on tissue cellularity changes, rather than magnetic disturbances. A few mouse brain regions, such as the hypothalamus and the caudate-putamen, show a slight decrease in T_2 values with age, which could result from increased deposition of paramagnetic substances such as ferritin and hemosiderin (11,59). In human, basal ganglia *e.g.* caudate-putamen structures show increased levels of paramagnetic substances with age (13). Falangola *et al.* (22) did not observe any age-dependency of T_2 in normal mouse brain at 7 T. The differences in the findings can be explained by the ROI definition, use of different imaging parameters, susceptibility effects and the field strength. Specially, the ROI employed in our study covers only the somatosensory and the retrosplenial granular cortex regions. However in

the study of Falangola *et al.*, the ROI covers a bigger volume, *i.e*., the ectorhinal, perirhinal, piriform, somatosensory and retrosplenial granular cortex regions.

It is known that technical challenges such as increased RF field inhomogeneity, increased RF power deposition and susceptibility effects are prevalent at higher fields (15), which can give rise to errors in the T_2 measurements (39,40). However, our results show that these factors have negligible effect on the test-retest reliability and accuracy of the phantom and *in vivo* experiments. While the MSME sequence provides considerable time savings compared to a single-slice multi-echo sequence, cross-talk between slices can occur (60). However this cross-talk can be substantially decreased by adding slice gaps between adjacent slices (61). In our study, an inter-slice gap of 150% of the slice thickness was used that substantially reduced the influence of cross-talk between slices (61). In addition, it has been reported that introducing gaps between neighboring slices also helps in reducing magnetization transfer effects by increasing the resonance offset (60). A slight overestimation of the *in vivo* T_2 was observed with the MSME sequence compared to the single-slice sequence at 17.6 T. However, the T_2 of the mouse brain observed with the MSME sequence were consistently within 3 ms of the values acquired with the single-slice sequence for all regions (supplementary Fig. 3.2S).

In clinical evaluations T_2 values are often inaccurate in absolute terms due to the systematic errors related to *e.g.* the type of curve fitting used in the analysis, and the echo train length. In clinical evaluations, however, a good test-retest reliability of T_2, and shorter scan times are more important than absolute accuracy. The observation that the increase in T_2 using the MSME sequence as compared to the single-slice multi-echo sequence is relatively small, the absence of obvious inter-slice variation of T_2 in multi-slice imaging, and good test-retest reliability indicated that the MSME protocol can serve to find optimal parameters for T_2 weighted sequences at 17.6 T. In addition, the MSME sequence can be safely used for evaluation of disease progression in the mouse models of neurodegenerative diseases at 17.6 T.

In addition to T_2 values, we also measured *in vivo* T_1 changes for a variety of brain regions in young (3 months of age) and old (23 months of age) mice at 17.6 T. The T_1 values obtained for young mice are in excellent agreement with an earlier report at 17.6 T (18). Comparison of the T_1 values in multiple brain regions reveals a slightly lower T_1 for the corpus callosum and the caudate-putamen regions in old mice as compared to young mice. These age-dependent T_1 changes are in agreement with measurements in humans

(at 1.5 T) and rats (at 16.4 T) (47,62-64). In addition, we also observed slightly longer T_1 in the thalamus region of old mice as compared to young mice. An increase in the thalamus T_1 values with age has also been reported in MRI scans collected from humans at 1.5 T (64,65). The age-related changes in T_1 might reflect various physiological processes. For example an increase in iron content of brain tissue can lead to a decrease in T_1, while a decline in the number of myelinated fibers can cause an increase in T_1 (10,11).

In conclusion, our results provide a comprehensive and quantitative *in vivo* T_2 profile for various mouse brain regions at 17.6 T and show that the T_2 decreases substantially at 17.6 T compared to 9.4 T. In addition, age-related T_2 and T_1 changes in the mouse brain were observed, which provides a useful reference for comparison with disease-related deviations in T_2 and T_1 relaxation for future studies.

Acknowledgments

The authors wish to thank Kees Erkelens, Karthick Babu Sai Sankar Gupta and Fons Lefeber for their assistance during various stages of MRI measurements. This work was supported by grants from the Internationale Stichting Alzheimer Onderzoek (ISAO) and Centre for Medical Systems Biology (CMSB).

Supplementary Material

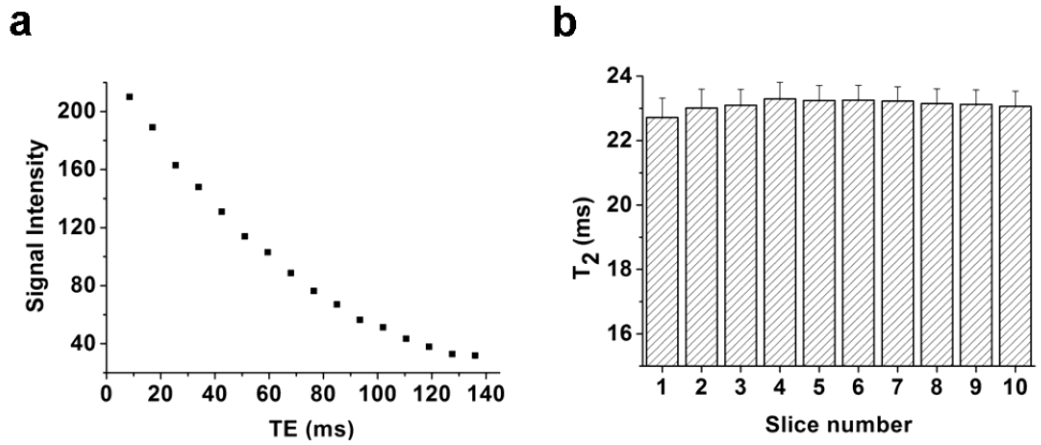

***Fig. 4.1S**. (a) Plot showing signal intensity versus echo time (TE) for Gd-DOTA phantom (10mM) solution measured using the MSME sequence with 16 echo times (TE); (b) T_2 (ms ± SE) of Gd-DOTA phantom (10mM) solution measured using the MSME sequence with 10 slices. No statistically significant variation in T_2 values was observed between the slices (P >0.05).*

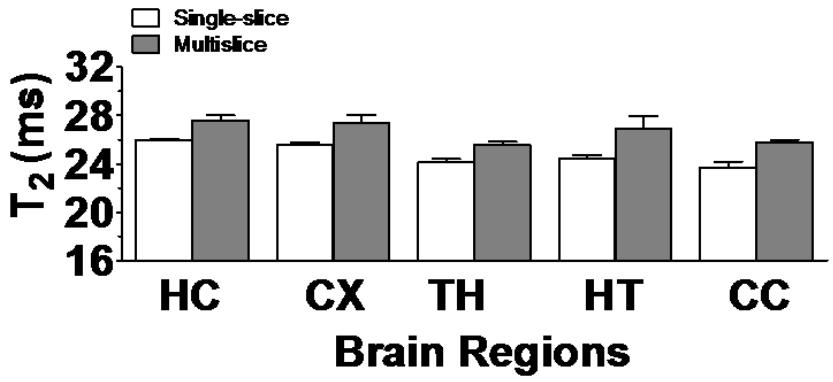

***Fig. 4.2S**. In vivo T_2 relaxation times of different mouse brain regions acquired by single-slice and multislice methods at 17.6 T. Error bars represent the SE over four animals. HC = hippocampus , CX = cortex, TH = thalamus, HT = hypothalamus, CC = corpus callosum. The T_2 values measured using multi-slice mode were slightly higher than those from the single-slice mode; however, the systematic overestimation was less than 3 ms.*

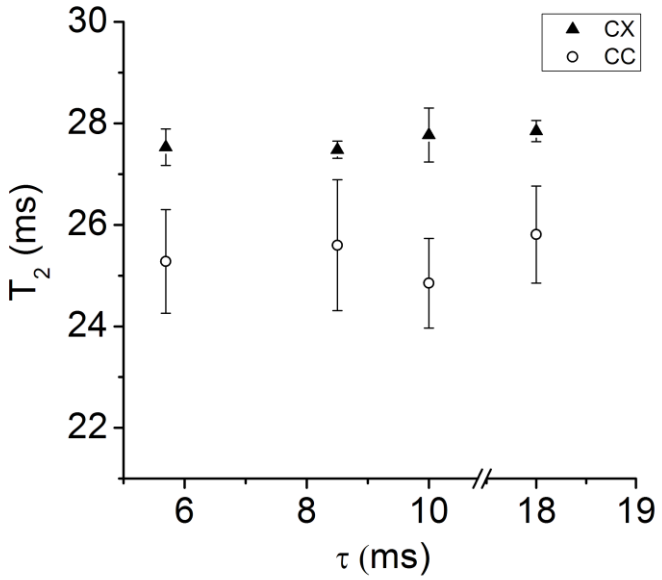

***Fig. 4.3S**. Effect of refocusing interpulse interval τ on the T_2 in cortex (CX) and corpus collasum (CC). T_2 values were measured using the MSME sequence with 4 different τ values, namely 5.6, 8.5, 10, and 18 ms. Values are expressed as mean T_2 in ms ± SD (error bars); n = 3.*

References

1. Damadian R. Tumor detection by nuclear magnetic resonance. Science 1971;171(976):1151-1153.
2. Helpern JA, Lee SP, Falangola MF, Dyakin VV, Bogart A, Ardekani B, Duff K, Branch C, Wisniewski T, de Leon MJ, Wolf O, O'Shea J, Nixon RA. MRI assessment of neuropathology in a transgenic mouse model of Alzheimer's disease. Magn Reson Med 2004;51(4):794-798.
3. Deoni SC. Quantitative relaxometry of the brain. Top Magn Reson Imaging 2010;21(2):101-113.
4. Ongur D, Prescot AP, Jensen JE, Rouse ED, Cohen BM, Renshaw PF, Olson DP. T2 relaxation time abnormalities in bipolar disorder and schizophrenia. Magn Reson Med 2010;63(1):1-8.
5. Seewann A, Vrenken H, van der Valk P, Blezer EL, Knol DL, Castelijns JA, Polman CH, Pouwels PJ, Barkhof F, Geurts JJ. Diffusely abnormal white matter in chronic multiple sclerosis: imaging and histopathologic analysis. Arch Neurol 2009;66(5):601-609.
6. Fullerton GD, Potter JL, Dornbluth NC. NMR relaxation of protons in tissues and other macromolecular water solutions. Magn Reson Imaging 1982;1(4):209-226.
7. Beaulieu C, Fenrich FR, Allen PS. Multicomponent water proton transverse relaxation and T2-discriminated water diffusion in myelinated and nonmyelinated nerve. Magnetic Resonance Imaging 1998;16(10):1201-1210.
8. Jones CK, Whittall KP, MacKay AL. Robust myelin water quantification: averaging vs. spatial filtering. Magn Reson Med 2003;50(1):206-209.
9. Bartzokis G. Age-related myelin breakdown: a developmental model of cognitive decline and Alzheimer's disease. Neurobiol Aging 2004;25(1):5-18; author reply 49-62.
10. Lacomis D, Osbakken M, Gross G. Spin-lattice relaxation (T1) times of cerebral white matter in multiple sclerosis. Magn Reson Med 1986;3(2):194-202.
11. Vymazal J, Brooks RA, Baumgarner C, Tran V, Katz D, Bulte JW, Bauminger R, Di Chiro G. The relation between brain iron and NMR relaxation times: an in vitro study. Magn Reson Med 1996;35(1):56-61.

12. Guilfoyle DN, Dyakin VV, O'Shea J, Pell GS, Helpern JA. Quantitative measurements of proton spin-lattice (T1) and spin-spin (T2) relaxation times in the mouse brain at 7.0 T. Magn Reson Med 2003;49(3):576-580.
13. Kumar R, Delshad S, Woo MA, Macey PM, Harper RM. Age-related regional brain T2-relaxation changes in healthy adults. J Magn Reson Imaging 2012;35(2):300-308.
14. de Graaf RA, Brown PB, McIntyre S, Nixon TW, Behar KL, Rothman DL. High magnetic field water and metabolite proton T1 and T2 relaxation in rat brain in vivo. Magn Reson Med 2006;56(2):386-394.
15. Hu X, Norris DG. Advances in high-field magnetic resonance imaging. Annu Rev Biomed Eng 2004;6:157-184.
16. Budde J, Shajan G, Hoffmann J, Ugurbil K, Pohmann R. Human imaging at 9.4 T using T(2)*-, phase-, and susceptibility-weighted contrast. Magn Reson Med 2010.
17. Schepkin VD, Brey WW, Gor'kov PL, Grant SC. Initial in vivo rodent sodium and proton MR imaging at 21.1 T. Magn Reson Imaging 2010;28(3):400-407.
18. van de Ven RC, Hogers B, van den Maagdenberg AM, de Groot HJ, Ferrari MD, Frants RR, Poelmann RE, van der Weerd L, Kiihne SR. T(1) relaxation in in vivo mouse brain at ultra-high field. Magn Reson Med 2007;58(2):390-395.
19. Kara F, van Dongen ES, Schliebs R, van Buchem MA, de Groot HJ, Alia A. Monitoring blood flow alterations in the Tg2576 mouse model of Alzheimer's disease by in vivo magnetic resonance angiography at 17.6T. NeuroImage 2012;60(2):958-966.
20. Kuo YT, Herlihy AH, So PW, Bhakoo KK, Bell JD. In vivo measurements of T1 relaxation times in mouse brain associated with different modes of systemic administration of manganese chloride. J Magn Reson Imaging 2005;21(4):334-339.
21. El Tannir El Tayara N, Delatour B, Le Cudennec C, Guegan M, Volk A, Dhenain M. Age-related evolution of amyloid burden, iron load, and MR relaxation times in a transgenic mouse model of Alzheimer's disease. Neurobiol Dis 2006;22(1):199-208.
22. Falangola MF, Dyakin VV, Lee SP, Bogart A, Babb JS, Duff K, Nixon R, Helpern JA. Quantitative MRI reveals aging-associated T2 changes in mouse models of Alzheimer's disease. NMR Biomed 2007;20(3):343-351.

23. Weidensteiner C, Metzger F, Bruns A, Bohrmann B, Kuennecke B, von Kienlin M. Cortical hypoperfusion in the B6.PS2APP mouse model for Alzheimer's disease: comprehensive phenotyping of vascular and tissular parameters by MRI. Magn Reson Med 2009;62(1):35-45.
24. Waterston RH, Lindblad-Toh K, Birney E, et al MGSC. Initial sequencing and comparative analysis of the mouse genome. Nature 2002;420(6915):520-562.
25. Braakman N, Matysik J, van Duinen SG, Verbeek F, Schliebs R, de Groot HJ, Alia A. Longitudinal assessment of Alzheimer's beta-amyloid plaque development in transgenic mice monitored by in vivo magnetic resonance microimaging. J Magn Reson Imaging 2006;24(3):530-536.
26. Carr HY, Purcell EM. Effects of Diffusion on Free Precession in Nuclear Magnetic Resonance Experiments. Phys Rev 1954;94(3):630-638.
27. Meiboom S, Gill D. Modified Spin-Echo Method for Measuring Nuclear Relaxation Times. Rev Sci Instrum 1958;29(8):688-691.
28. Hennig J, Nauerth A, Friedburg H. RARE imaging: a fast imaging method for clinical MR. Magn Reson Med 1986;3(6):823-833.
29. Corot C, Robert P, Idee JM, Port M. Recent advances in iron oxide nanocrystal technology for medical imaging. Adv Drug Deliv Rev 2006;58(14):1471-1504.
30. Rohrer M, Bauer H, Mintorovitch J, Requardt M, Weinmann HJ. Comparison of magnetic properties of MRI contrast media solutions at different magnetic field strengths. Invest Radiol 2005;40(11):715-724.
31. Muller R, Buttner P. A critical discussion of intraclass correlation coefficients. Stat Med 1994;13(23-24):2465-2476.
32. Bartzokis G, Mintz J, Marx P, Osborn D, Gutkind D, Chiang F, Phelan CK, Marder SR. Reliability of in vivo volume measures of hippocampus and other brain structures using MRI. Magn Reson Imaging 1993;11(7):993-1006.
33. Bloembergen N, Purcell EM, Pound RV. Relaxation Effects in Nuclear Magnetic Resonance Absorption. Phys Rev 1948;73(7):679-712.
34. Jezzard P, Duewell S, Balaban RS. MR relaxation times in human brain: measurement at 4 T. Radiology 1996;199(3):773-779.
35. Klug G, Kampf T, Bloemer S, Bremicker J, Ziener CH, Heymer A, Gbureck U, Rommel E, Noth U, Schenk WA, Jakob PM, Bauer WR. Intracellular and extracellular T1 and T2 relaxivities of magneto-optical nanoparticles at experimental high fields. Magn Reson Med 2010;64(6):1607-1615.

36. Michaeli S, Garwood M, Zhu XH, DelaBarre L, Andersen P, Adriany G, Merkle H, Ugurbil K, Chen W. Proton T2 relaxation study of water, N-acetylaspartate, and creatine in human brain using Hahn and Carr-Purcell spin echoes at 4T and 7T. Magn Reson Med 2002;47(4):629-633.
37. Crawley AP, Henkelman RM. Errors in T2 estimation using multislice multiple-echo imaging. Magn Reson Med 1987;4(1):34-47.
38. Oh J, Han ET, Pelletier D, Nelson SJ. Measurement of in vivo multi-component T2 relaxation times for brain tissue using multi-slice T2 prep at 1.5 and 3 T. Magn Reson Imaging 2006;24(1):33-43.
39. Majumdar S, Orphanoudakis SC, Gmitro A, O'Donnell M, Gore JC. Errors in the measurements of T2 using multiple-echo MRI techniques. II. Effects of static field inhomogeneity. Magn Reson Med 1986;3(4):562-574.
40. Majumdar S, Orphanoudakis SC, Gmitro A, O'Donnell M, Gore JC. Errors in the measurements of T2 using multiple-echo MRI techniques. I. Effects of radiofrequency pulse imperfections. Magn Reson Med 1986;3(3):397-417.
41. Poon CS, Henkelman RM. Practical T2 quantitation for clinical applications. J Magn Reson Imaging 1992;2(5):541-553.
42. Whittall KP, MacKay AL, Graeb DA, Nugent RA, Li DK, Paty DW. In vivo measurement of T2 distributions and water contents in normal human brain. Magn Reson Med 1997;37(1):34-43.
43. Gareau PJ, Rutt BK, Bowen CV, Karlik SJ, Mitchell JR. In vivo measurements of multi-component T2 relaxation behaviour in guinea pig brain. Magn Reson Imaging 1999;17(9):1319-1325.
44. Dydak U, Schar M. MR spectroscopy and spectroscopic imaging: comparing 3.0 T versus 1.5 T. Neuroimaging Clin N Am 2006;16(2):269-283, x.
45. Soher BJ, Dale BM, Merkle EM. A review of MR physics: 3T versus 1.5T. Magn Reson Imaging Clin N Am 2007;15(3):277-290, v.
46. Deelchand DK, Van de Moortele PF, Adriany G, Iltis I, Andersen P, Strupp JP, Vaughan JT, Ugurbil K, Henry PG. In vivo 1H NMR spectroscopy of the human brain at 9.4 T: initial results. J Magn Reson 2010;206(1):74-80.
47. Pohmann R, Shajan G, Balla DZ. Contrast at high field: Relaxation times, magnetization transfer and phase in the rat brain at 16.4 T. Magn Reson Med 2011.

48. Duewell SH, Ceckler TL, Ong K, Wen H, Jaffer FA, Chesnick SA, Balaban RS. Musculoskeletal MR imaging at 4 T and at 1.5 T: comparison of relaxation times and image contrast. Radiology 1995;196(2):551-555.
49. Chen JH, Avram HE, Crooks LE, Arakawa M, Kaufman L, Brito AC. In vivo relaxation times and hydrogen density at 0.063-4.85 T in rats with implanted mammary adenocarcinomas. Radiology 1992;184(2):427-434.
50. Cremillieux Y, Ding SJ, Dunn JF. High-resolution in vivo measurements of transverse relaxation times in rats at 7 Tesla. Magn Reson Med 1998;39(2):285-290.
51. Fischer HW, Rinck PA, Van Haverbeke Y, Muller RN. Nuclear relaxation of human brain gray and white matter: analysis of field dependence and implications for MRI. Magn Reson Med 1990;16(2):317-334.
52. Bartha R, Michaeli S, Merkle H, Adriany G, Andersen P, Chen W, Ugurbil K, Garwood M. In vivo (H2O)-H-1 T-2(dagger) measurement in the human occipital lobe at 4T and 7T by Carr-Purcell MRI: Detection of microscopic susceptibility contrast. Magn Reson Med 2002;47(4):742-750.
53. Hardy PA, Henkelman RM. Transverse Relaxation Rate Enhancement Caused by Magnetic Particulates. Magnetic Resonance Imaging 1989;7(3):265-275.
54. Vymazal J, Brooks RA, Baumgarner C, Tran V, Katz D, Bulte JWM, Bauminger ER, DiChiro G. The relation between brain iron and NMR relaxation times: An in vitro study. Magn Reson Med 1996;35(1):56-61.
55. Brooks RA, Vymazal J, Bulte JWM, Baumgarner CD, Tran V. Comparison of T2 Relaxation in Blood, Brain, and Ferritin. Jmri-J Magn Reson Im 1995;5(4):446-450.
56. Stefanovic B, Sled JG, Pike GB. Quantitative T-2 in the occipital lobe: The role of the CPMG refocusing rate. Journal of Magnetic Resonance Imaging 2003;18(3):302-309.
57. Jackson GD, Connelly A, Duncan JS, Grunewald RA, Gadian DG. Detection of hippocampal pathology in intractable partial epilepsy: increased sensitivity with quantitative magnetic resonance T2 relaxometry. Neurology 1993;43(9):1793-1799.
58. Briellmann RS, Kalnins RM, Berkovic SF, Jackson GD. Hippocampal pathology in refractory temporal lobe epilepsy: T2-weighted signal change reflects dentate gliosis. Neurology 2002;58(2):265-271.

59. Chen JC, Hardy PA, Clauberg M, Joshi JG, Parravano J, Deck JH, Henkelman RM, Becker LE, Kucharczyk W. T2 values in the human brain: comparison with quantitative assays of iron and ferritin. Radiology 1989;173(2):521-526.
60. Santyr GE. Magnetization transfer effects in multislice MR imaging. Magn Reson Imaging 1993;11(4):521-532.
61. Watanabe A, Boesch C, Obata T, Anderson SE. Effect of multislice acquisition on T1 and T2 measurements of articular cartilage at 3T. J Magn Reson Imaging 2007;26(1):109-117.
62. Saito N, Sakai O, Ozonoff A, Jara H. Relaxo-volumetric multispectral quantitative magnetic resonance imaging of the brain over the human lifespan: global and regional aging patterns. Magnetic Resonance Imaging 2009;27(7):895-906.
63. Oros-Peusquens AM, Laurila M, Shah NJ. Magnetic field dependence of the distribution of NMR relaxation times in the living human brain. Magn Reson Mater Phy 2008;21(1-2):131-147.
64. Cho S, Jones D, Reddick WE, Ogg RJ, Steen RG. Establishing norms for age-related changes in proton T1 of human brain tissue in vivo. Magnetic Resonance Imaging 1997;15(10):1133-1143.
65. Steen RG, Gronemeyer SA, Taylor JS. Age-related changes in proton T1 values of normal human brain. J Magn Reson Imaging 1995;5(1):43-48.

5 General Discussion and Future Outlook*

In this thesis the potential applications of high-resolution MR angiography and relaxometry to study Alzheimer's disease pathology in transgenic mouse models were investigated at ultra high magnetic fields. The specific focus was both on the MRA and the relaxometry method optimization, as well as their application to monitor AD related changes, such as blood flow abnormalities and myelin breakdown, and to understand the underlying mechanisms of these changes.

5.1 Monitoring blood flow abnormalities in an AD mouse model

In Chapter 2 it was shown that improved visualization of cerebral vasculature of mouse brain is possible by applying *in vivo* MRA at 17.6 T. The results presented in this chapter show that MRA image quality at 17.6 T is already significantly higher than the one acquired at 9.4 T. Due to ultra-high field strength (17.6 T) and use of strong gradients, the small sized arteries were very clearly imaged up to the level of the pial vessels.

The optimized MRA method was applied to detect AD related blood flow defects in cerebral arteries in Tg2576 mice at 17.6 T. In addition, amyloid plaque load was assessed based on T_2 weighted images and also in subsequent immunohistochemical staining of histological sections.Abnormal hypointensities seen on the MRA scans were counted and scored for comparison with wild-type mice. Signal hypointensities and plaque load were both shown to increase with age in the affected mice and to differ from wild-type mice. Overall decrease in the brightness of the arteries was observed in transgenic mice as compared to wild-type. In particular, the middle cerebral artery and the anterior communicating artery were the most significantly affected vessels in Tg2576 mice. Histological data revealed that CAA might be responsible for impaired cerebral blood flow, thereby contributing to the progression of AD. Our data suggest that after a certain level of elevation of Aβ deposits, blood flow abnormalities can be observed with MRA, thus challenging the view that elevated soluble Aβ levels provide sufficient and necessary condition to cause severe blood flow abnormalities.

Along with CAA, many other factors such as oxidative stress and Aβ induced endothelial

*Parts of this chapter were published in Curr Med Imag Rev 2011; 7:1:80-87

dysfunction might have contributed to blood flow abnormalities. It has been reported that cerebrovascular dysfunction in aged Tg2576 mice could be fully rescued by antioxidants and the peroxisome proliferator-activated receptor agonist pioglitazone without reducing brain Aβ plaque load (1).

Rescuing cerebrovascular function in AD can be an interesting alternative to counteract AD pathology (1). Imaging blood flow and vasculature architecture changes during AD progression with MRA could be used to evaluate success of potential therapies targeting blood flow abnormalities. The ability of ultra high field MRA to provide information about small cerebral vessels at high spatial resolution has the potential to improve our understanding about the AD. The MRA technique discussed here still needs further development to be used diagnostically or as a tool for drug discovery. MRA sensitivity can be increased by use of higher magnetic field strengths, a cryogenic RF probe and non-toxic contrast agents (2).

5.2 Probing white matter abnormalities in AD using T_2 measurements

Neuropathological diagnosis of AD is still based on the presence of primarily gray matter alterations due to abundant Aβ deposition in these regions. In recent years, a strong interest in white matter pathology seen in AD has developed (3-5). In particular abnormalities in corpus callosum (*i.e.* largest white matter structure in the brain), has been associated with AD pathology. Since the corpus callosum plays an important role in functional connectivity and cognitive processing, abnormalities in corpus callosum integrity can lead to clear functional defects, including impairment in cognitive processes (6). A systematic assessment of the T_2 values in the corpus callosum in mouse models of AD is still missing.

In Chapter 3 T_2 changes in the corpus callosum in a mouse model of AD with age (10 to 18 months) were monitored. A significant elongation in T_2 values of the corpus callosum in Tg2576 mice compared to wild-type was observed at all ages (10-18 months), whereas a significant decrease in T_2 was observed in the cortex and hippocampus of 18 months Tg2576 mice. Myelinated fibers in corpus callosum are composed of lipids, proteins and water. Demyelination and gliosis increase free-to bound ratio of the water in the tissue, which causes an increase in T_2 values. In this chapter the increase in T_2 values in corpus callosum was correlated with demyelination and gliosis, which were confirmed with

histology. The decrease in the T_2 values observed in the hippocampus and cortex can be due to magnetic field inhomogeneities created by iron containing Aβ plaques.

This chapter highlights open questions and motivates future research. First, there are no longitudinal T_2 studies that were conducted to assess changes in white matter integrity in the corpus callosum in mouse models of AD. Second, future studies are required to determine how vascular factors affect the white matter integrity of the corpus callosum. Third, the behavioural outcome of white matter abnormalities remains unclear. There is clearly a need for studies correlating these abnormalities with classic hallmarks of AD pathology, such as amyloid load, gliosis and neurofibrillary tangle. Hybrid MRI/PET devices might be employed for this purpose. Interestingly, in this chapter white matter integrity changes in corpus callosum did not show a strong correlation with Aβ load.

White matter consists of myelinated fiber tracts that interconnect various parts of the cerebral hemisphere. Abnormalities in integrity of white matter may cause disconnection between different regions of the brain. This raises the hypothesis that AD includes a disconnection disorder. Future studies using novel MRI methods, such as resting state functional MRI, can investigate networking problems related with white matter abnormalities. Our results suggest that a decrease in white matter integrity in the corpus callosum might be an early event in the course of AD and raises the possibility that both gliosis and myelin related pathology might be contributing to AD onset.

Currently, there exist little data concerning the neurobiological basis of white matter integrity decline in AD. A better understanding of the neurobiological underpinnings of microstructural changes in corpus callosum and other white matter regions associated with AD-risk has the potential to aid the development of novel pharmacological intervention strategies for AD. New treatment strategies, intended to protect axon and myelin integrity in seniors at risk of AD, might be more successful to prevent or slow down the disease progression.

5.3 *In vivo* Measurement of T_2 in the Mouse Brain at 17.6 T

Previous studies have shown that many factors influence the ability to obtain accurate multi-component T_2 data *in vivo* using CPMG imaging sequences, including: the SNR, the refocusing interpulse interval and partial volume effects (7-9). Further improvement in the accuracy of T_2 data can be achieved using a variety of strategies, such as using an

optimized refocusing interpulse interval and increased magnetic field strength. In particular, ultra-high magnetic field systems provide greater SNR and increased resolution, which can increase the sensitivity and specificity of T_2 measurements to detect subtle tissue changes during AD progression.

In Chapter 4, the normative T_2 and T_1 values at 17.6 T over different mouse brain regions with age were established. In this chapter, the dependence of tissue T_2 values on magnetic field was also investigated by comparing the T_2 values acquired at 17.6 T with those acquired at 9.4 T. Field dependent decrease in tissue T_2 values was observed with increasing field strength. The T_2 dependence on magnetic field strength is in contradiction to the Bloembergen-Purcell-Pound dipolar relaxation model, which predicts T_2 to be independent of the field strength (10,11). The decrease in tissue T_2 with increasing field strength observed in this study can be explained by increased microscopic susceptibility effects, causing irreversible dephasing due to diffusion (12).

In this chapter, T_2 changes of brain regions were monitored with age at 17.6 T. A relatively short refocusing interpulse interval was used to acquire T_2 values of mouse brain regions in order to decrease the contribution of diffusion or chemical exchange effects on T_2 data. Many brain regions showed an age-dependent increase in T_2 values. The age-dependent increase in tissue T_2 values can be due to neuronal and axonal tissue degradation (13-16), whereas the decrease in tissue T_2 values could result from deposition of paramagnetic substances such as ferritin and hemosiderin (17,18). Overall these results show that age-dependent changes in tissue T_2 relaxation times can be accurately measured at 17.6 T. These estimates of *in vivo* T_2 relaxation of mouse brain will be useful to optimize sequences for optimal image contrast and will serve as a useful reference for comparison with disease related deviations in T_2 and T_1 values.

5.3.1 Future outlook

5.3.1.1 Metabolic profiling of AD by magnetic resonance spectroscopy

The new updated criteria and guidelines for the diagnosis of AD defines three stages of AD, which includes preclinical (19), mild cognitive impairment (20) and dementia (21). These updated guidelines aim to accelerate the development and implementation of potential biomarkers of AD to identify predementia and even preclinical asymptomatic stages of the disease. *In vivo* neuroimaging methods have the capability to detect early

structural, functional and metabolic changes in AD brain. While structural and functional changes can be detected with MRI, MRS can provide a wealth of information on various aspects of *in vivo* neurochemistry, including neuronal health, gliosis, osmoregulation, energy metabolism, neuronal-glial cycling, and molecular synthesis rates in brain of AD patients (22-25). In mouse models of AD, the relation between metabolic changes that can be detected *in vivo* using MRS and cerebral Aβ accumulation is examined by sacrificing mice of different ages. However, the correlation between Aβ deposition and neurochemical changes would be more reliable if both could be measured *in vivo* in the same mice repeatedly over time.

In vivo detection of Aβ plaques using MRI without using a contrast agent has been reported in transgenic mouse models of AD (26,27). Subsequently our group has performed the first longitudinal μMRI study to follow the development of plaques with age in the same mice (28). In a follow-up study we studied the temporal relationship between the severity of plaque deposition monitored by *in vivo* μMRI and the altered neurochemical profile monitored by *in vivo* MRS in the same Tg2576 mice with age between 12 and 18 months (Fig. 5.1) (29). A clear increase in the level of taurine was observed with age between 14 and 18 months (Fig. 5.1). The increase in taurine was more drastic between 16 and 18 months and was correlated with the severity of plaque load at these ages. A decline in NAA with age was clearly observed between 12 and 18 months (Fig. 5.1). However, the drastic decrease in NAA was registered at the age between 14 and 16 months. In addition, the analysis of the plaque load and its temporal relationship with each altered metabolite are underway.

In recent years, the use of *in vivo* MRS in AD research has become more widespread. Common findings of *in vivo* MRS in human AD patients and AD mouse models are: a decrease in NAA and an increase in mIns. Because of these consistent findings, these metabolic changes have been proposed as potential biomarkers for early diagnosis of AD. These changes also correlated with an increase in amyloid plaque load and a decrease in cognitive performance. Although a decrease in NAA and an increase in either mIns or taurine have been consistently observed in AD, these changes are not specific only for AD. The same changes have been shown to occur in other neurodegenerative diseases such as Huntington's disease, Parkinson's disease and in other brain disorders (30-33). Therefore, specific *in vivo* MRS markers of AD are still missing. The use of localized *in vivo* ^{1}H MRS in mice is often hampered by low sensitivity of local measurements due to both the small size of the brain and low concentrations of several brain metabolites,

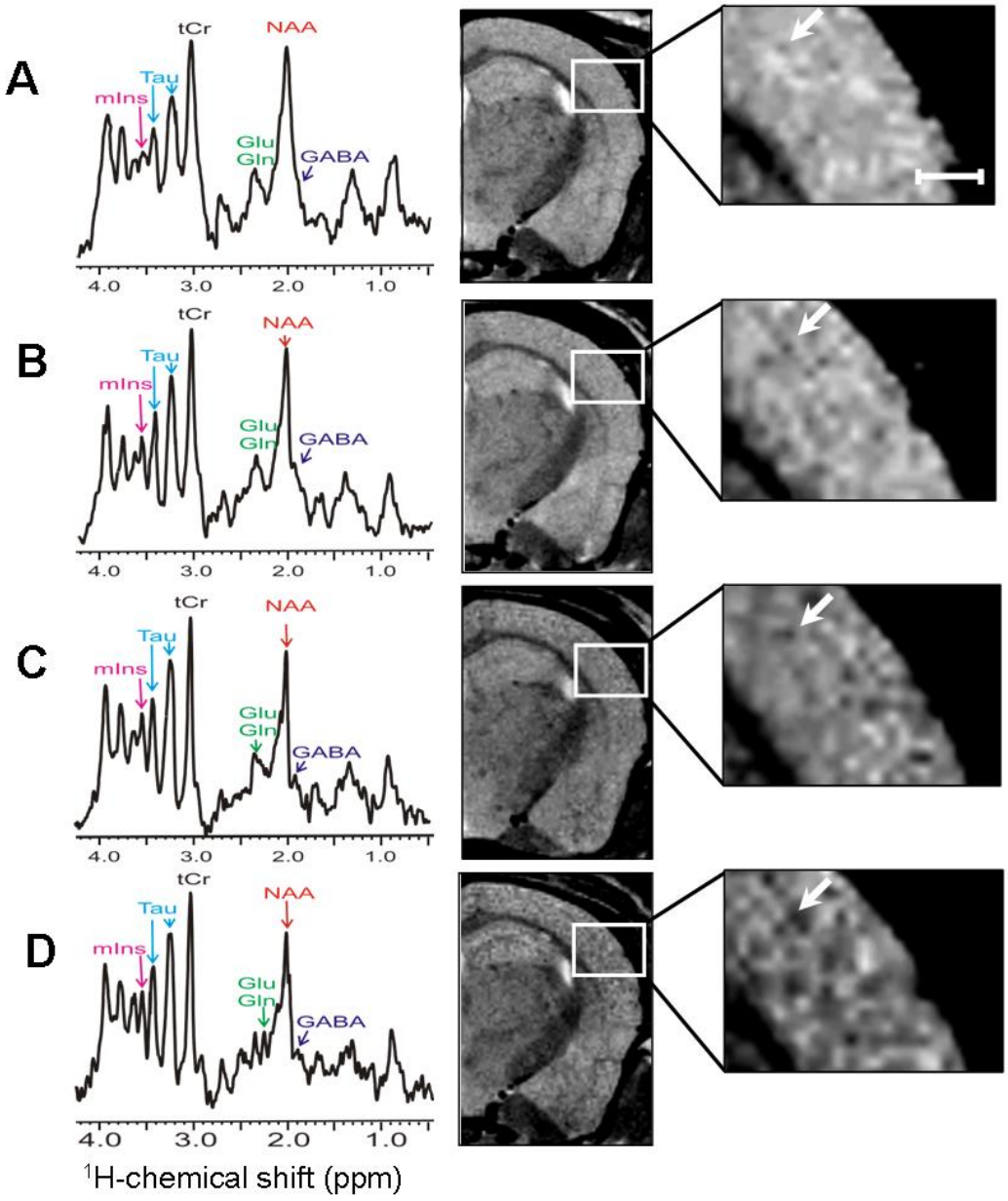

Fig. 5.1. Correlation between the development of Aβ plaques monitored by in vivo µMRI and changes in neurochemical profile monitored by MRS with age in the brain of the same AD transgenic mouse at the age of 12 months (A), 14 months (B), 16 months (C), and 18 months (D). ^{1}H-MR spectra were obtained from a 8 µl voxel placed in the cortex-hippocampus region at 9.4T using a PRESS sequence (TR/TE 3500/15 ms). A decrease in NAA and an increase in Tau with age can be clearly seen in the MR spectra on the left. MR images were acquired at 9.4T using a RARE sequence (TR/TE 6s/10.5ms; RARE factor 4). The magnified subsampled areas of the MR images on the right show an increase in plaque load with age. Scale bar, 400 µm.

which result in limited signal-to-noise ratio. A significant limitation of 1D ^{1}H MRS is the spectral crowding since most of the metabolite resonances are restricted to a narrow chemical shift range of 5 ppm. Detection of most of the metabolites is hampered by spectral overlap with other metabolites. Therefore important neurotransmitters and other metabolites, which are in low concentration or with multiple splitting, cannot be reliably resolved (34,35). This limitation makes the data difficult to interpret, particularly in relation to metabolites such as GABA, Glu and Gln. Thus, further improvement in *in vivo* ^{1}H MRS is required to monitor small but crucial changes in the AD mouse brain.

Future MRS studies in AD mice should take advantage of the availability of higher magnetic field strengths, new experimental MRS methods and of the option to exploit other nuclei such as ^{13}C, ^{16}F, ^{7}Li, ^{23}Na. *In vivo* MRS studies in AD mice have been performed in magnetic field strengths up to 9.4T. For nuclear MRS a higher magnetic field strength is always desirable. Moving from 9.4T to higher fields, such as 17.6T, is expected to be beneficial, since high field strength will improve signal-to-noise ratio as well as spectral resolution, thus enabling the reliable identification of metabolites at low concentrations or with coupled spin systems. The problem of spectral overlap can be reduced by using 2D MRS methods. Compared to conventional, one-dimensional MRS, localized 2D MRS reduces the problem of spectral overlap considerably, as the resonances are dispersed over a two-dimensional surface, allowing the separation and unambiguous assignment of resonances of several metabolites in a single measurement. Recently several 2D MRS sequences have been used for studying brain metabolism in human subjects, although not in AD patients, using clinical MRI scanners (35-37). The techniques based on localized variations of the 2D chemical shift correlated spectroscopic sequence appear most promising with regard to identifying metabolites that cannot be resolved using conventional 1D MRS sequences due to spectral crowding. Our group has recently implemented a localized 2D MRS technique at 9.4T and, for the first time, obtained highly resolved localized 2D MR spectra from the living mouse brain (34). Use of localized 2D MRS allowed clear and simultaneous detection of a large number of brain metabolites based on their network of cross-peaks in localized regions of the mouse brain *in vivo*. A clear separation of the cross-peaks of Glu, Gln, GSH and GABA, allowed direct *in vivo* assignment of resonances of these coupled spin systems. In addition, the cross- peak of NAAG was separated from NAA (34). The 2D spectrum also showed well-resolved cross-peaks of many other metabolites present at low concentration, such as alanine, aspartate, α-glucose, tyrosine, threonine, and glycerol. These results demonstrate the feasibility of 2D MRS to get localized access to the mouse brain for

efficient identification of metabolites (34). This method can be applied to mouse models of AD and has a great potential for resolving brain metabolites hidden under overlapping multiplets, which will have significant implication in detecting new biomarkers of AD in the near future.

Other spectroscopic imaging techniques, such as chemical shift imaging, proton echo planar spectroscopic imaging and double echo-filter metabolite imaging can also be applied to mouse models of AD (38). In addition to ^{1}H MRS, the use of other nuclei can be exploited in AD, although other nuclei are not as sensitive as ^{1}H. The sensitivity levels of other nuclei relative to ^{1}H are 6.65% (^{31}P), 0.018% (^{13}C), 83.4% (^{16}F), and 27.2% (^{7}Li) (39). Despite its low sensitivity, ^{31}P is one of the most commonly used nuclei in brain research after ^{1}H MRS, which provides important information about changes in the levels of membrane phospholipids and high energy metabolites (40). Another nucleus, ^{13}C, has also been used in humans but it has not yet been applied in mouse models of AD. Despite its low sensitivity, ^{13}C MRS can help to overcome significant problems of spectral overcrowding and magnet frequency. For example it can provide invaluable data, particularly in relation to Glu-Gln cycling and astrocytic activity (41,42). Recent applications of ^{13}C MRS in humans have shown that it may have potential application in AD as well as other neurodegenerative disorders (41). This method can even be of greater significance if it is coupled with ^{1}H or ^{31}P MRS.

In conclusion, *in vivo* MRS is a powerful tool to unravel the neurochemical basis of AD in transgenic mouse models. The full potential of MRS in AD mouse model has not yet been exploited, and we expect that higher magnetic field strengths combined with exploitation of other nuclei than ^{1}H will further and substantially increase our understanding of the early stages of AD.

References

1. Nicolakakis N, Aboulkassim T, Ongali B, Lecrux C, Fernandes P, Rosa-Neto P, Tong XK, Hamel E. Complete rescue of cerebrovascular function in aged Alzheimer's disease transgenic mice by antioxidants and pioglitazone, a peroxisome proliferator-activated receptor gamma agonist. J Neurosci 2008;28(37):9287-9296.
2. Baltes C, Radzwill N, Bosshard S, Marek D, Rudin M. Micro MRI of the mouse brain using a novel 400 MHz cryogenic quadrature RF probe. NMR Biomed 2009;22(8):834-842.
3. Sjobeck M, Haglund M, Englund E. Decreasing myelin density reflected increasing white matter pathology in Alzheimer's disease--a neuropathological study. Int J Geriatr Psychiatry 2005;20(10):919-926.
4. Englund E, Brun A, Alling C. White matter changes in dementia of Alzheimer's type. Biochemical and neuropathological correlates. Brain 1988;111 (Pt 6):1425-1439.
5. Brun A, Englund E. A white matter disorder in dementia of the Alzheimer type: a pathoanatomical study. Ann Neurol 1986;19(3):253-262.
6. Hinkley LB, Marco EJ, Findlay AM, Honma S, Jeremy RJ, Strominger Z, Bukshpun P, Wakahiro M, Brown WS, Paul LK, Barkovich AJ, Mukherjee P, Nagarajan SS, Sherr EH. The role of corpus callosum development in functional connectivity and cognitive processing. PLoS One 2012;7(8):e39804.
7. Crawley AP, Henkelman RM. Errors in T2 estimation using multislice multiple-echo imaging. Magn Reson Med 1987;4(1):34-47.
8. Graham SJ, Stanchev PL, Bronskill MJ. Criteria for analysis of multicomponent tissue T2 relaxation data. Magn Reson Med 1996;35(3):370-378.
9. Poon CS, Henkelman RM. Practical T2 quantitation for clinical applications. J Magn Reson Imaging 1992;2(5):541-553.
10. Bloembergen N, Purcell EM, Pound RV. Relaxation Effects in Nuclear Magnetic Resonance Absorption. Phys Rev 1948;73(7):679-712.
11. de Graaf RA, Brown PB, McIntyre S, Nixon TW, Behar KL, Rothman DL. High magnetic field water and metabolite proton T1 and T2 relaxation in rat brain in vivo. Magn Reson Med 2006;56(2):386-394.

12. Jezzard P, Duewell S, Balaban RS. MR relaxation times in human brain: measurement at 4 T. Radiology 1996;199(3):773-779.
13. Kumar R, Delshad S, Woo MA, Macey PM, Harper RM. Age-related regional brain T2-relaxation changes in healthy adults. J Magn Reson Imaging 2012;35(2):300-308.
14. Jackson GD, Connelly A, Duncan JS, Grunewald RA, Gadian DG. Detection of hippocampal pathology in intractable partial epilepsy: increased sensitivity with quantitative magnetic resonance T2 relaxometry. Neurology 1993;43(9):1793-1799.
15. Briellmann RS, Kalnins RM, Berkovic SF, Jackson GD. Hippocampal pathology in refractory temporal lobe epilepsy: T2-weighted signal change reflects dentate gliosis. Neurology 2002;58(2):265-271.
16. Seewann A, Vrenken H, van der Valk P, Blezer EL, Knol DL, Castelijns JA, Polman CH, Pouwels PJ, Barkhof F, Geurts JJ. Diffusely abnormal white matter in chronic multiple sclerosis: imaging and histopathologic analysis. Arch Neurol 2009;66(5):601-609.
17. Chen JC, Hardy PA, Clauberg M, Joshi JG, Parravano J, Deck JH, Henkelman RM, Becker LE, Kucharczyk W. T2 values in the human brain: comparison with quantitative assays of iron and ferritin. Radiology 1989;173(2):521-526.
18. Vymazal J, Brooks RA, Baumgarner C, Tran V, Katz D, Bulte JW, Bauminger R, Di Chiro G. The relation between brain iron and NMR relaxation times: an in vitro study. Magn Reson Med 1996;35(1):56-61.
19. Sperling RA, Aisen PS, Beckett LA, Bennett DA, Craft S, Fagan AM, Iwatsubo T, Jack CR, Jr., Kaye J, Montine TJ, Park DC, Reiman EM, Rowe CC, Siemers E, Stern Y, Yaffe K, Carrillo MC, Thies B, Morrison-Bogorad M, Wagster MV, Phelps CH. Toward defining the preclinical stages of Alzheimer's disease: recommendations from the National Institute on Aging-Alzheimer's Association workgroups on diagnostic guidelines for Alzheimer's disease. Alzheimer's & dementia : the journal of the Alzheimer's Association 2011;7(3):280-292.
20. Albert MS, DeKosky ST, Dickson D, Dubois B, Feldman HH, Fox NC, Gamst A, Holtzman DM, Jagust WJ, Petersen RC, Snyder PJ, Carrillo MC, Thies B, Phelps CH. The diagnosis of mild cognitive impairment due to Alzheimer's disease: recommendations from the National Institute on Aging-Alzheimer's Association

workgroups on diagnostic guidelines for Alzheimer's disease. Alzheimer's & dementia : the journal of the Alzheimer's Association 2011;7(3):270-279.

21. McKhann GM, Knopman DS, Chertkow H, Hyman BT, Jack CR, Jr., Kawas CH, Klunk WE, Koroshetz WJ, Manly JJ, Mayeux R, Mohs RC, Morris JC, Rossor MN, Scheltens P, Carrillo MC, Thies B, Weintraub S, Phelps CH. The diagnosis of dementia due to Alzheimer's disease: recommendations from the National Institute on Aging-Alzheimer's Association workgroups on diagnostic guidelines for Alzheimer's disease. Alzheimer's & dementia : the journal of the Alzheimer's Association 2011;7(3):263-269.
22. Bartha R, Smith M, Rupsingh R, Rylett J, Wells JL, Borrie MJ. High field (1)H MRS of the hippocampus after donepezil treatment in Alzheimer disease. Prog Neuropsychopharmacol Biol Psychiatry 2008;32(3):786-793.
23. Choi IY, Lee SP, Guilfoyle DN, Helpern JA. In vivo NMR studies of neurodegenerative diseases in transgenic and rodent models. Neurochem Res 2003;28(7):987-1001.
24. Jessen F, Block W, Traber F, Keller E, Flacke S, Lamerichs R, Schild HH, Heun R. Decrease of N-acetylaspartate in the MTL correlates with cognitive decline of AD patients. Neurology 2001;57(5):930-932.
25. Krishnan KR, Charles HC, Doraiswamy PM, Mintzer J, Weisler R, Yu X, Perdomo C, Ieni JR, Rogers S. Randomized, placebo-controlled trial of the effects of donepezil on neuronal markers and hippocampal volumes in Alzheimer's disease. Am J Psychiatry 2003;160(11):2003-2011.
26. Jack CR, Jr., Wengenack TM, Reyes DA, Garwood M, Curran GL, Borowski BJ, Lin J, Preboske GM, Holasek SS, Adriany G, Poduslo JF. In vivo magnetic resonance microimaging of individual amyloid plaques in Alzheimer's transgenic mice. J Neurosci 2005;25(43):10041-10048.
27. Vanhoutte G, Dewachter I, Borghgraef P, Van Leuven F, Van der Linden A. Noninvasive in vivo MRI detection of neuritic plaques associated with iron in APP[V717I] transgenic mice, a model for Alzheimer's disease. Magn Reson Med 2005;53(3):607-613.
28. Braakman N, Matysik J, van Duinen SG, Verbeek F, Schliebs R, de Groot HJ, Alia A. Longitudinal assessment of Alzheimer's beta-amyloid plaque development in transgenic mice monitored by in vivo magnetic resonance microimaging. J Magn Reson Imaging 2006;24(3):530-536.

29. Braakman N, Matysik, J., de Groot, HJM., Schliebs, R., Alia, A.,. Correlation between neurochemical changes and development of Alzheimer's plaques with age monitored by in vivo high resolution magnetic resonance microimaging and spectroscopy.; 2008 2008. p 257.
30. Choi JK, Dedeoglu A, Jenkins BG. Application of MRS to mouse models of neurodegenerative illness. NMR Biomed 2007;20(3):216-237.
31. Boska MD, Lewis TB, Destache CJ, Benner EJ, Nelson JA, Uberti M, Mosley RL, Gendelman HE. Quantitative 1H magnetic resonance spectroscopic imaging determines therapeutic immunization efficacy in an animal model of Parkinson's disease. J Neurosci 2005;25(7):1691-1700.
32. Oz G, Nelson CD, Koski DM, Henry PG, Marjanska M, Deelchand DK, Shanley R, Eberly LE, Orr HT, Clark HB. Noninvasive detection of presymptomatic and progressive neurodegeneration in a mouse model of spinocerebellar ataxia type 1. J Neurosci 2010;30(10):3831-3838.
33. Tsang TM, Woodman B, McLoughlin GA, Griffin JL, Tabrizi SJ, Bates GP, Holmes E. Metabolic characterization of the R6/2 transgenic mouse model of Huntington's disease by high-resolution MAS 1H NMR spectroscopy. J Proteome Res 2006;5(3):483-492.
34. Braakman N, Oerther T, de Groot HJ, Alia A. High resolution localized two-dimensional MR spectroscopy in mouse brain in vivo. Magn Reson Med 2008;60(2):449-456.
35. Thomas MA, Yue K, Binesh N, Davanzo P, Kumar A, Siegel B, Frye M, Curran J, Lufkin R, Martin P, Guze B. Localized two-dimensional shift correlated MR spectroscopy of human brain. Magn Reson Med 2001;46(1):58-67.
36. Binesh N, Yue K, Fairbanks L, Thomas MA. Reproducibility of localized 2D correlated MR spectroscopy. Magn Reson Med 2002;48(6):942-948.
37. Thomas MA, Hattori N, Umeda M, Sawada T, Naruse S. Evaluation of two-dimensional L-COSY and JPRESS using a 3 T MRI scanner: from phantoms to human brain in vivo. NMR Biomed 2003;16(5):245-251.
38. Ross AJ, Sachdev PS. Magnetic resonance spectroscopy in cognitive research. Brain Res Brain Res Rev 2004;44(2-3):83-102.
39. Frangou S, Williams SC. Magnetic resonance spectroscopy in psychiatry: basic principles and applications. Br Med Bull 1996;52(3):474-485.

40. Pettegrew JW, Klunk WE, Panchalingam K, McClure RJ, Stanley JA. Molecular insights into neurodevelopmental and neurodegenerative diseases. Brain Res Bull 2000;53(4):455-469.
41. Ross B, Lin A, Harris K, Bhattacharya P, Schweinsburg B. Clinical experience with 13C MRS in vivo. NMR Biomed 2003;16(6-7):358-369.
42. Shen J, Petersen KF, Behar KL, Brown P, Nixon TW, Mason GF, Petroff OA, Shulman GI, Shulman RG, Rothman DL. Determination of the rate of the glutamate/glutamine cycle in the human brain by in vivo 13C NMR. Proc Natl Acad Sci U S A 1999;96(14):8235-8240.

Summary

Dementia due to AD has had tremendous impact on the affected individuals, care givers and medical health care system. Both developed and developing countries will face the challenge of coping with a high frequency of AD, which is a characteristic of aging societies. However, there is still no effective treatment for AD and the underlying mechanisms of the disease remain largely unknown.

While aging remains one of the most significant risk factors for development of AD, increasing evidence strongly points to the potential roles of cerebrovascular and white matter abnormalities in AD development. A better understanding of the manner in which these abnormalities contribute to disease progression can be achieved by *in vivo* characterization of AD related pathologies. To this end, MR based techniques such as magnetic resonance angiography and relaxometry serve as effective non-invasive tools to longitudinally monitor changes in AD brain. The resolution and sensitivity of these MR based techniques used in clinical studies, however, are hampered by low magnetic fields (≤3T). To overcome this limitation, MRI systems having high field strength (≥7T) have been developed. Ultra high magnetic field MRI provides high sensitivity, increased resolution and better spectral dispersion of brain metabolites. These systems may cause a paradigm shift in AD research through the *in vivo* observation of subtle structural, metabolic and functional changes in the AD brain.

An advanced understanding of AD pathology can be achieved by validating *in vivo* changes with histology. To this end, transgenic mouse models of AD, which develop amyloid pathology, serve as valuable preclinical models to study the disease. *In vivo* imaging of these mouse models at ultra high magnetic field strengths can permit a better understanding of the underlying cellular mechanism of AD. This knowledge can be used to develop potential biomarkers and promising treatment strategies to impede and/or prevent AD progression.

In this thesis, a variety of MR based techniques were optimized and employed to longitudinally monitor the AD progression in transgenic mouse models of the disease at 9.4 T and 17.6 T. The relevance of this work is summarized in Chapter 1.

In Chapter 2, age-dependent blood flow alterations were examined in a Tg2576 mouse model of Alzheimer's disease using MR angiography at 17.6 T. AD is linked to abnormalities in the vascular system. Here ultra-high field MRA was employed to monitor age-dependent cerebrovascular alterations in the Tg2576 model. The blood flow alterations observed in the middle cerebral artery and anterior communicating artery increased in the Tg2576 mice compared to the wild-type mice over time. Histological data revealed that these alterations such as signal voids might be correlated with severity of Aβ type of CAA. These results show that ultra-high field MRA is a valuable tool to monitor blood flow alterations longitudinally in living mice.

In Chapter 3, *in vivo* T_2 changes were longitudinally monitored in the corpus callosum, the largest white matter structure in the brain, of the Tg2576 mice. Being sensitive marker for tissue pathology, *in vivo* T_2 changes depicted severe pathology in the corpus callosum as well as in the gray matter regions of Tg2576 mice. In particular, a marked increase in T_2 values was observed in the 10 months of age Tg2576 mice suggesting early microstructural changes in the white matter. These pathologies were correlated with gliosis, demyelination, and Aβ deposition.

In Chapter 4, age-dependent regional brain T_1 and T_2 changes in C57BL/6J mice were established at 17.6T. Being the main component of contrast in MRI, the estimates of *in vivo* T_1 and T_2 will be useful in future studies to optimize pulse sequences for optimal image contrast at 17.6T and will serve as baseline values against which disease related relaxation changes could be assessed in mice. Chapter 5 presents general discussion and future outlook of the thesis.

Samenvatting

Dementie ten gevolge van AD heeft grote gevolgen voor de personen die er aan lijden, zorgverleners, en het zorgstelsel. Ontwikkelde landen en ontwikkelingslanden zullen de uitdaging aan moeten gaan met veelvuldig voorkomende AD, wat karakteristiek is voor vergrijzende maatschappijen. Er is nog geen effectieve behandeling voor AD en de onderliggende werking van deze ziekte blijft voor het grootste deel onbekend.

Hoewel veroudering een van de belangrijkste risicofactoren is voor ontwikkeling van AD, is er steeds meer bewijsmateriaal dat wijst op de potentiële rol van cerebrovasculaire- en witte massa-afwijkingen in de ontwikkeling van AD. Een beter begrip van de manier waarop deze afwijkingen bijdragen aan de ziekeprogressie kan worden verkregen met *in vivo* kenschetsing van AD gerelateerde ziektes. Om dit te bewerkstellingen dienen MR gebaseerde technieken zoals magnetische resonantie angiografie en relaxometrie als effectieve non-invasieve instrumenten om de veranderingen in de AD hersenen longitudinaal te volgen. De resolutie en gevoeligheid van deze MR gebaseerde technieken die gebruikt worden in klinische studies worden daarentegen belemmerd door zwakker magnetische velden (≤3T). Om deze beperking te overwinnen zijn er MRI systemen met sterke magnetische velden (≥7T) ontwikkeld. MRI met zeer sterke magnetische velden biedt grote gevoeligheid, hogere resolutie en betere spectrale dispersie van hersenmetabolieten. Deze systemen zullen mogelijk een paradigmaverschuiving in AD onderzoek veroorzaken door *in vivo* waarneming van subtiele structurele, metabolische en functionele veranderingen in de AD hersenen.

Een vergaand begrip van AD afwijkingen kan bereikt worden door de *in vivo* veranderingen te vergelijken met histologie. Hiertoe dienen transgene muismodellen van AD, die een amyloidafwijking ontwikkelen, tot waardevolle preklinische modellen om de ziekte te bestuderen. Het *in vivo* afbeelden van deze muismodellen bij zeer hoge magnetische veldsterkte staat een beter begrip van de onderliggende cellulaire mechanismen van AD toe. Deze kennis kan gebruikt worden om potentiële biomarkers en veelbelovende behandelingsstrategieën te ontwikkelen om de AD ontwikkeling te belemmeren en/of te voorkomen.

In dit proefschrift zijn verschillende MR gebaseerde technieken geoptimaliseerd en gebruikt om de ontwikkeling van AD in een transgeen muismodel van de ziekte te onderzoeken bij 9.4T en 17.6T. De toepasselijkheid van dit werk is samengevat in Hoofdstuk 1.

In Hoofdstuk 2 zijn leeftijdsafhankelijke bloedstroomveranderingen onderzocht in het Tg2576 muismodel van Alzheimer met MR angiografie bij 17.6T. AD is gekoppeld aan afwijkingen in het vasculaire systeem. Hierbij werd zeer hoge magnetische veldsterkte MRA gebruikt om de leeftijdsafhankelijke cerebrovasculaire veranderingen in Tg2576 te volgen. De bloedstroomveranderingen opgemerkt in de middelste hersenslagader en de arteria communicans anterior nemen in de loop der tijd toe in de Tg2576 muizen ten opzichte van de wild-type muizen. Histologische gegevens hebben onthuld dat deze veranderingen zoals signaalleegtes wellicht gecorreleerd zijn met de hevigheid van het Aβ type van CAA. Deze resultaten tonen aan dat zeer hoge magnetische veldsterkte MRA een waardevol instrument zijn om de bloedstroomveranderingen longitudinaal te onderzoeken in levende muizen.

In Hoofdstuk 3 zijn *in vivo* T_2 veranderingen longitudinaal onderzocht in het corpus callosum, de grootste witte-massastsructuur in de hersenen, van de Tg2576 muizen. *In vivo* T_2 veranderingen zijn gevoelige indicatoren voor weefselpathologie en laten grote pathologische verstoringen in het corpus callosum en in de grijze-massagebieden van de Tg2576-muizen zien. In het bijzonder werd een opvallende verhoging in T_2 waarden gemeten in de 10 maanden oude Tg2576-muizen, wat vroege microstructurele veranderingen in de witte massa suggereert. Deze afwijkingen werden gecorreleeerd met gliosis, demyelinisatie, en Aβ-afzetting.

In Hoofdstuk 4 werden leeftijdsafhankelijke T_1 en T_2 veranderingen in de hersengebieden van C57BL/6J-muizen vastgelegd bij 17.6T voor de grootste contrastcomponent van de MRI. De schattingen van *in vivo* T_1 en T_2 zullen nuttig zijn in toekomstig onderzoek om de pulsreeksen te optimaliseren voor optimaal afbeeldingscontrast bij 17.6T, en zullen dienen als ijkingswaarden waartegen ziektegerelateerde relaxatieveranderingen kunnen worden geëvalueerd in muizen. Hoofdstuk 5 presenteert een algemene discussie en toekomstig vooruitzicht voor het werk in dit proefschrift.

Curriculum Vitae

In 1995, after finishing my high school education, I started my studies in the Department of Biological Sciences at the Middle East Technical University (METU). In 2004, I graduated from the master program of Biotechnology in METU. In 2007, I did my internship in the Medical Pharmacology Department in Leiden University: "The use of primary glucocorticoid target genes as markers for glucocorticoid responsiveness during the development" under the guidance of Dr. Onno Meijer and Dr. Danielle Champagne. Results were presented in the Dutch Endo-Neuro-Psycho Meeting (2008 & 2009). In September 2008, I started my PhD in the solid state NMR group of prof. dr. H.J.M de Groot, under the guidance of Dr. Alia. During my PhD I had presented my work in the ISMRM meetings (2009,2010 and 2011). Since November 2012, I have been working in the Bio-medical Imaging Group of prof. dr. Annemie van der Linden, as a postdoctoral fellow.

List of publications

Full publications

Longitudinal monitoring of transverse relaxation time (T_2) changes in the corpus callosum region of a mouse model of Alzheimer' disease
F. Kara, R. Schliebs, A. Van der Lindenden, H.J.M. Groot and A. Alia. (2013) *Submitted*.

In vivo measurement of transverse relaxation time in the mouse brain at 17.6 T
F. Kara, Fu Chen, J. Matysik, A. Alia. MRM doi: 10.1002/mrm.24533 (IF= 2.96)

Monitoring blood flow alterations in the Tg2576 mouse model of Alzheimer's disease by *in vivo* magnetic resonance angiography at 17.6 T.
F. Kara, E.S. van Dongen, R. Schliebs, M. A. van Buchem, H. J. de Groot, and A. Alia.. Neuroimage 2012; 60: 958–966. (IF= 5.89).

RNase Dre2 mutant zebrafish model familial cystic leukoencephalopathy and reveal a role for RNase T2 in degrading ribosomal RNA
N. Haud, **F. Kara**, S. Diekmann , M. Henneke, JR. Willer, MS. Hillwig, RG. Gregg, GC. MacIntosh, J. Gärtner, A. Alia, A.F.L. Hurlstone. Proc Natl Acad Sci USA. 2011; 108:3:1099-1103. (IF=9.68)

Prospects of Magnetic Resonance Spectroscopy in Mouse Models of Alzheimer's Disease
F. Kara, N. Braakman , M.A. van Buchem, H.J.M. de Groot, A. Alia. Curr Med Imag Rev. 2011; 7:1:80-87. (IF = 0.7)

In vivo evaluation of cerebrovascular blood flow artifacts in a transgenic mouse model of Alzheimer's disease using MRI
Kara, F., Ravensbergen, J., et al., J Neuro. 2009; 110 (Supp,1):38. (IF = 7.27)

Individual variation in the spatial reference and working memory assessed under allothetic and idiothetic orientation cues in rat
E.J. Doğru, U. Gümüşbaş, **F..Kara**. Acta Neurobiol Exp. 2003; 63:17-23. (IF= 2.11)

Conference proceedings

Age-related regional brain T_2 and T_1 relaxation times changes in the healthy mouse at 17.6 T
F. Kara, Fu Chen, I. Ronen, H.J.M. de Groot, J. Matysik, A. Alia Intl. Soc. Mag. Reson. Med. 2013 electronic poster 2881.

2D L-cosy MR spectroscopy detects changes in brain glucose level in mouse model of AD
A. Alia, **F. Kara**, N. Braakman, M.A. van Buchem and R. Schliebs Intl. Soc. Mag. Reson. Med. 2013 electronic poster 2882.

Probing age-dependent cerebrovascular alterations in the Tg2576 mouse model of Alzheimer's disease by magnetic resonance angiography at 17.6 T
F. Kara, E.S. van Dongen, et al., Intl. Soc. Mag. Reson. Med. 2012

Regional glutamate alterations in 11-month-old Tg2576 mouse model of Alzheimer's disease detected by *in vivo* ^{1}H magnetic resonance spectroscopy at 9.4 T
Alia, **F. Kara**., Intl. Soc. Mag. Reson. Med. 2012

Ultra High Field Magnetic Resonance Microimaging in Zebrafish Model of Cystic Leukoencephalopathy
Alia, H. Noémie, **F. Kara**, and A. Hurlstone. Intl. Soc. Mag. Reson. Med. 2011; 19:2230.

Changes in glucose level with age and its correlation with severity of plaque deposition in a transgenic model of Alzheimer's disease
F. Kara, K. Möbius, M. A. van Buchem, et al. . Intl. Soc. Mag. Reson. Med. 2011; 19:2231.

In vivo measurement of T_2 relaxation times in mouse brain at 17.6 Tesla
F. Kara, F. Chen, J. Matysik, and A. Alia.. Proc. Intl. Soc. Mag. Reson. Med. 2011; 19: electronic poster 3971.

Magnetic resonance angiography of the mouse cerebrovascular system at 17.6 T
F. Kara, and A. Alia. Proc. Intl. Soc. Mag. Reson. Med. 2010; 18: electronic poster 2247.

In vivo longitudinal monitoring of blood flow alterations in TG2576 mouse model of Alzheimer's disease
F. Kara, N. Braakman, et al. Proc. Intl. Soc. Mag. Reson. Med. 2010; 18:4273.

2D L-COSY MR spectroscopy detects very early changes in the brain of Alzheimer mouse
S. van Duijn, **F. Kara**, et al.. Proc. Intl. Soc. Mag. Reson. Med. 2010; 18:4257.

Alzheimer's plaques and its association with neurochemical changes with age monitored by *in vivo* magnetic resonance microimaging and spectroscopy
Kara F., Braakman N., et al. Development of FENS Forum of Neuroscience Abstr. 2010; 5: 167.9.

The use of primary glucocorticoid target genes as markers for glucocorticoid responsiveness during the development
E. Kitraki, **F. Kara**, et al. 2009 8th Dutch Endo-Neuro-Psycho Meeting Doorwerth/ The Netherlands.

MRI assessment of blood flow artifacts in a transgenic mouse model of Alzheimer's disease
F. **Kara,** J. Ravensbergen, et al., Proc. Intl. Soc. Mag. Reson. Med**.** 2009; 17:1331.

In vivo localized two-dimensional MR spectroscopy to compare the neurochemical profile in wild-type and transgenic mouse model of Alzheimer's disease

N. Braakman, **F. Kara,** et al., Proc. Int. Soc. Mag. Reson. Med. 2009; 17:108.